

Award Number: W81XWH-08-1-0191

TITLE: Interaction of Blast and Head Impact in the Generation of Brain Injuries

PRINCIPAL INVESTIGATOR: Zaouk, Abdullatif DSc

CONTRACTING ORGANIZATION: Foster-Miller Inc.
Waltham, Massachusetts 02451-1196

REPORT DATE: August 2009

TYPE OF REPORT: Final

PREPARED FOR: U.S. Army Medical Research and Materiel Command
Fort Detrick, Maryland 21702-5012

DISTRIBUTION STATEMENT:

Approved for public release; distribution unlimited

The views, opinions and/or findings contained in this report are those of the author(s) and should not be construed as an official Department of the Army position, policy or decision unless so designated by other documentation.

REPORT DOCUMENTATION PAGE

Form Approved
OMB No. 0704-0188

Public reporting burden for this collection of information is estimated to average 1 hour per response, including the time for reviewing instructions, searching existing data sources, gathering and maintaining the data needed, and completing and reviewing this collection of information. Send comments regarding this burden estimate or any other aspect of this collection of information, including suggestions for reducing this burden to Department of Defense, Washington Headquarters Services, Directorate for Information Operations and Reports (0704-0188), 1215 Jefferson Davis Highway, Suite 1204, Arlington, VA 22202-4302. Respondents should be aware that notwithstanding any other provision of law, no person shall be subject to any penalty for failing to comply with a collection of information if it does not display a currently valid OMB control number. **PLEASE DO NOT RETURN YOUR FORM TO THE ABOVE ADDRESS.**

1. REPORT DATE (DD-MM-YYYY) 01-09-2009		2. REPORT TYPE Final		3. DATES COVERED (From - To) 1 March 2008 - 31 Aug 2009	
4. TITLE AND SUBTITLE Interaction Of Blast And Head Impact In The Generation Of Brain Injuries				5a. CONTRACT NUMBER	
				5b. GRANT NUMBER W81XWH-08-1-0190	
				5c. PROGRAM ELEMENT NUMBER	
6. AUTHOR(S) Xudong Xin and Abdullatif Zaouk				5d. PROJECT NUMBER	
				5e. TASK NUMBER	
				5f. WORK UNIT NUMBER	
7. PERFORMING ORGANIZATION NAME(S) AND ADDRESS(ES) AND ADDRESS(ES) Foster-Miller, Inc. Waltham, MA 02451				8. PERFORMING ORGANIZATION REPORT NUMBER	
9. SPONSORING / MONITORING AGENCY NAME(S) AND ADDRESS(ES) U.S. Army Medical Research and Materiel Command 1077 Patchel Street Fort Detrick, Maryland 21702-5012				11. SPONSOR/MONITOR'S REPORT NUMBER(S)	
				12. DISTRIBUTION / AVAILABILITY STATEMENT Approved for public release; distribution unlimited	
13. SUPPLEMENTARY NOTES					
14. ABSTRACT TBI occurs as a direct result of blast wave-induced changes in atmospheric pressure (primary blast injury), from objects put in motion by the blast hitting people (secondary blast injury), and by people being forcefully put in motion by the blast (tertiary blast injury) (Taber, 2006). The brain is clearly vulnerable to both secondary and tertiary blast injury. The most common types of TBI are diffused axonal injury, contusion, and subdural hemorrhage. In this report, efforts have been made to quantitatively study the effects of blast overpressure and blast-related impact on secondary and tertiary TBI. A series of nonlinear dynamic finite-element analyses have been performed on a human-head (H-head) finite-element model developed by ESI Group and a finite-element Hybrid-III dummy model by LSTC. Finite-element calculations were performed to validate the ESI H-head model against the 3D brain motion data of Hardy et al. (2001) and the intracranial pressure data of Nahum et al. (1977). Additionally, available blast loading approaches were discussed, specifically the smoothed particle hydrodynamics (SPH) method. Parametric simulations involving primary, secondary, and tertiary blast injury were performed to evaluate the effect of standoff distance, impulse and fragment speed on the extent of damage to the brain, using cumulative strain damage measure as the injury metric.					
15. SUBJECT TERMS TBI, FEA, SPH, Blast Impact, Primary Blast Injury, Secondary Blast Injury, Tertiary Blast Injury, PAM-CRASH, LS-DYNA					
16. SECURITY CLASSIFICATION OF: U			17. LIMITATION OF ABSTRACT U	18. NUMBER OF PAGES 96	19a. NAME OF RESPONSIBLE PERSON USAMRMC
a. REPORT U	b. ABSTRACT U	c. THIS PAGE U			19b. TELEPHONE NUMBER (include area code)

TECHNICAL REPORT

INTERACTION OF BLAST AND HEAD IMPACT IN THE GENERATION OF BRAIN INJURIES

August, 2009

Submitted to

U.S. Army Medical Research and Material
Command
1077 Patchel Street
Fort Detrick, Maryland 21702-5012

Submitted by

Xudong Xin and
Abdullatif (Bud) Zaouk (PI)
QinetiQ North America | Foster-Miller Inc.
350 Second Avenue
Waltham, MA 02451-1196

Contents

CONTENTS.....	I
FIGURES	III
TABLES	VI
ACKNOWLEDGMENT	VII
1. INTRODUCTION.....	1
2. ESI H-HEAD FINITE-ELEMENT MODEL.....	3
3. VALIDATION OF ESI H-HEAD MODEL	9
3.1 H-HEAD MODEL VALIDATION AGAINST NEUTRAL DENSITY TARGETS (NDT) TEST.....	9
3.1.1 <i>Description of NDT Test by Hardy et al.</i>	9
3.1.2 <i>Simulation Procedure and Validation Results</i>	10
3.1.3 <i>Conclusion for H-Head FE Model Validation against NDT Test</i>	20
3.2 H-HEAD MODEL VALIDATION AGAINST HEAD IMPACT TEST.....	20
3.2.1 <i>Nahum Head Impact Test Description</i>	20
3.2.2 <i>FE Modeling Procedure and Results</i>	21
3.2.3 <i>Conclusion for H-Head FE Model Validation against Nahum's Test</i>	25
4. BRAIN INJURY METRICS.....	26
5. BLAST OVERPRESSURE SIMULATION METHODS	28
5.1 BLAST OVERPRESSURE SIMULATION METHODS	28
5.2 EVALUATION OF SPH METHOD IN PAM-SHOCK.....	28
5.3 COMPARISON OF SPH (PAM-SHOCK), ALE AND CONWEP (LS-DYNA)	34
5.4 BLAST SIMULATION CONCLUSION.....	38
6. PARAMETRIC SIMULATIONS OF PRIMARY BLAST INJURY	40
6.1 SIMULATION PROCEDURE OF PRIMARY BLAST-INDUCED TBI	40
6.2 SIMULATION RESULTS.....	41
6.2.1 <i>Front loading</i>	41
6.2.2 <i>Rear Loading</i>	45
6.2.3 <i>Primary Blast Injury Parametric Simulation Results</i>	48
6.3 REMARKS.....	52
7. PARAMETRIC SIMULATIONS OF SECONDARY BLAST INJURY	53
7.1 SIMULATION PROCEDURE OF SECONDARY BLAST-INDUCED TBI	53
7.2 SIMULATION RESULTS.....	54
7.2.1 <i>Front Impact</i>	54
7.2.2 <i>Rear Impact</i>	57
7.2.3 <i>Secondary Blast Injury Parametric Simulation Results</i>	60
7.3 REMARKS.....	64
8. PARAMETRIC SIMULATION OF TERTIARY BLAST INJURY.....	65
8.1 SIMULATION PROCEDURE OF TERTIARY BLAST-INDUCED TBI	65
8.2 SIMULATION RESULTS.....	66
8.2.1 <i>Front Blast Loading with Rear Impact Event</i>	66
8.2.2 <i>Rear Blast Loading with Front Impact Event</i>	70
8.2.3 <i>Tertiary Blast Injury Parametric Simulation Results</i>	74
8.3 REMARKS.....	78

9. KEY RESEARCH ACCOMPLISHMENTS AND CONCLUSIONS..... 79
10. REFERENCES81

Figures

FIGURE 1-1 SIMULATION PROCESS USED IN PROJECT	2
FIGURE 2-1 ESI H-HEAD FINITE-ELEMENT MODEL AND INNER STRUCTURE	3
FIGURE 2-2 ESI H-HEAD FE MODEL DETAILS	4
FIGURE 3-1 THE BIPLANAR X-RAY SYSTEM USED IN NDT TESTS (ALL BY HARDY ET AL. 2001)	9
FIGURE 3-2 SETUP OF ACCELERATION OR PADDED IMPACTOR TEST	9
FIGURE 3-3 SETUP OF DECELERATION OR FIXED BLOCK TEST	10
FIGURE 3-4 SKULL MARKERS AND GRAVITY CENTER LOCATION IN NDT TESTS	10
FIGURE 3-5 NODAL LOCATIONS IN H-HEAD MODEL CORRESPONDING TO NDT TESTS	11
FIGURE 3-6 VERIFICATION OF ACCELERATION DATA ON H-HEAD MODEL FOR TEST C755-T2	13
FIGURE 3-7 VERIFICATION OF ROTATIONAL VELOCITY DATA ON H-HEAD MODEL FOR TEST C755-T2.....	13
FIGURE 3-8 X-DISPLACEMENT TIME-HISTORY COMPARISON AT NDT-A1 FOR TEST C755-T2	13
FIGURE 3-9 X-DISPLACEMENT TIME-HISTORY COMPARISON AT NDT-A5 FOR TEST C755-T2	14
FIGURE 3-10 X-DISPLACEMENT TIME-HISTORY COMPARISON AT NDT-P1 FOR TEST C755-T2.....	14
FIGURE 3-11 X-DISPLACEMENT TIME HISTORY COMPARISON AT NDT-P5 FOR TEST C755-T2	14
FIGURE 3-12 Z-DISPLACEMENT TIME HISTORY COMPARISON AT NDT-A1 FOR TEST C755-T2	15
FIGURE 3-13 Z-DISPLACEMENT TIME-HISTORY COMPARISON AT NDT-A5 FOR TEST C755-T2.....	15
FIGURE 3-14 Z-DISPLACEMENT TIME-HISTORY COMPARISON AT NDT-P1 FOR TEST C755-T2	15
FIGURE 3-15 Z-DISPLACEMENT TIME-HISTORY COMPARISON AT NDT-P5 FOR TEST C755-T2	16
FIGURE 3-16 VERIFICATION OF TRANSLATIONAL ACCELERATION DATA FOR NDT TEST C383-T1	16
FIGURE 3-17 VERIFICATION OF ROTATIONAL ACCELERATION DATA FOR NDT TEST C383-T1	17
FIGURE 3-18 X-DISPLACEMENT TIME-HISTORY COMPARISON AT NDT-A1 FOR TEST C383-T1	17
FIGURE 3-19 X-DISPLACEMENT TIME-HISTORY COMPARISON AT NDT-A6 FOR TEST C383-T1	18
FIGURE 3-20 X-DISPLACEMENT TIME-HISTORY COMPARISON AT NDT-P1 FOR TEST C383-T1	18
FIGURE 3-21 X-DISPLACEMENT TIME-HISTORY COMPARISON AT NDT-P6 FOR TEST C383-T1	18
FIGURE 3-22 Z-DISPLACEMENT TIME-HISTORY COMPARISON AT NDT-A1 FOR TEST C383-T1	19
FIGURE 3-23 Z-DISPLACEMENT TIME-HISTORY COMPARISON AT NDT-A6 FOR TEST C383-T1	19
FIGURE 3-24 Z-DISPLACEMENT TIME-HISTORY COMPARISON AT NDT-P1 FOR TEST C383-T1	19
FIGURE 3-25 Z-DISPLACEMENT TIME-HISTORY COMPARISON AT NDT-P6 FOR TEST C383-T1	20
FIGURE 3-26 IMPACT LOADING AREA AND PRESSURE MEASURED LOCATIONS	22
FIGURE 3-27 VERIFICATION OF INPUT FORCE-TIME HISTORY WITH TEST DATA.....	22
FIGURE 3-28 HEAD ACCELERATION TIME HISTORY COMPARISON	23
FIGURE 3-29 INTRACRANIAL PRESSURE TIME HISTORY PLOTS IN ANTERIOR REGION	23
FIGURE 3-30 INTRACRANIAL PRESSURE TIME HISTORY PLOTS IN POSTERIOR REGION	24
FIGURE 3-31 INTRACRANIAL PRESSURE TIME HISTORY PLOTS IN OCCIPITAL REGION.....	24
FIGURE 3-32 INTRACRANIAL PRESSURE TIME HISTORY PLOTS IN PARIETAL REGION	24
FIGURE 5-1 COARSE MESH (2.5CM ³) AND FINE SPH MESH (1.25CM ³) FOR 1 M ³ SPACE.....	29
FIGURE 5-2 BLAST PRESSURE WAVE PROPAGATION SIMULATED BY COARSE (UPPER) AND FINE MESHES (LOWER)	30
FIGURE 5-3 CONTACT FORCE BETWEEN SPH PARTICLES AND TARGETS FOR COARSE AND FINE MESHES	30
FIGURE 5-4 REFLECTED PRESSURE TIME HISTORIES FOR 6.25 KG TNT AT 1 M STANDOFF	31
FIGURE 5-5 DIMENSION AND BOUNDARY CONDITIONS OF THE QUARTER MODEL	31
FIGURE 5-6 PRESSURE WAVE PROPAGATION BY SPH METHOD	32
FIGURE 5-7 DENSITY, PRESSURE AND VELOCITY FRINGE AT PEAK VALUES	32
FIGURE 5-8 DENSITY TIME HISTORIES OF SELECTED SPH PARTICLES IN FRONT OF MIDDLE PAD	33
FIGURE 5-9 PRESSURE TIME HISTORIES OF SELECTED SPH PARTICLES IN FRONT OF MIDDLE PAD.....	33
FIGURE 5-10 VELOCITY TIME HISTORIES OF SELECTED SPH PARTICLES IN FRONT OF MIDDLE PAD	33
FIGURE 5-11 CONTACT FORCE TIME HISTORIES BETWEEN PARTICLES AND MIDDLE PAD	34
FIGURE 5-12 MODEL AND BOUNDARY CONDITION FOR AIR-SPHERE INTERACTION SIMULATION UNDER BLAST PRESSURE.....	35
FIGURE 5-13 PRESSURE FRINGES AT 0.22 MS AFTER DETONATION	36
FIGURE 5-14 REFLECTED PRESSURE TIME HISTORY COMPARISON	36
FIGURE 5-15 RIGID BODY ACCELERATION TIME HISTORY OF SPHERE BY DIFFERENT METHODS	37
FIGURE 5-16 RIGID BODY ACCELERATION TIME HISTORY COMPARISON (SPH CURVE BY SAE 1000).....	37

FIGURE 5-17 RIGID-BODY VELOCITY TIME HISTORY COMPARISON 37

FIGURE 5-18 RIGID-BODY DISPLACEMENT TIME HISTORY COMPARISON 38

FIGURE 6-1 SEATED DUMMY MODEL UNDER BLAST LOADING 41

FIGURE 6-2 PROGRESSIVE DEFORMATION OF DUMMY UNDER BLAST LOAD FROM FRONT CHARGE 41

FIGURE 6-3 TRANSLATIONAL ACCELERATION TIME HISTORY OF HEAD 42

FIGURE 6-4 ROTATIONAL ACCELERATION TIME HISTORY OF HEAD 42

FIGURE 6-5 FRINGES OF INTRACRANIAL PRESSURE VARIATION WITH TIME FOR FRONT BLAST LOADING 43

FIGURE 6-6 TYPICAL INTRACRANIAL PRESSURE TIME HISTORY FOR FRONT BLAST LOADING 43

FIGURE 6-7 CSDM TIME HISTORY FOR FRONT BLAST LOADING 44

FIGURE 6-8 TRANSLATION VELOCITY TIME HISTORY OF HEAD 44

FIGURE 6-9 ROTATIONAL VELOCITY TIME HISTORY OF HEAD 44

FIGURE 6-10 PROGRESSIVE DUMMY DEFORMATION UNDER BLAST LOAD FROM REAR CHARGE 45

FIGURE 6-11 TRANSLATIONAL ACCELERATION TIME HISTORY OF HEAD 45

FIGURE 6-12 ROTATIONAL ACCELERATION TIME HISTORY OF HEAD 45

FIGURE 6-13 TRANSLATIONAL VELOCITY TIME HISTORY OF HEAD 46

FIGURE 6-14 ROTATIONAL VELOCITY TIME HISTORY OF HEAD 46

FIGURE 6-15 FRINGES OF INTRACRANIAL PRESSURE VARIATION WITH TIME FOR REAR BLAST LOADING 47

FIGURE 6-16 TYPICAL INTRACRANIAL PRESSURE TIME HISTORY FOR REAR BLAST LOADING 47

FIGURE 6-17 CSDM TIME HISTORY FOR REAR BLAST LOADING 47

FIGURE 6-18 CSDM VS. IMPULSE CURVE FOR FRONT AND REAR BLAST LOADING 48

FIGURE 6-19 X-ACCELERATION HISTORIES OF HEAD AND CHEST FOR A FRONT CHARGE CASE 49

FIGURE 6-20 X-ACCELERATION HISTORIES OF HEAD AND CHEST FOR A REAR CHARGE CASE 49

FIGURE 6-21 ANTERIOR INTRACRANIAL PRESSURE HISTORIES BY FRONT BLAST LOADING 50

FIGURE 6-22 POSTERIOR INTRACRANIAL PRESSURE HISTORIES BY FRONT BLAST LOADING 50

FIGURE 6-23 OCCIPITAL INTRACRANIAL PRESSURE HISTORIES BY FRONT BLAST LOADING 50

FIGURE 6-24 ANTERIOR INTRACRANIAL PRESSURE HISTORIES BY REAR BLAST LOADING 51

FIGURE 6-25 POSTERIOR INTRACRANIAL PRESSURE HISTORIES BY REAR BLAST LOADING 51

FIGURE 6-26 OCCIPITAL INTRACRANIAL PRESSURE HISTORIES BY REAR BLAST LOADING 51

FIGURE 7-1 FE MODELS FOR FRONT IMPACT (LEFT) AND REAR IMPACT (RIGHT) BY FRAGMENT 54

FIGURE 7-2 PROGRESSIVE DEFORMATION OF DUMMY BY A FRONT BLOW FROM A FRAGMENT AT 20 M/S 54

FIGURE 7-3 TRANSLATIONAL ACCELERATION TIME HISTORY OF HEAD 55

FIGURE 7-4 ROTATIONAL ACCELERATION TIME HISTORY OF HEAD 55

FIGURE 7-5 TRANSLATIONAL VELOCITY TIME HISTORY OF HEAD 55

FIGURE 7-6 ROTATIONAL VELOCITY TIME HISTORY OF HEAD 56

FIGURE 7-7 FRINGES OF INTRACRANIAL PRESSURE VARIATION WITH TIME FOR A FRONT IMPACT 56

FIGURE 7-8 TYPICAL INTRACRANIAL PRESSURE TIME HISTORY FOR A FRONT IMPACT EVENT 56

FIGURE 7-9 CSDM TIME HISTORY FOR A FRONT IMPACT EVENT 57

FIGURE 7-10 PROGRESSIVE DEFORMATION OF DUMMY BY A REAR BLOW FROM A FRAGMENT AT 20 M/S 57

FIGURE 7-11 TRANSLATIONAL ACCELERATION-TIME HISTORY OF HEAD 58

FIGURE 7-12 ROTATIONAL ACCELERATION-TIME HISTORY OF HEAD 58

FIGURE 7-13 TRANSLATIONAL VELOCITY-TIME HISTORY OF HEAD 58

FIGURE 7-14 ROTATIONAL VELOCITY-TIME HISTORY OF HEAD 59

FIGURE 7-15 FRINGES OF INTRACRANIAL PRESSURE VARIATION WITH TIME FOR A REAR IMPACT 59

FIGURE 7-16 TYPICAL INTRACRANIAL PRESSURE TIME HISTORY FOR A REAR IMPACT EVENT 59

FIGURE 7-17 CSDM TIME HISTORY FOR A TYPICAL REAR IMPACT EVENT 60

FIGURE 7-18 ANTERIOR INTRACRANIAL PRESSURE HISTORIES FOR FRONT IMPACT AT VARIOUS SPEEDS 61

FIGURE 7-19 POSTERIOR INTRACRANIAL PRESSURE HISTORIES FOR FRONT IMPACT AT VARIOUS SPEEDS 61

FIGURE 7-20 OCCIPITAL INTRACRANIAL PRESSURE HISTORIES FOR FRONT IMPACT AT VARIOUS SPEEDS 61

FIGURE 7-21 ANTERIOR INTRACRANIAL PRESSURE HISTORIES FOR REAR IMPACT AT VARIOUS SPEEDS 62

FIGURE 7-22 POSTERIOR INTRACRANIAL PRESSURE HISTORIES FOR REAR IMPACT AT VARIOUS SPEEDS 62

FIGURE 7-23 OCCIPITAL INTRACRANIAL PRESSURE HISTORIES FOR REAR IMPACT AT VARIOUS SPEEDS 62

FIGURE 7-24 CSDM VS IMPULSE CURVE FOR FRONT AND REAR FRAGMENT IMPACT 63

FIGURE 8-1 FE MODEL SET UP FOR TERTIARY-BLAST-INJURY SIMULATION 66

FIGURE 8-2 PROGRESSIVE DEFORMATION OF DUMMY BY A FRONT BLAST LOADING WITH REAR IMPACT 66

FIGURE 8-3 TRANSLATIONAL ACCELERATION TIME HISTORY OF HEAD 67

FIGURE 8-4 ROTATIONAL ACCELERATION TIME HISTORY OF HEAD 67

FIGURE 8-5 RIGID WALL IMPACT FORCE TIME HISTORY 67
 FIGURE 8-6 TRANSLATIONAL VELOCITY TIME HISTORY OF HEAD 68
 FIGURE 8-7 ROTATIONAL VELOCITY TIME HISTORY OF HEAD 68
 FIGURE 8-8 FRINGES OF INTRACRANIAL PRESSURE FOR A FRONT BLAST LOADING AND REAR IMPACT 69
 FIGURE 8-9 INTRACRANIAL PRESSURE TIME HISTORY FOR A FRONT BLAST WITH REAR IMPACT 69
 FIGURE 8-10 CSDM-TIME HISTORY FOR FRONT BLAST LOADING AND REAR IMPACT 70
 FIGURE 8-11 PROGRESSIVE DEFORMATION OF DUMMY BY A REAR BLAST LOADING WITH FRONT IMPACT 70
 FIGURE 8-12 TRANSLATIONAL ACCELERATION TIME HISTORY OF HEAD 71
 FIGURE 8-13 ROTATIONAL ACCELERATION TIME HISTORY OF HEAD 71
 FIGURE 8-14 HEAD-RIGID OBJECT IMPACT FORCE TIME HISTORY 71
 FIGURE 8-15 TRANSLATIONAL VELOCITY TIME HISTORY OF HEAD 72
 FIGURE 8-16 ROTATIONAL VELOCITY TIME HISTORY OF HEAD 72
 FIGURE 8-17 FRINGES OF INTRACRANIAL PRESSURE FOR A REAR BLAST LOADING WITH FRONT IMPACT 73
 FIGURE 8-18 INTRACRANIAL PRESSURE TIME HISTORY FOR A REAR BLAST WITH FRONT IMPACT 73
 FIGURE 8-19 CSDM TIME HISTORY FOR A REAR BLAST LOADING WITH FRONT IMPACT 74
 FIGURE 8-20 ANTERIOR INTRACRANIAL PRESSURE HISTORIES FOR FRONT BLAST LOADING AND REAR IMPACT
 75
 FIGURE 8-21 POSTERIOR INTRACRANIAL PRESSURE HISTORIES FOR FRONT BLAST LOADING AND REAR IMPACT
 75
 FIGURE 8-22 OCCIPITAL INTRACRANIAL PRESSURE HISTORIES FOR FRONT BLAST LOADING AND REAR IMPACT
 75
 FIGURE 8-23 ANTERIOR INTRACRANIAL PRESSURE HISTORIES FOR REAR BLAST LOADING AND FRONT IMPACT
 76
 FIGURE 8-24 POSTERIOR INTRACRANIAL PRESSURE HISTORIES FOR REAR BLAST LOADING AND FRONT IMPACT
 76
 FIGURE 8-25 OCCIPITAL INTRACRANIAL PRESSURE HISTORIES FOR REAR BLAST LOADING AND FRONT IMPACT
 76
 FIGURE 8-26 CSDM VS BLAST IMPULSE FOR TERTIARY-BLAST BRAIN INJURY 77
 FIGURE 8-27 IMPACT CONTRIBUTIONS TO CSDM FOR TERTIARY-BLAST BRAIN INJURY 77

Tables

TABLE 2-1 H-HEAD MODEL PART, ELEMENT AND MATERIAL TYPES	5
TABLE 3-1 NDT TEST DATA FOR C755-T2 AND C383-T1 (FROM HARD <i>ET AL</i> , 2001).....	12
TABLE 5-1 COMPARISON OF RESULTS FROM DIFFERENT METHODS FOR 6.25KG TNT	34
TABLE 5-2 COMPARISON OF BLAST PRESSURE SIMULATION RESULTS BY DIFFERENT METHODS	38
TABLE 6-1 CALCULATED CASES FOR PRIMARY BLAST INJURY SIMULATION	52
TABLE 7-1 CALCULATED CASES FOR SECONDARY BLAST INJURY SIMULATION	63
TABLE 8-1 CALCULATED CASES FOR TERTIARY BLAST INJURY SIMULATION.....	78

Acknowledgment

This report discusses the interaction of blast and head impact in the generation of brain injuries. QinetiQ North America | Foster-Miller performed this work under contract W81XWH-08-1-0191 from the Fiscal Year 2007 Department of Defense Post-Traumatic Stress Disorder/Traumatic Brain Injury Research Program of the Office of the Congressionally Directed Medical Research Programs (CDMRP).

The authors would like to thank ESI North America for their support and cooperation on this program, specifically Mr. Ramesh Dwarampudi, Mr. Daniel Dooge, and Mr. David Piesko. We also gratefully acknowledge Mr. David Moran who assisted in the technical editing of this report.

1. Introduction

Brain injury is an ever present risk of military duty. The experience of brain injury in the military and the need to develop new medical, safety and rehabilitative technologies to address the efficiency of evolving warfare have been instrumental in driving research and advancing clinical care (Salazar, 2000). Given improvements in helmet design and body armor and the resultant reductions in penetrating injuries including penetrating head trauma, blast-related closed-head injuries have become the signature injury of these military operations. Of total combat losses in Iraq, 48% have resulted from injuries caused by improvised explosive devices (IEDs). Among those most seriously injured, brain injury has been found in approximately 60% of evacuated casualties. Also, owing to increased use of body armor, combat injuries to the head and neck occur at a rate approximately four times greater than torso injuries, with the eyes and orbit among the most frequently injured anatomical structures.

In addition, brain injury has become a leading public health problem for civilians. In the United States, 1.4 million individuals sustain traumatic brain injury (TBI) annually, resulting in 235,000 hospital admissions and 50,000 deaths (Langlois, 2004). Economically, the total impact of direct and indirect medical and other costs in 1995 dollars was reported to exceed \$56 billion (Thurman, 2001).

TBI occurs as a direct result of blast-wave-induced changes in atmospheric pressure (primary blast injury), from objects put in motion by the blast hitting people (secondary blast injury), and by people being forcefully put in motion by the blast (tertiary blast injury) (Taber, 2006). The brain is clearly vulnerable to both secondary and tertiary blast injury. The most common types of TBI are diffused axonal injury, contusion, and subdural hemorrhage. It is thought that diffuse axonal injury results when shearing, stretching and/or angular forces pull on brain tissues, and that contusions occur when the brain moves within the skull enough to contact bone, causing hemorrhage and edema. Traumatic subdural hemorrhage may occur if the brain moves within the skull enough to tear the tributary surface veins that bridge from the brain surface to the dural venous sinus.

In this report, efforts have been made to quantitatively study the effects of blast overpressure and blast-related impact on secondary and tertiary TBI. A series of nonlinear dynamic finite-element analyses have been performed on a human-head (H-head) finite-element model developed by ESI Group and a finite-element Hybrid-III (H-III) dummy model by LSTC.

Finite-element (FE) calculations were performed to validate the ESI H-head model against the 3D brain motion data of Hardy et al. (2001) and the intracranial pressure data of Nahum et al. (1977), these experimental data being most applicable to the impact events. Additionally, available blast loading approaches were discussed, specifically the smoothed particle hydrodynamics (SPH) method. The SPH method is a meshless or gridless Lagrangian technique developed to simulate astrophysical problems. This method does not require any fixed connectivity and particles interact with one another by an interpolation function. In PAM-SHOCK or LS-DYNA, SPH method and JWL explosive materials are combined along with air material properties to explicitly model the blast wave propagation. The most advantageous feature of SPH is its ability to handle problems with extremely large deformations, such as detonation of high explosives. However, SPH technology is relatively new

compared with standard grid-based Lagrangian and Eulerian techniques. Several problems need to be solved before it is a fully developed computational continuum dynamics technique.

Primary blast-induced TBI simulations were conducted as baseline. This involved the dynamic behavior of the human head FE model under blast loading conditions with the purpose to quantify the extent of damage caused by the rigid motion of the head due to blast overpressure. Data obtained from the simulations can be used to superpose the brain injury with fragment impact in secondary blast injury, as well as to isolate the injury caused by impact in the tertiary blast injury. For the secondary simulations, TBI caused by impact from flying fragments with different momentums were performed, a series of calculations were performed with fragment impact on the frontal or occipital region of the H-head model. Tertiary blast injury simulations were conducted with the H-III model, which was put into motion and impacted with rigid objects under various impulsive pressures.

The following process was used in all simulations performed:

1. Perform simulations of fragment impact or blast loading on an LS-DYNA H-III FE model
2. Apply kinetic data (velocity and acceleration) of head CG (center of gravity) to the ESI H-head model
3. Perform H-head simulations
4. Systematically investigate brain injury patterns and damage levels

Furthermore, the cumulative strain damage measure (CSDM) for diffused axonal injuries was adopted to reflect injury level. Results are summarized to show the relation between injury severity and blast or/and impact impulse.

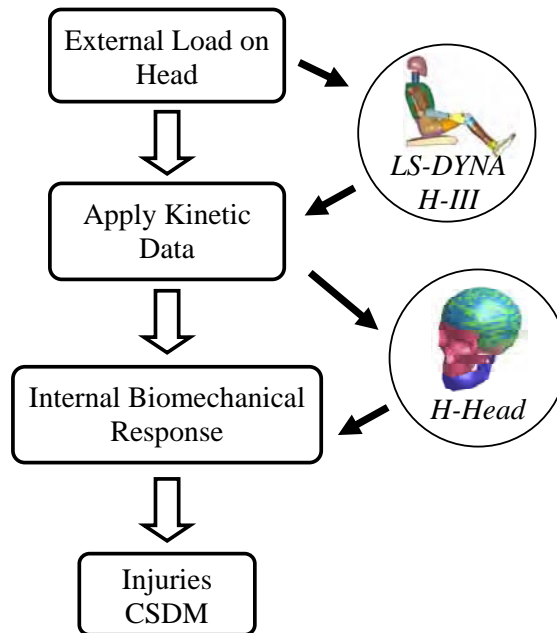


Figure 1-1 Simulation process used in project

2. ESI H-Head Finite-Element Model

The development of anatomically realistic computational models that represent adequate structural and material features, internal constraints, and proper boundary conditions has been evolving at a rapid pace. This includes the ability to model detailed aspects such as the dura, falx, sphenoid wings and the foramen, all of which affect the pressure distribution in the brain under impact and limit the motion of the brain tissue. Another significant component is the subarachnoidal layer that contains mainly cerebrospinal fluid (CSF). It plays a pivotal role in load transmission and mitigation, and shear relief from interactions between the surface of the brain and the dural membrane.

All of the components of the head-brain complex are composed of various levels of fluid and solid materials including soft and hard tissue. While the properties have been well described for a variety of purposes, descriptions aimed specifically at large deformations and strain rate dependency are not easily found. To further complicate matters, it is becoming increasingly difficult to find these properties in vivo.

With the rapid advances in computer technology, sophisticated computer models of the head can provide useful information in the investigation of neurotrauma due to impact. The internal biomechanical responses of the brain cannot be completely measured by experimental techniques without introducing large complexity, therefore FE models may be used to study impact events. Moreover, they reduce the need to conduct a large number of experimental tests. In particular, an FE model that describes in detail the complex geometry and the multiple material compositions of the brain can be used to calculate internal stress, strain and pressure at all locations and at any given instant during an impact (Zhang et al., 2001). These models, if validated rigorously, can be used to design countermeasures to mitigate brain injuries in the future.

A finite-element model of the human head developed by the ESI Group was used in this effort (Trameçon, 2003). The most recently released version of the ESI H-head model (v2007) consists of 63 parts, 32,800 nodes, 48,870 elements and 16 material types (Figure 2-1).

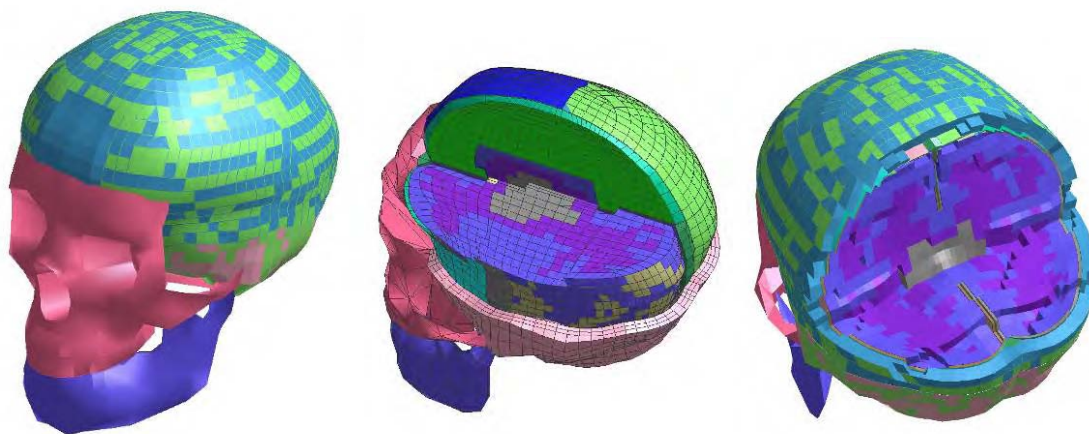


Figure 2-1 ESI H-head finite-element model and inner structure

The model includes the skull (inner and outer table, upper and lower dipole, face bone, mandible), dura, sinus, venous blood, pia, cerebral spinal fluid (CSF), white matter, gray matter, falx cerebri, tentorium, ventricle, cerebellum and brain stem. Contact interfaces are defined between related parts, such as dura↔csf, falx↔csf, tentorium↔csf, pia↔csf, pia↔falx, gray matter↔cerebellum, dura↔pia etc. Various material properties, including elastic, elastic-plastic, linear viscoelastic, null material, layered membrane with linear fibers, and Murnaghan EOS have been adopted and continuously updated in the H-head model for realistic biomechanical responses (Table 2-1).

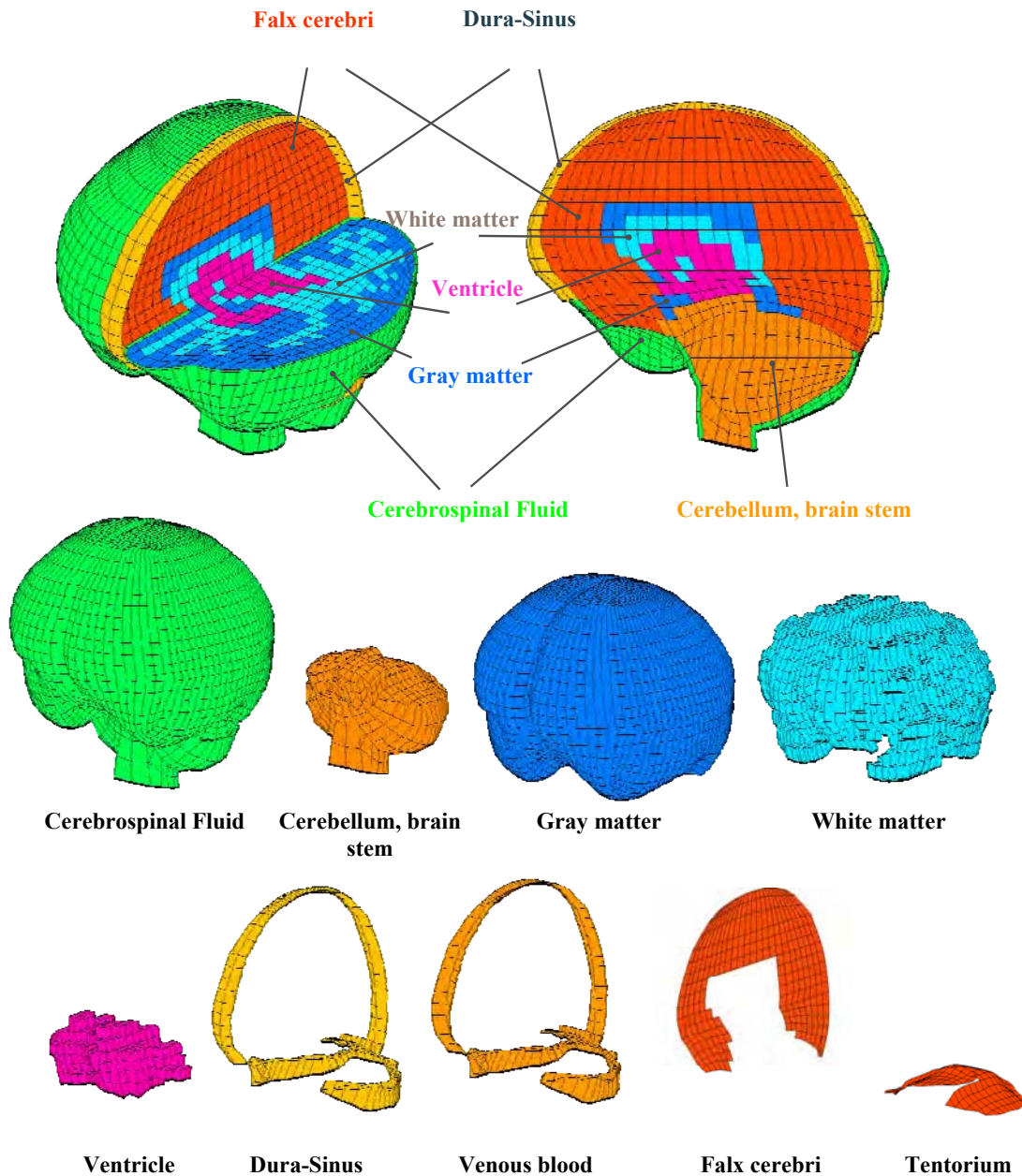


Figure 2-2 ESI H-head FE model details

Table 2-1 H-head model part, element and material types

Part, Airbag and Link Name	Element Type	Material Type
Outer table	shell	Elastic_Shell
Dipole upper	solid	Elastic_Plastic_Solid
Dipole lower	solid	Elastic_Plastic_Solid
Inner table	shell	Elastic_Shell
Facial bone	shell	Null_Material_Shell
Mandible	shell	Null_Material_Shell
Dura matter	membrane	Layered_Membrane
Dura sinus	membrane	Layered_Membrane
Venous blood	solid	Murnaghan Eos_Solid
CSF→left	solid	Murnaghan Eos Solid
CSF→right	solid	Murnaghan Eos Solid
Falx cerebri	membrane	Layered_Membrane
Pia	membrane	Layered_Membrane
Tentorium	membrane	Layered_Membrane
Gray matter	solid	Linear Visco_Elastic
White matter	solid	Linear Visco_Elastic
Ventricle	solid	Murnaghan_Eos Solid
Cerebellum & brain stem	solid	Linear Visco_Elastic
Airbag skin→Dura→RUAO	shell	Null_Material_Shell
Airbag skin→CSF→RUAO	shell	Null_Material_Shell
Airbag skin→dura→LUAO	shell	Null_Material_Shell
Airbag skin→CSF→LUAO	shell	Null_Material_Shell
Airbag skin→dura→RUPO	shell	Null_Material_Shell
Airbag skin→CSF→RUPO	shell	Null_Material_Shell
Airbag skin→dura→LUPO	shell	Null_Material_Shell
Airbag skin→CSF→LUPO	shell	Null_Material_Shell
Airbag skin→dura→RLPO	shell	Null_Material_Shell
Airbag skin→CSF→RLPO	shell	Null_Material_Shell
Airbag skin→dura→LLPO	shell	Null_Material_Shell
Airbag skin→CSF→LLPO	shell	Null_Material_Shell
Airbag skin→CSF→RUAI	shell	Null_Material_Shell
Airbag skin→pia→RUAI	shell	Null_Material_Shell
Airbag skin→CSF→LUAI	shell	Null_Material_Shell

Airbag skin→pia→LUAI	shell	Null_Material_Shell
Airbag skin→CSF→RUPI	shell	Null_Material_Shell
Airbag skin→Pia→RUPI	shell	Null_Material_Shell
Airbag skin→CSF→LUPI	shell	Null_Material_Shell
Airbag skin→pia→LUPI	shell	Null_Material_Shell
Airbag skin→CSF→RLPI	shell	Null_Material_Shell
Airbag skin→pia→RLPI	shell	Null_Material_Shell
Airbag skin→CSF→LLPI	shell	Null_Material_Shell
Airbag skin→pia→LLPI	shell	Null_Material_Shell
CSF→skin→left→outer	shell	Null_Material_Shell
CSF→skin→right→outer	shell	Null_Material_Shell
CSF→skin→left→inner	shell	Null_Material_Shell
CSF→skin→right→inner	shell	Null_Material_Shell
Airbag skin→pia→RIU	shell	Null_Material_Shell
Airbag skin→CSF→RIU	shell	Null_Material_Shell
Airbag skin→pia→LIU	shell	Null_Material_Shell
Airbag skin→CSF→LIU	shell	Null_Material_Shell
Airbag skin→CSF →RIL	shell	Null_Material_Shell
Airbag skin→tentorium→RIL	shell	Null_Material_Shell
Airbag skin→CSF →LIL	shell	Null_Material_Shell
Airbag skin→tentorium→LIL	shell	Null_Material_Shell
CSF→skin→left→upper	shell	Null_Material_Shell
CSF→skin→right→upper	shell	Null_Material_Shell
CSF→skin→left→lower	shell	Null_Material_Shell
CSF→skin→right→lower	shell	Null_Material_Shell
CSF→skin→left→media→outer	shell	Null_Material_Shell
CSF→skin→left→media→inner	shell	Null_Material_Shell
CSF→skin→left→falx	shell	Null_Material_Shell
CSF→skin→right→media→outer	shell	Null_Material_Shell
CSF→skin→right→media→inner	shell	Null_Material_Shell
tied→airbag skin tied to CSF	tied	Slink_Elink_Tied
tied→frontal bones tied to skull	tied	Slink_Elink_Tied

The following references were considered relevant for basic and detailed understanding, construction and validation of the head model:

Abel, Gennarelli and Segawa (1978) on incidence and severity of cerebral concussion in

rhesus monkeys from sagittal acceleration;
Bandak and Eppinger (1994), Bandak (1996) on brain FE models and impact traumatic brain injury;
Chapon, Verriest, Dedoyan, Trauchessec and Artru (1983) on brain vulnerability from real accidents;
Choi and Lee (1999b) on deformable FE models of the human body;
Claessens (1997), Claessens, Sauren and Wismans (1997) on FE modeling of the human head under impact conditions;
Cooper (1982a), Cooper (1982b) on injury of the skull, brain and cerebrospinal fluid;
Dimasi, Marcus and Eppinger (1991) on a 3D anatomical brain model for automobile crash loading;
Donnelly and Medige (1997) on shear properties of human brain tissues;
Ewing, Thomas, Lustick, Muzzy III, Willems and Majewski (1978) on the effect of the initial position on the head/neck response in sled tests;
Gennarelli (1980), Gennarelli, Thibault, Adams, Graham, Thompson and Marcincin (1982) on the analysis of head injury severity by AIS-80 (1980) and on diffuse axonal injury and traumatic coma in primates (1982);
Gray's Anatomy (1989): Atlas of Anatomy;
Gurdjian and Lissner (1944), Gurdjian, Webster and Lissner (1955), Gurdjian, Roberts and Thomas (1966) on mechanisms of head injury and brain concussion and tolerance of acceleration and intracranial pressure;
Holbourn [1943) on the mechanics of head injury;
Kang, Willinger, Diaw and Chinn (1997) on the validation of a 3D FE model of the human head in motorcycle accidents;
Lee, Melvin and Ueno (1987), Lee and Haut (1989) on FE analysis of subdural hematoma and bridging vein failure characteristics;
Lissner, Lebow and Evans (1960) on experiments on intracranial pressure;
Margulies, Thibault and Gennarelli (1990) on modeling brain injury in primates;
Miller and Chinzei (1997) on constitutive modeling of brain tissue;
Nahum, Smith and ward (1977) on intracranial-pressure dynamics during head impact;
Newman (1993) on head protection;
Ommaya, Hirsch, Flamm and Mahone (1966), Ommaya and Hirsch (1971), Ommaya and Gennarelli (1974) on cerebral concussions in the monkey (1966), on their tolerances (1971) and on their clinical/experimental correlation (1974);
Ono, Kikuchi, Nakamura, Kobayashi and Nakamura (1980), Ono (1999) on head injury tolerance for sagittal impact from tests (1980) and on spine deformation and on vertebral motion from whiplash test volunteers (1999);
Penn and Clasen (1982) on traumatic brain swelling and edema;
Putz and Pabst (2000): *Sobotta Atlas of Human Anatomy*;
Ruan, Khalil and King (1991) on human FE head model response in side impacts;
Ruan and Prasad (1994) on head injury assessment in frontal impacts by mathematical modeling;
Sances et al. (1982) on head and spine injuries;
Scott (1981) on the epidemiology of motorcyclist head and neck trauma;
Spitzer and Whitlock (1998): *Atlas of the Visible Human Male*;
Tariere (1981) on investigation of the brain with CT scanners;

Torg (1982), Torg and Pavlov (1991) on athletic injury on the head, neck and face;
Turquier, Kang, Trosseille, Willinger, Lavaste, Tarriere and Dömönt (1996) on the validation of a 3D FE head model against experiments;
Ueno, Melvin, Lundquist and Lee (1989) on 2D FE analysis of human brain under impact;
Voo, Kumaresan, Pintar, Yoganandan and Sances (1996) on a finite-element model of the human head;
Walke, Kollros and Case (1944) on the physiological basis of concussion;
Willinger, Kang and Diaw (1999) on the validation of a 3D FE human model against experimental impacts;
Wismans et al. (1994) on injury biomechanics;
Zeidler, Stürtz, Burg and Rau (1981) on injury mechanisms in head-on collisions;
Zhou, Khalil and King (1996) on the viscoelastic brain FE modeling for sagittal and lateral-rotation acceleration.

3. Validation of ESI H-Head Model

3.1 H-Head Model Validation against Neutral Density Targets (NDT) Test

3.1.1 Description of NDT Test by Hardy et al.

By using high-speed biplanar x-ray system and neutral density targets (NDTs), Hardy et al. (2001) investigated the relative brain motion with respect to the skull. The test data can be used for validation of finite-element models of human head. In their tests, an array of multiple NDTs were implanted in human brains in the temporoparietal and occipitoparietal regions to image brain displacement during impact events. A suspension fixture was used for testing of inverted, perfused human cadaver heads (Figure 3-1). After removing the rigid body motion from the test data, the brain motion data relative to the CG of the head were provided.



Figure 3-1 The biplanar x-ray system used in NDT tests (all by Hardy et al. 2001)

For the acceleration test, the skull was impacted by a padded linear-piston impactor (Figure 3-2); while in the deceleration test, the moving skull was stopped by an unpadded fixed surface (Figure 3-3). The head was supported during the acceleration phase in order to eliminate the neck flexion/extension prior to impact. The NDTs were implanted into two columns as shown in Figure 3-4, in which p is posterior column and a is anterior column.



Figure 3-2 Setup of acceleration or padded impactor test

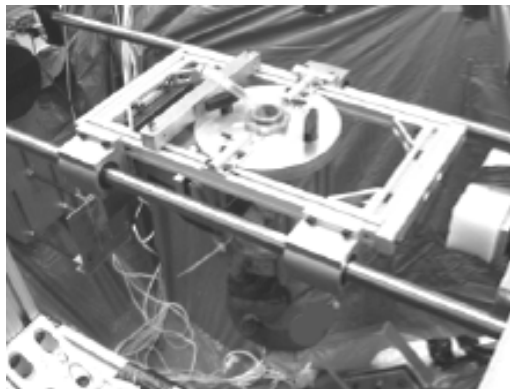


Figure 3-3 Setup of deceleration or fixed block test

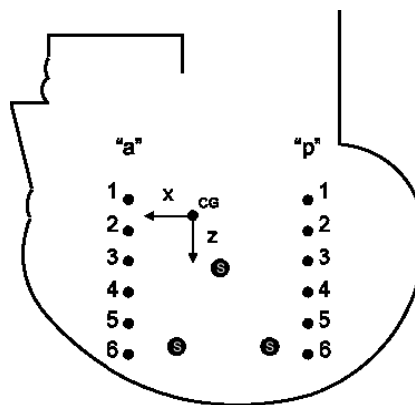


Figure 3-4 Skull markers and gravity center location in NDT tests

Two tests were chosen for ESI H-Head model validation in this project, C755-T2 and C383-T1. In test C755-T2, the head was accelerated by a blow to the occipital region. The impactor was a 150mm-diameter flat disk padded with 50mm-thick Ensolite. In test C383-T1, the head was decelerated by a blow to the anterior region. The fixed block was a 25mm-wide and 250mm-long acrylic structure. Some test information can be found in Table 3-1.

Hardy et al. had published the data as resultant acceleration, angular acceleration, velocity and displacement time-history plots in x, y and z directions. These data were filtered per SAE channel class 180-Hz specifications and were provided with respect to a local reference frame which is fixed within the moving skull. Their observation from low-severity tests showed that the relative displacement between brain and skull were on the order of $\pm 5\text{mm}$. Due to technical limitations, their study could not measure shear strain or principal strain of brain matter. The key findings were that the displacements of brain seem to lag the motion of the skull and the brain seems to return to its original configuration. This reflects the viscoelastic response of the brain material.

3.1.2 Simulation Procedure and Validation Results

Acceleration and velocity time histories in translational and rotational directions obtained from Hardy et al.'s NDT tests were used as input condition in the H-Head FE model.

Boundary conditions were considered free at the neck area since the impact phenomenon is too fast to be influenced by neck constraints. Furthermore, the coordinate system used in all NDT tests was used in the H-Head FE model, that is:

- x — from occipital to anterior, $\pm x$ is impacting direction
- y — from left to right, y is the major rotation axis when head is impacted
- z — from bottom to top

To validate H-Head model against Hardy’s tests, the following simulation process was used:

- Identify the CG of H-Head model.
- Define the outer and inner table, dipole, facial bone, and mandible parts in H-Head model as a rigid body — skull.
- Set up a local reference frame attached to the skull with the head CG as the origin. This reference frame is used for measuring relative motion of brain matter with respect to skull.
- Apply linear and rotational acceleration or velocity to the head CG.
- Select nodes corresponding to targets in NDT test for history output (Figure 3-5).
- Run PAM-CRASH calculations and output results
 - Output and verify the input acceleration or velocity curves.
 - Output nodal displacements of brain at NDTs’ location and remove rigid motions.
 - Compare calculated result with NDT test data.

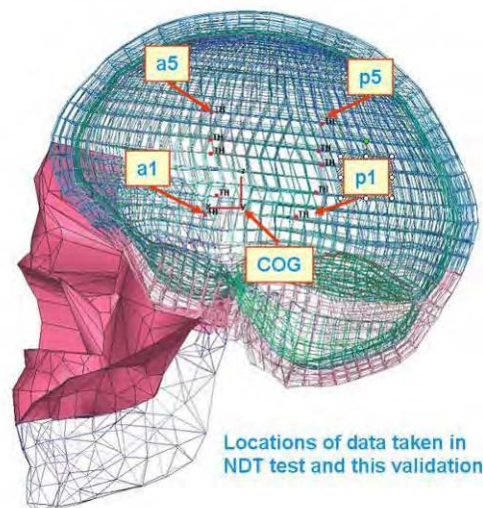


Figure 3-5 Nodal locations in H-Head model corresponding to NDT tests

Furthermore, H-Head FE model was based on an average human head with the following dimensions: 18.5cm (occiput to glabella) \times 21.5cm (vertex to mentum) \times 15.6cm (breadth).

Thus the FE model dimensions are different than the human cadaver head dimensions used in both tests (Table 3-1).

Table 3-1 NDT Test Data for C755-T2 and C383-T1 (from Hard *et al*, 2001)

Test	C755-T2	C383-T1
Cadaver #	755	383
Occiput to Glabella (cm)	19	20
Vertex to Mentum (cm)	25	26
Breadth (cm)	16	14
Circumference (cm)	55	56
Impact Type	Acceleration	Deceleration
Impact Surface	Flat piston	Angled block
Impact Area	Occipital	Anterior
Relative Severity	Lower	Higher
Camera System	JCL	VR4
Linear Acc_X Range (g)	-8 ~ +21	-46 ~ +5
Linear Acc_Y Range (g)	-7 ~ +3	-2 ~ +6
Linear Acc_Z Range (g)	-14 ~ +10	-41 ~ +20
Resultant ACC (g)	22	62
HIC 15ms	17	47
Rotational Acc_X Range (rad/s ²)	-342 ~ +121	-407 ~ +395
Rotational Acc_Y Range (rad/s ²)	-574 ~ +1882	-1930 ~ +2592
Rotational Acc_Z Range (rad/s ²)	-204 ~ +60	-523 ~ +875
Rotational Vel_X Range (rad/s)	-3 ~ 0	-3 ~ +1
Rotational Vel_Y Range (rad/s)	-1 ~ +18	-20 ~ +4
Rotational Vel_Z Range (rad/s)	-1 ~ 0	-1 ~ +3
Data used in finite-element simulation input	Linear acceleration and rotational velocity	Linear acceleration and rotational acceleration

C755-T2 is an acceleration test in which an occipital impact was applied. In the model validation, the linear acceleration and rotational velocity time histories from Hardy’s NDT test were used as simulation input parameters. Figure 3-6 and Figure 3-7 show the input data verification of the skull acceleration and rotational velocity with NDT test. By removing the skull’s rigid body motion, the relative displacements of the brain at selected NDT locations (a1, a5, p1 and p5) are given in Figure 3-8 - Figure 3-15 for comparison. The H-Head test C755-T2 showed that the relative displacement between brain and skull were on the order of ±5mm.

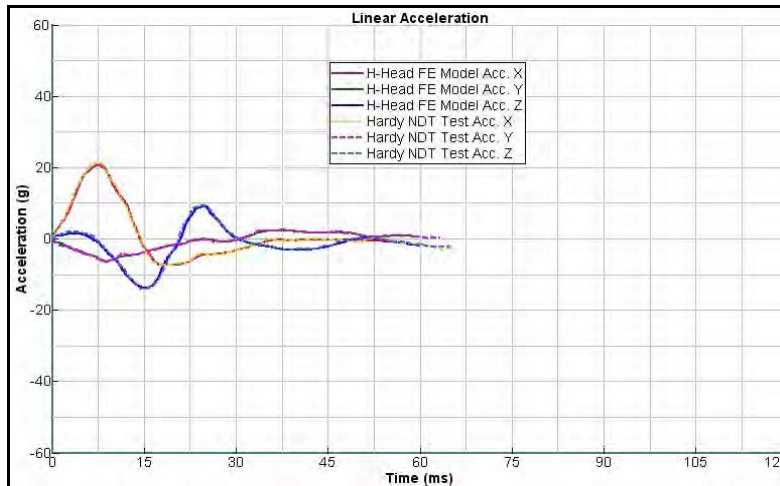


Figure 3-6 Verification of acceleration data on H-Head model for test C755-T2

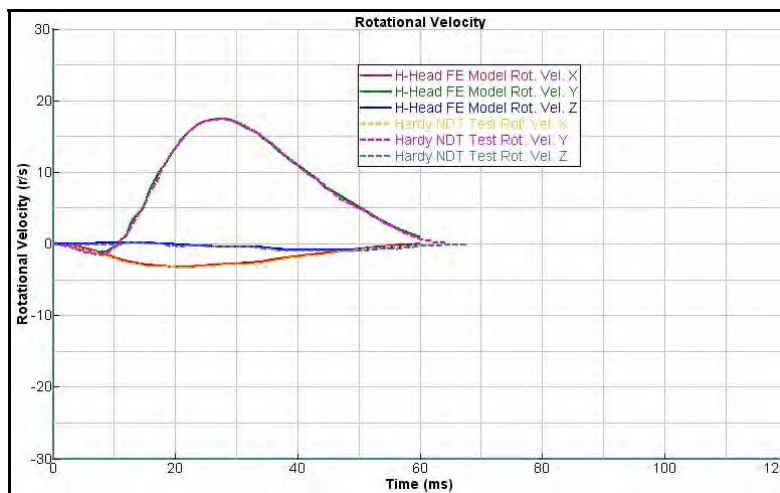


Figure 3-7 Verification of rotational velocity data on H-Head model for test C755-T2

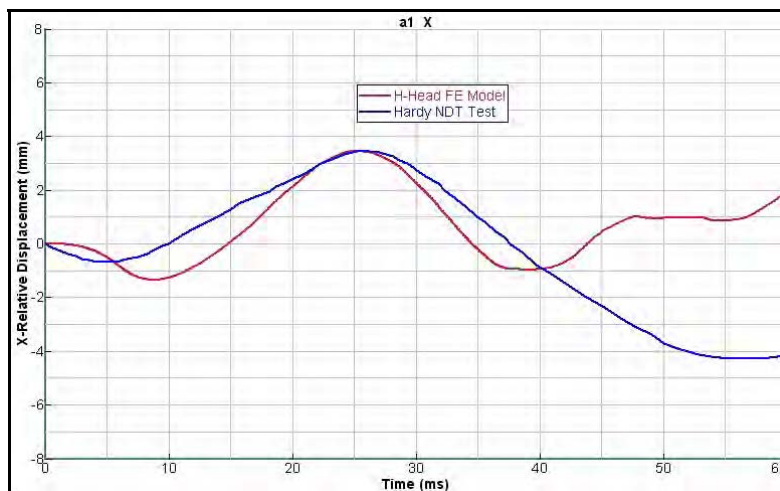


Figure 3-8 X-displacement time-history comparison at NDT-a1 for test C755-T2

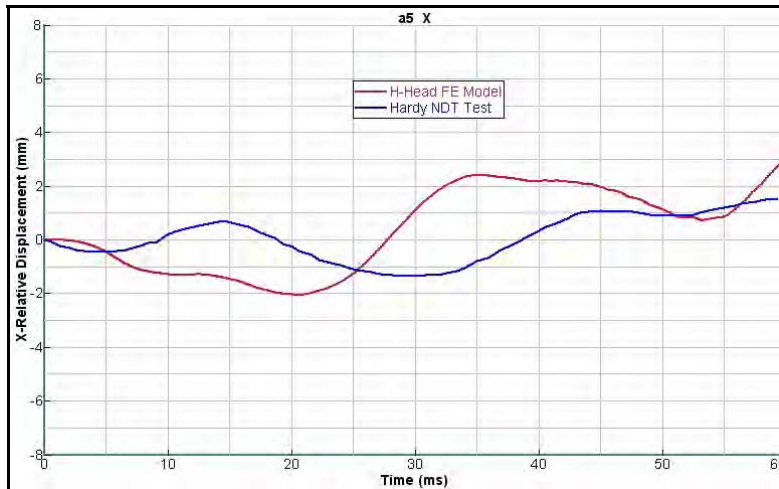


Figure 3-9 X-displacement time-history comparison at NDT-a5 for test C755-T2

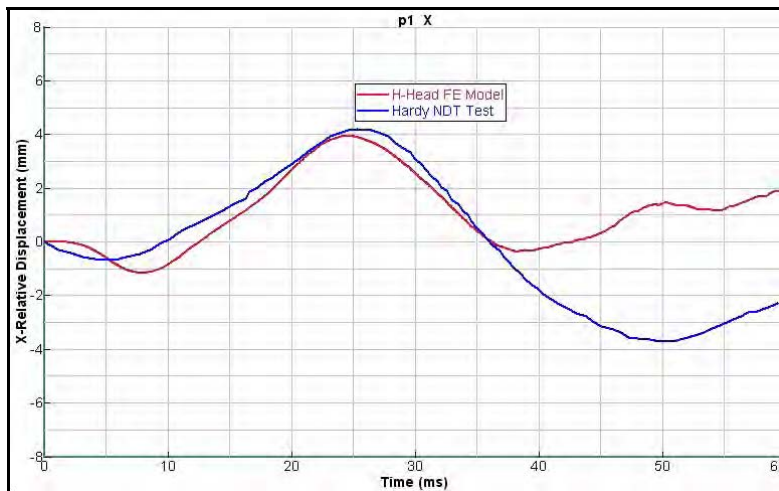


Figure 3-10 X-displacement time-history comparison at NDT-p1 for test C755-T2

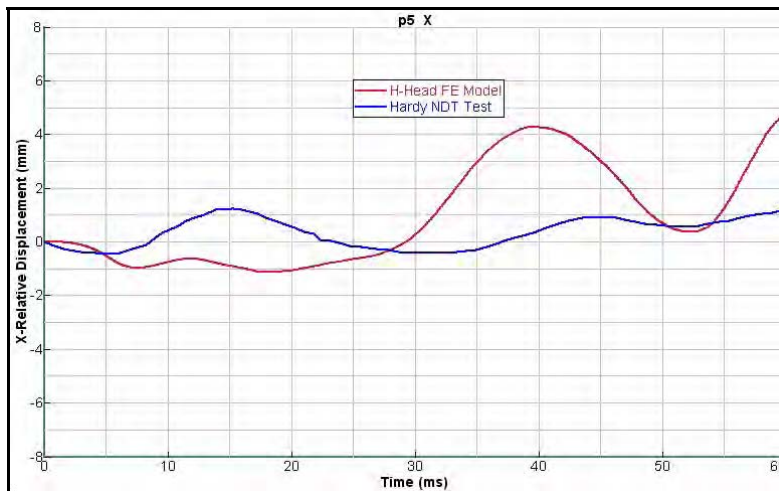


Figure 3-11 X-displacement time history comparison at NDT-p5 for test C755-T2

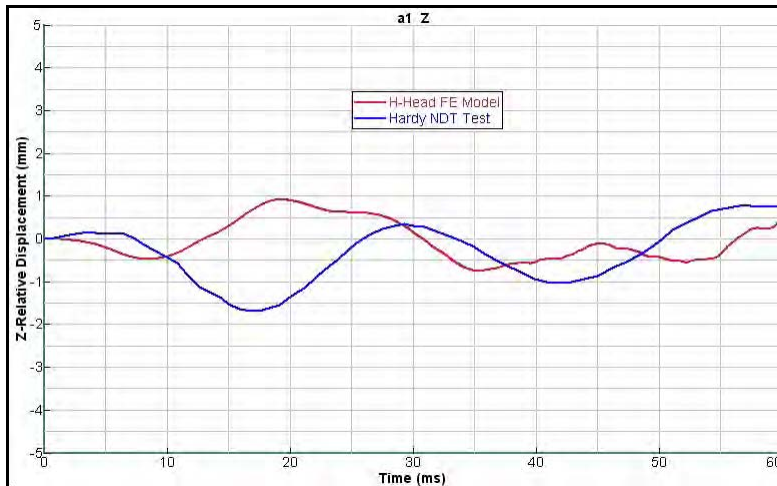


Figure 3-12 Z-displacement time history comparison at NDT-a1 for test C755-T2

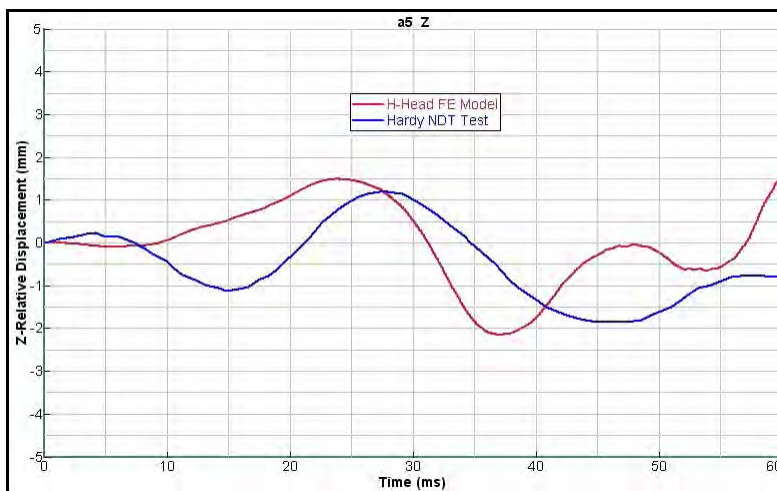


Figure 3-13 Z-displacement time-history comparison at NDT-a5 for test C755-T2

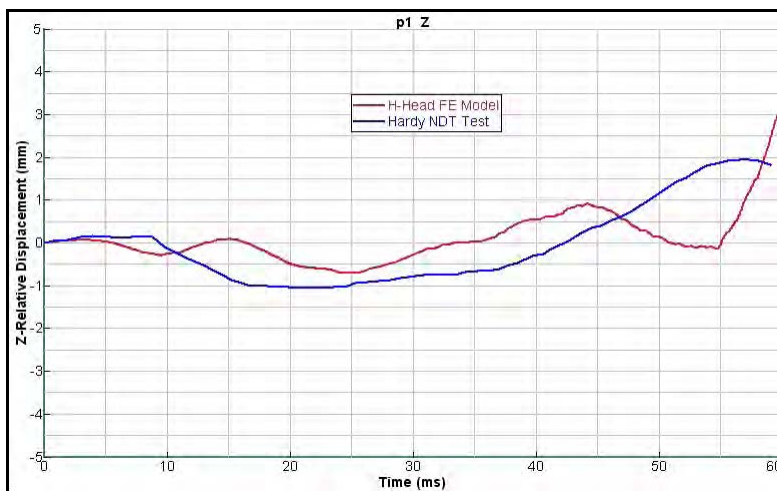


Figure 3-14 Z-displacement time-history comparison at NDT-p1 for test C755-T2

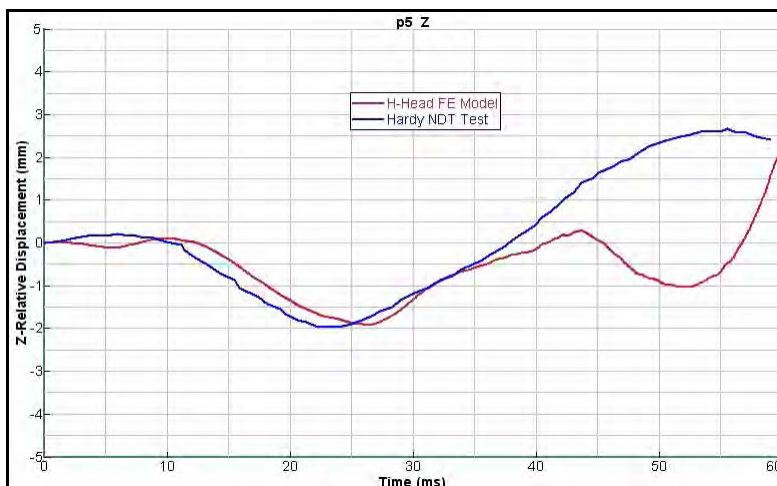


Figure 3-15 Z-displacement time-history comparison at NDT-p5 for test C755-T2

C383-T1 is a deceleration test in which a frontal impact was applied. In the model validation, both the translational and rotational acceleration time histories from NDT test were used as simulation input parameters. Figure 3-16 and Figure 3-17 show the input data verification of the translational and rotational acceleration with NDT test.

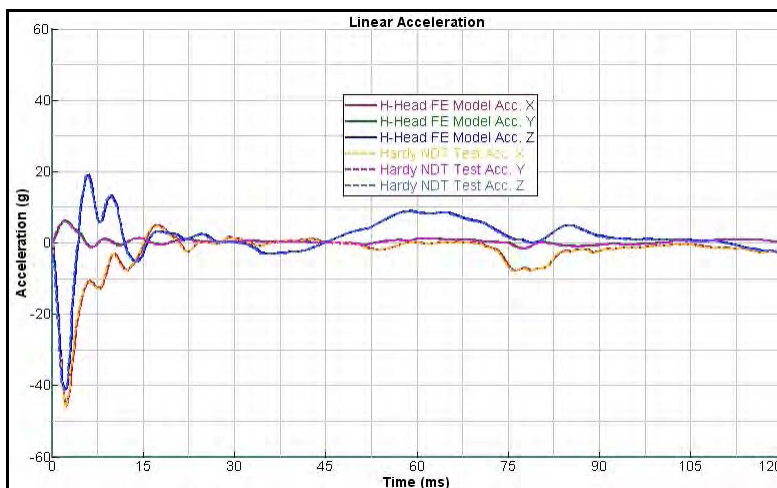


Figure 3-16 Verification of translational acceleration data for NDT test C383-T1

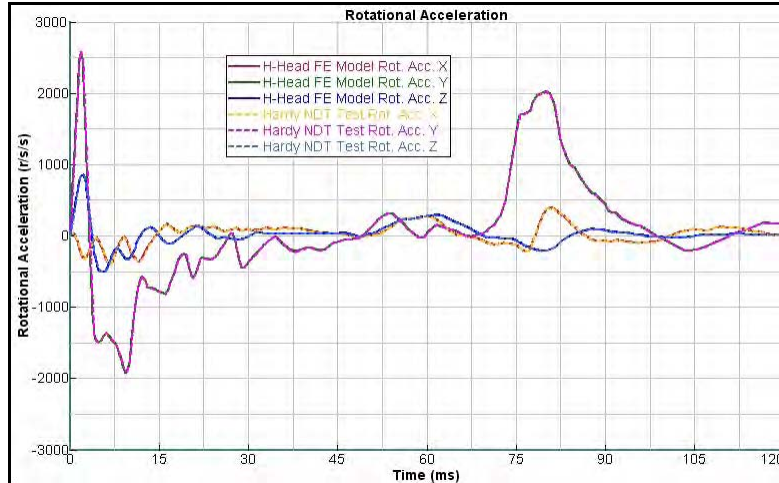


Figure 3-17 Verification of rotational acceleration data for NDT test C383-T1

For comparison between H-Head model results and NDT test data, the relative displacements of the brain at selected NDT locations (a1, a6, p1 and p6) are given in Figure 3-18 to Figure 3-25. Maximum displacement difference between calculation and test data is shown to be approximately 10 millimeters. Considering the difference of geometry dimension between test specimens and H-Head model, this difference is considered to be acceptable.

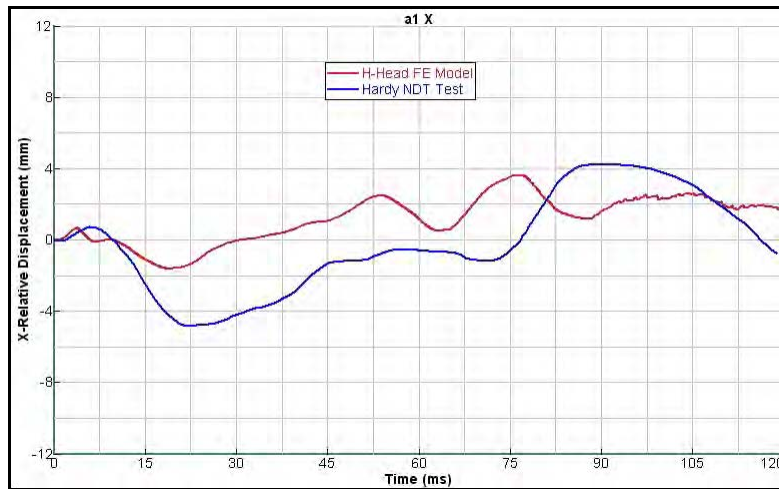


Figure 3-18 X-displacement time-history comparison at NDT-a1 for test C383-T1

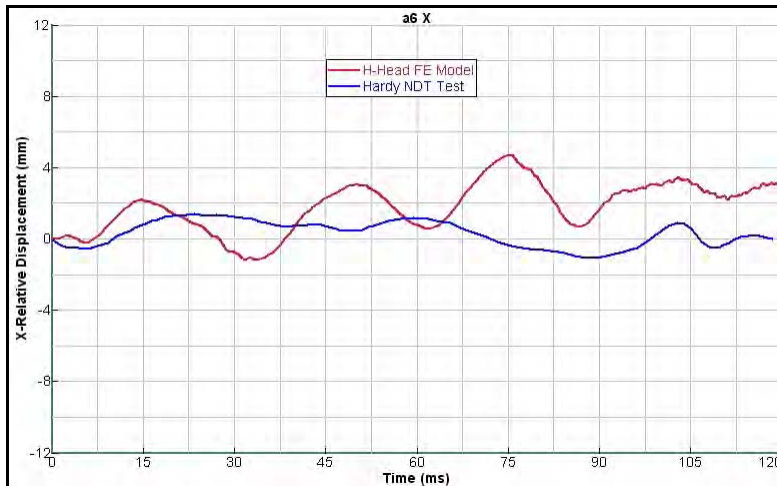


Figure 3-19 X-displacement time-history comparison at NDT-a6 for test C383-T1

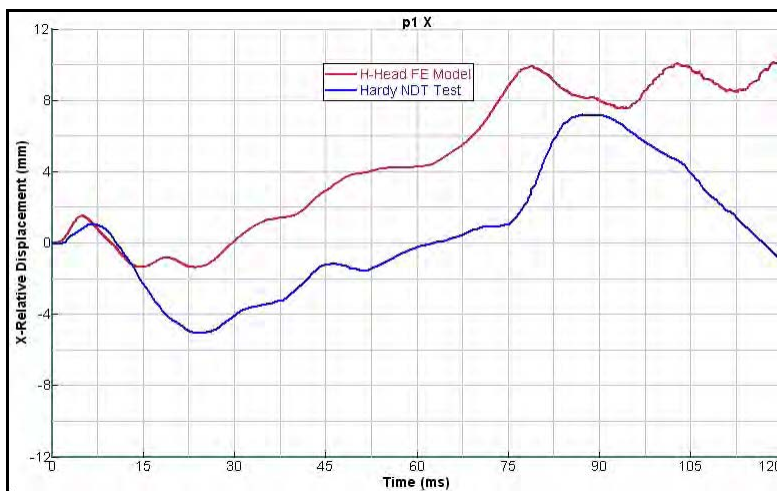


Figure 3-20 X-displacement time-history comparison at NDT-p1 for test C383-T1

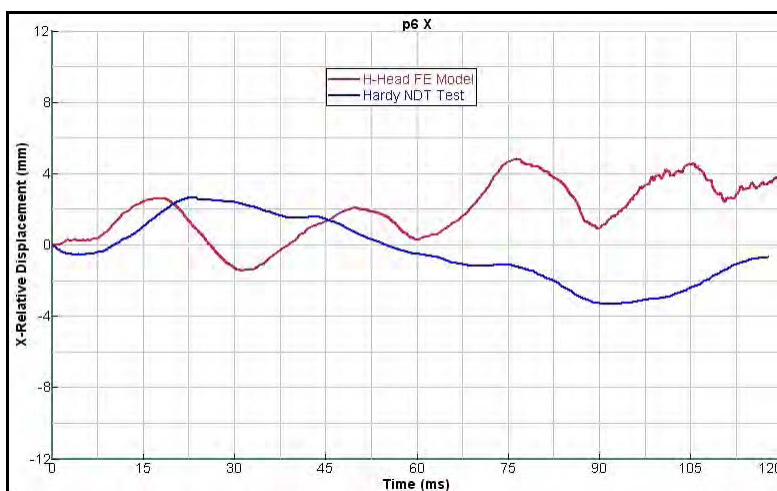


Figure 3-21 X-displacement time-history comparison at NDT-p6 for test C383-T1

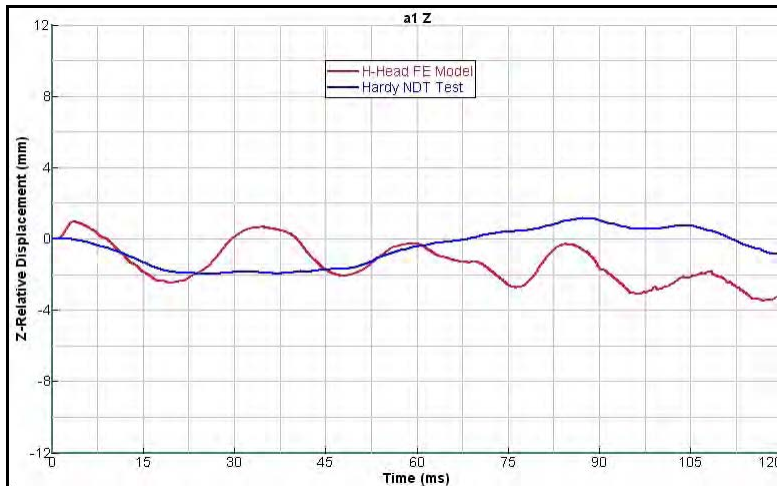


Figure 3-22 Z-displacement time-history comparison at NDT-a1 for test C383-T1

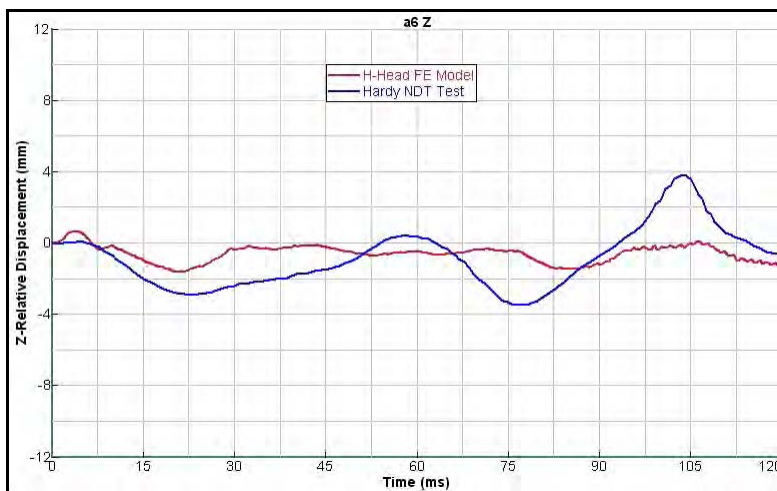


Figure 3-23 Z-displacement time-history comparison at NDT-a6 for test C383-T1

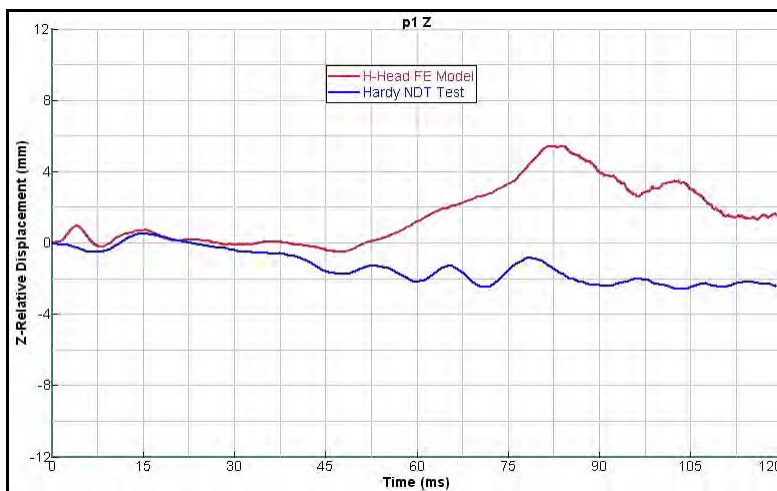


Figure 3-24 Z-displacement time-history comparison at NDT-p1 for test C383-T1

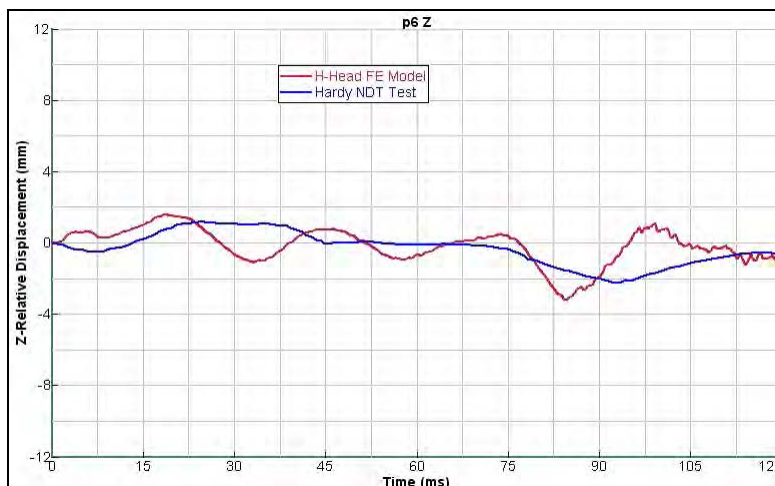


Figure 3-25 Z-displacement time-history comparison at NDT-p6 for test C383-T1

3.1.3 Conclusion for H-Head FE Model Validation against NDT Test

Comparison shows that the difference between ESI H-Head model results and NDT test data are relatively small, and are within the same magnitude level. The largest difference of displacement history was approximately six millimeters for test C755-T2 (Figure 3-10) and ten millimeters for C383-T1 (Figure 3-20). The similar trends and small difference displayed in displacement time histories imply the strain generated by impact should be also at the same level for ESI H-Head model and NDT tests. It can be concluded that validation results of ESI H-Head model v2007 against NDT tests are within acceptable ranges.

3.2 H-Head Model Validation against Head Impact Test

3.2.1 Nahum Head Impact Test Description

Nahum, Smith and Ward (1977) had conducted measurement of intracranial pressure during human head impact in which a seated and stationary cadaver was impacted by a rigid mass traveling at a constant velocity. In the tests, the skull was rotated until the Frankfort anatomical plane was inclined 45 degrees to horizontal (Figure 3-26) and the sequential impacts were delivered to the frontal bone in the midsagittal plane in an anterior-posterior direction. Various padding materials were interposed between skull and impactor to vary the duration of applied load. The impact force and biaxial acceleration-time histories of the skull were recorded during impact. By placing pressure transducers in planned locations inside dura matter, the intracranial-pressure time histories were recorded near the anterior bone, posterior, parietal and occipital regions.

Impactor mass and velocity combinations ranged from 5.23 to 23.09 kg and 8.41 to 12.95 m/s. Peak input force varied from 5.20 to 14.84 kilonewtons, which resulted in peak head acceleration from 1.52×10^3 to 3.90×10^3 m/s². High positive peak pressures were recorded beneath the impact site in the anterior region. The pressure magnitude decreased and eventually became negative as the area opposite the blow was approached. Because of the 45-degree-inclined setup, the head rotated no more than a few degrees when the peak pressure was attained.

3.2.2 FE Modeling Procedure and Results

ESI had performed H-Head model validation against Nahum's test. They used a circular-shape pendulum as the impactor by assigning a constant speed. Since the impactor dimension (impact area) and the padding material interposed between skull and impactor (as a damping part) are unknown, it was difficult to repeat the impact even when using the correct initial momentum.

To accurately transmit the impact pulse recorded in test into the head model, two alternative methods were proposed, one using frontal pressure loading segments, the other using prescribed acceleration at head CG.

To validate H-Head model against Nahum's tests, the following simulation procedure was used:

- Define the facial bone and mandible parts as a rigid skull if pressure loading method is used, including the outer table, inner table and dipole in skull if prescribed acceleration method is used.
- Identify the CG of H-Head model.
- Set up a local reference frame attached to the skull with the head CG as the origin. This reference frame is used for measuring relative motion of brain matter with respect to skull.
- Select loading method:
 - For loading method 1: Define a circular pressure loading area which is tied to frontal bone.
 - For loading method 2: Define the outer and inner table, dipole, facial bone, and mandible parts as a rigid body — skull.
- Apply loading to head
 - For loading method 1: Apply the pressure loading histories (converted from impact force-time history) on the circular loading area.
 - For loading method 2: Apply acceleration histories to the CG of skull.
- Run PAM-CRASH calculations and output results:
 - Output and verify the input force and acceleration curves.
 - Output intracranial pressure histories at specified regions and converted acceleration unit into g .
 - Compare calculated pressure results with Nahum's impact test data.

To validate the ESI H-Head model, test 37 was chosen, in which a 5.59kg impactor mass at an initial speed of 9.94 m/s impacted on the frontal bone in midsagittal plane in anterior-posterior direction.

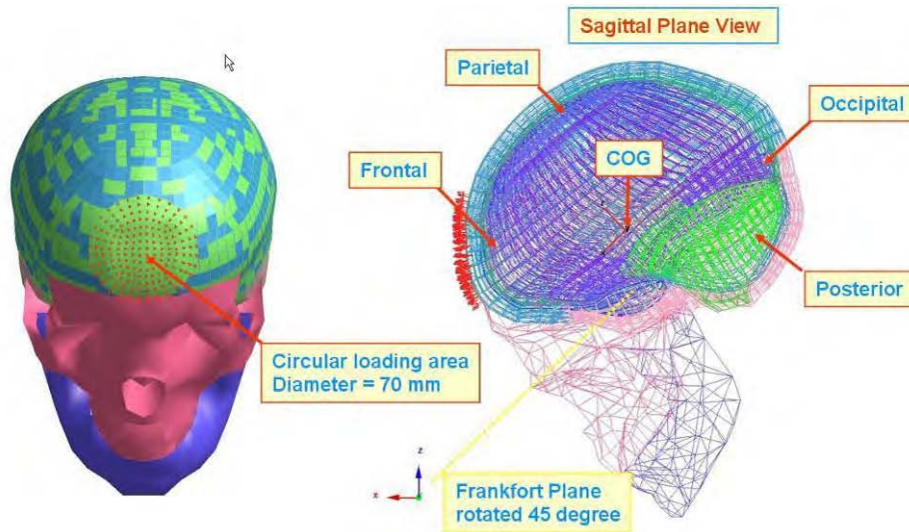


Figure 3-26 Impact loading area and pressure measured locations

To accurately transmit the impact pulse recorded in test 37 into the H-Head FE model, the pressure-time history was converted from the impact force-time history curve. The calculated impact force and head acceleration history results in Figure 3-27 and Figure 3-28 correlate well with the test data.

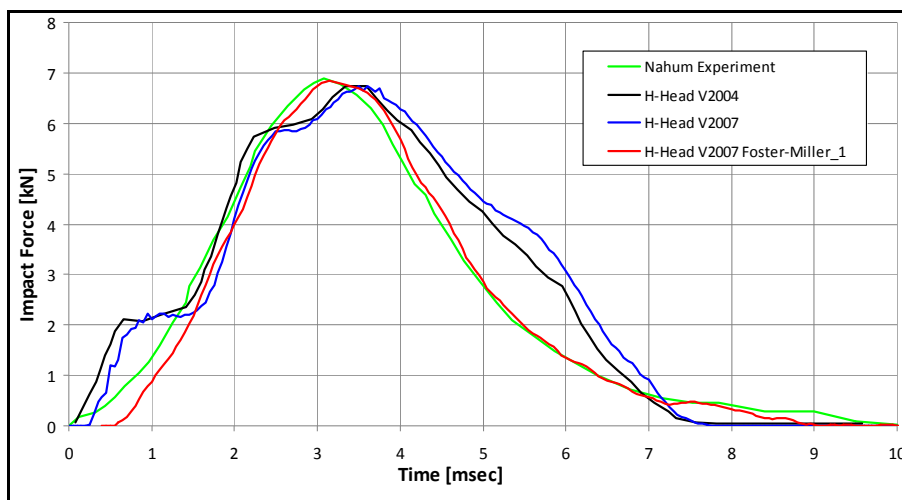


Figure 3-27 Verification of input force-time history with test data

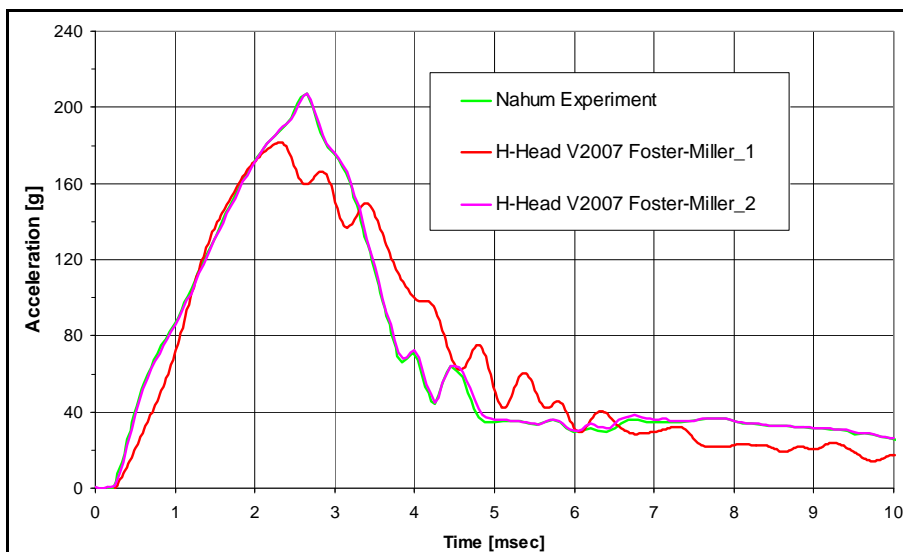


Figure 3-28 Head acceleration time history comparison

Figure 3-29 to Figure 3-32 compares intracranial pressure time histories in anterior, posterior, occipital and parietal regions. It proves that both proposed loading methods generated better results than previous pendulum impact method. Furthermore, acceleration method produced the best results. For instance, peak pressure difference in anterior region was 23 kPa by pressure loading and 1 kPa by acceleration loading; peak pressure difference in parietal region was 21.5 kPa by pressure loading and 10.8 kPa by acceleration loading. It indicates that the proposed methods can transfer the impact momentum more accurately than traditional methods, since the proposed methods avoid many unknowns such as impactor padding, impact area, loading angle and others.

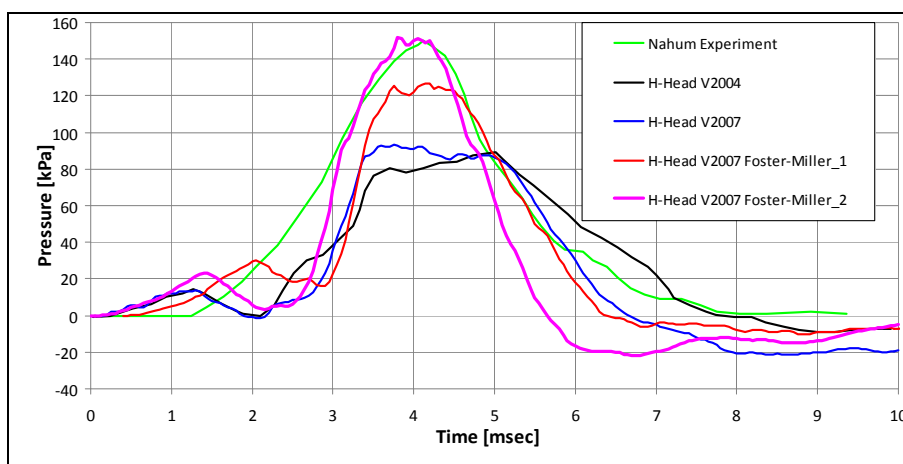


Figure 3-29 Intracranial pressure time history plots in anterior region

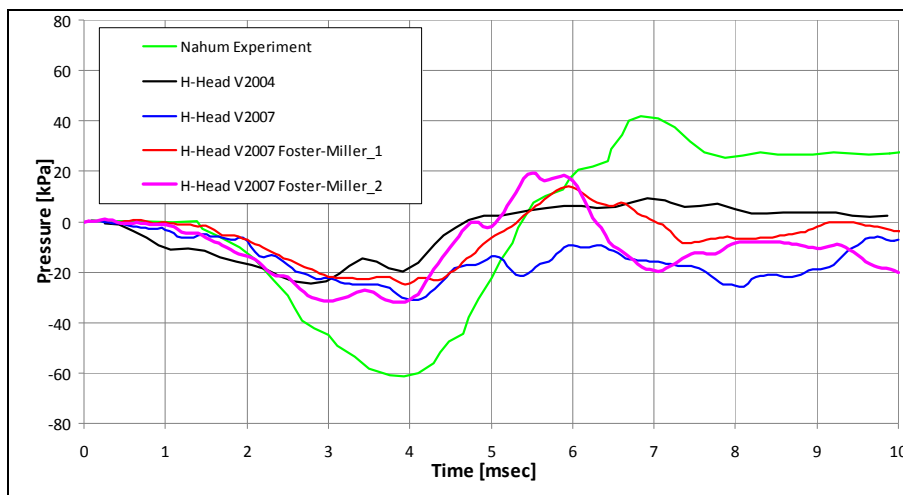


Figure 3-30 Intracranial pressure time history plots in posterior region

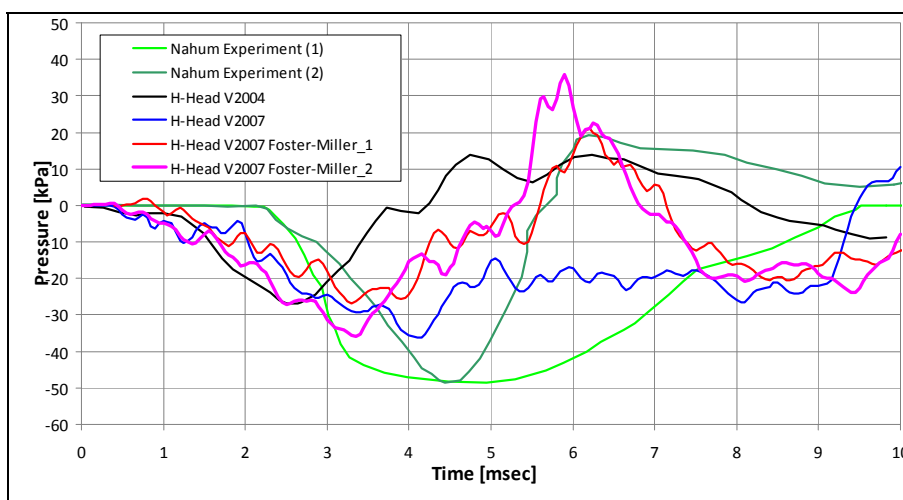


Figure 3-31 Intracranial pressure time history plots in occipital region

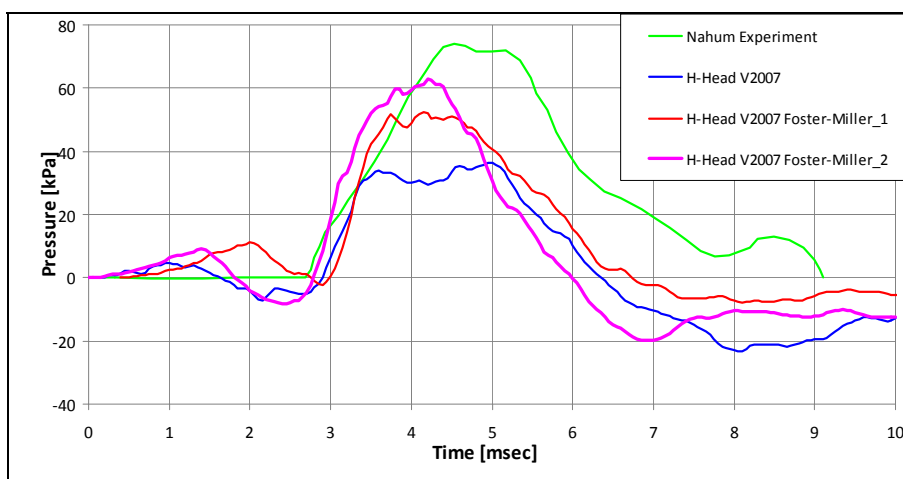


Figure 3-32 Intracranial pressure time history plots in parietal region

3.2.3 Conclusion for H-Head FE Model Validation against Nahum's Test

Using the proposed pressure or acceleration loading methods, impact momentum was transferred correctly. Validation shows reasonable correlation between results of H-Head model and Nahum test 37. Both methods demonstrated better matching with test data than ESI's pendulum method.

An important implication is that applying head acceleration on the head CG is essentially equivalent to applying impact force or pressure loading on the outer surface of H-Head model. In both methods, the head has similar kinetic response. Compared with the contribution by head rigid body motion to brain deformation, the contribution by skull deformation under impact or pressure is neglected since the skull is relatively stiff.

4. Brain Injury Metrics

Currently the only widely accepted injury metric available to evaluate for the possibility of head injuries is the head injury criterion (HIC). HIC relates the resultant translational acceleration to skull fracture. However, more head injuries are seen where injury is caused to the brain without skull fracture.

In this section, three of the most common types of injury metrics are examined here: Cumulative strain damage measure, correlate for diffused axonal injury (DAI); dilation damage measure, to estimate the potential for contusions; and relative motion damage measure (RMDM), a correlate for acute subdural hematoma (ASDH). Data from animal experiments were used to determine critical values for each injury metric. In order to apply this data, the linear and angular kinematics recorded for the animal's head were scaled in magnitude and time to what a human would experience.

Cumulative Strain Damage Measure (CSDM). Introduced by Bandak and Epinger (1995), CSDM is a widely accepted brain injury metric in TBI analyses. It is based on the hypothesis that DAI is related to the cumulative volume of brain tissue experiencing tensile strains over a critical level (Gennarelli et al. 1982, Meaney et al 1993, Takhounts et al. 2003). The CSDM metric predicts brain injury severity by monitoring the accumulation of strain damage. The CSDM level is calculated at each time step: it represents the volume fraction of brain tissue experiencing maximum principal strain over a prescribed threshold. CSDM levels range from 0 to 100% with the critical value of tensile strain being 15% based on the *SIMon theoretical manual*. The related volume fraction was chosen as 5.5% and 22.5% for mild DAI and moderate DAI, as recommended by ESI. CSDM was the primary injury metric used in this project and was considered to be the best representation for the potential of TBI.

Dilatation Damage Measure (DDM). DDM involves localized regions where stress states in the brain result in negative pressures, exceeding values large enough to produce contusions and tissue damage, often found in countercoup injuries. DDM monitors the volume of the brain experiencing specified negative pressure levels. Similar to the CSDM calculation, the final result is the percent of brain volume that has experienced a negative pressure level exceeding a prescribed threshold value sometime during the event. This pressure threshold is set at -100 KPa, the vapor pressure of water. The spatial distribution of the affected volume of brain mater reaching this negative pressure value indicates a higher possibility of contusions. Animal impact tests from Stalnaker et al. (1977) and Nusholtz et al. (1984), along with the physical model study of Nusholtz et al. (1995), were used to establish the injury threshold for DDM. DDM was calculated in all simulations performed; however, there were no instances of brain volume experience a negative volume pressure exceeding -100 KPa.

Relative Motion Damage Measure (RMDM). RMDM is used for the evaluation of injuries caused by brain motion relative to the interior surface of the cranium. This includes injuries due to acute subdural hematoma (ASDH). The metric accounts for the large-stretch modes of rupture of the bridging veins, while leaving open the possibility of using other micro or macro rupture modes associated with more complex vascular tethering states. The RMDM also incorporates the dependence of bridging vein-stretching rupture on strain rate. However, unlike CSDM and DDM, RMDM is not an integral measure of

injury and thus depends highly on the geometry of the head, and thus the FE model. Therefore, RMDM was not used as an injury metric in this project.

5. Blast Overpressure Simulation Methods

5.1 Blast Overpressure Simulation Methods

A critical aspect in analyzing mechanisms of blast-wave-induced TBI is to realistically generate the pressure loading applied on the targets. There are basically two types of methodologies for modeling blast effects:

1. Apply the blast pressure time history on the specified target surface. These history curves can be obtained from special codes such as BlastX and ConWep which are empirical formulations based on field experimental data. For a given charge type and weight, one can use these codes to calculate the blast air-pressure time history acting on a target at a given standoff and height. This type of method has the following advantages:
 - a. Calculation of the loading process is fast — pressure can be directly applied to target surface;
 - b. No interface action between air and target needs to be considered;
 - c. Pressure data are accurate enough for targets with simple geometry and loading path, since they are based on experiments.

However, this method may not be suitable for a fast-moving target, since it cannot account for pressure variation due to the target motion occurring in loading process.

2. Explicitly model the blast wave by hydrodynamics codes, such as SPH method in PAM-SHOCK and in LS-DYNA, ALE method in LS-DYNA, FCT method in Autodyn, and CTH code by Sandia Laboratory. These hydrodynamic codes are based on shock physics and computation is governed by equation of state (EoS), among them SPH, a meshfree Lagrangian method, and Eulerian methods FCT in Autodyn and CTH by Sandia. These types of methods show strength in solving problems where the target geometry is not simple and blast pressure wave paths are complicated. It typically is a CPU-intensive process due to the large number of elements involved in the calculations.

5.2 Evaluation of SPH Method in PAM-SHOCK

SPH (smoothed-particle hydrodynamics) is a mesh-free Lagrangian particle method for solving dynamic problems. This n -body integration scheme was initially developed by Lucy (1977) and Gringold and Managhan (1977) for solving astrophysical problems in an open space. It has some advantages over the traditional grid-based numerical methods, the finite-difference method (FDM) and finite-element method (FEM). For instance, it can avoid mesh-tangling issues encountered in extreme deformation problems. This method has no fixed connectivity; particles interact with one another by an interpolation function. In PAM-SHOCK or LS-DYNA, users can combine SPH method and JWL explosive material along with air material property to explicitly model the air blast-wave propagation caused by explosion. This method has the following advantages:

1. Air particles are scattered onto the target and apply pressure by contact interface — there is no need to predefine the pressure-loading segments on target;

2. Air particles will automatically follow the moving target, which might naturally adjust the pressure on the target;
3. Blast-wave propagation effects can be viewed explicitly.

This method uses significant computational resources for calculations involving large numbers of air-particle-to-air-particle interactions and air-particle-to-target-contact interfaces. To evaluate the suitability of using SPH for this study much effort has been given for evaluation and validation.

First, mesh dependency of the SPH method for blast simulation was studied. A one cubic meter space, which represents only a quarter model, was discretized into SPH meshes by two different mesh sizes. In the coarse mesh, each SPH particle represents a 2.5cm^3 air space (left block in Figure 5-1); in the fine mesh, each particle represents a 1.25cm^3 air space (right block in Figure 5-1). The 6.25 kg TNT charge (only 1.63kg TNT was used by symmetry) was located at the origin of coordinate system, and all boundary plates were fixed in space. The simulated blast wave propagations by SPH method in PAM-CRASH (Figure 5-2) showed that the average overpressure in the fine mesh model is higher than that in the coarse mesh model, though there is no obvious difference in the speed of the wave front. The time history records of contact force between air particles and target pads also indicate the fine mesh generated higher average force values than the coarse mesh (Figure 5-3).

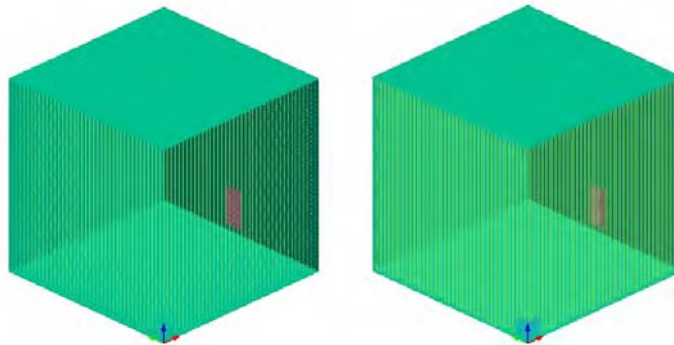


Figure 5-1 Coarse mesh (2.5cm^3) and fine SPH mesh (1.25cm^3) for 1 m^3 space

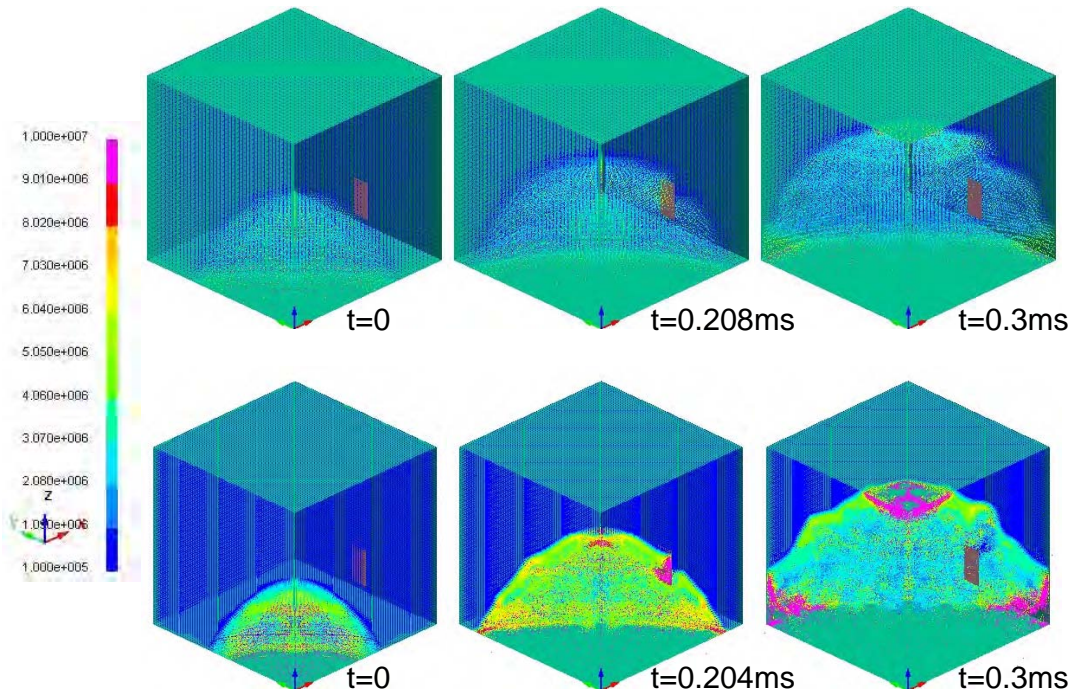


Figure 5-2 Blast pressure wave propagation simulated by coarse (upper) and fine meshes (lower)

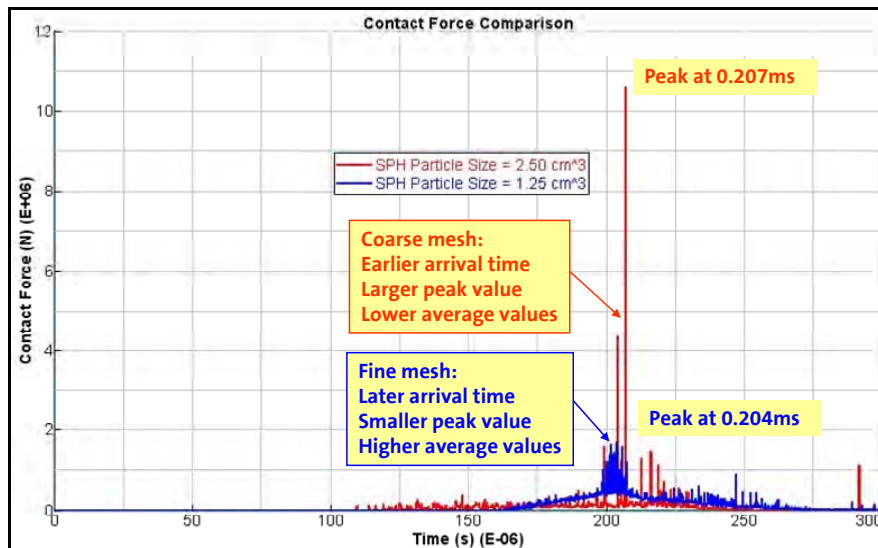


Figure 5-3 Contact force between SPH particles and targets for coarse and fine meshes

Second, prediction accuracy of SPH method for blast simulation was studied. This will compare several aspects of SPH method with empirical methods, including their predictions in peak pressure, arrival time, peak particle density and velocity. To avoid other analysis noise, a simple free-air burst simulation was considered. The charge is 6.25kg TNT at 1.2m (burst height) from ground and 1.0m (standoff) from target wall. The predicted pressure time history curves by BlastX and by ConWep (both are based on empirical formula) are well-matched; for example, in both curves the wave front arrived at approximately 0.325 milliseconds and the peak reflected pressures were around 23 megapascals (Figure

5-4). To compare SPH method with empirical methods, a quarter-model for a space of $1.0 \times 1.0 \times 2.4 \text{m}^3$ was calculated with two symmetry planes at $x = 0$ and $y = 0$ (Figure 5-5). Fixed boundaries were defined at $x = 1.0 \text{m}$, $y = 1.0 \text{m}$, and $z = 0$ and 2.4m .

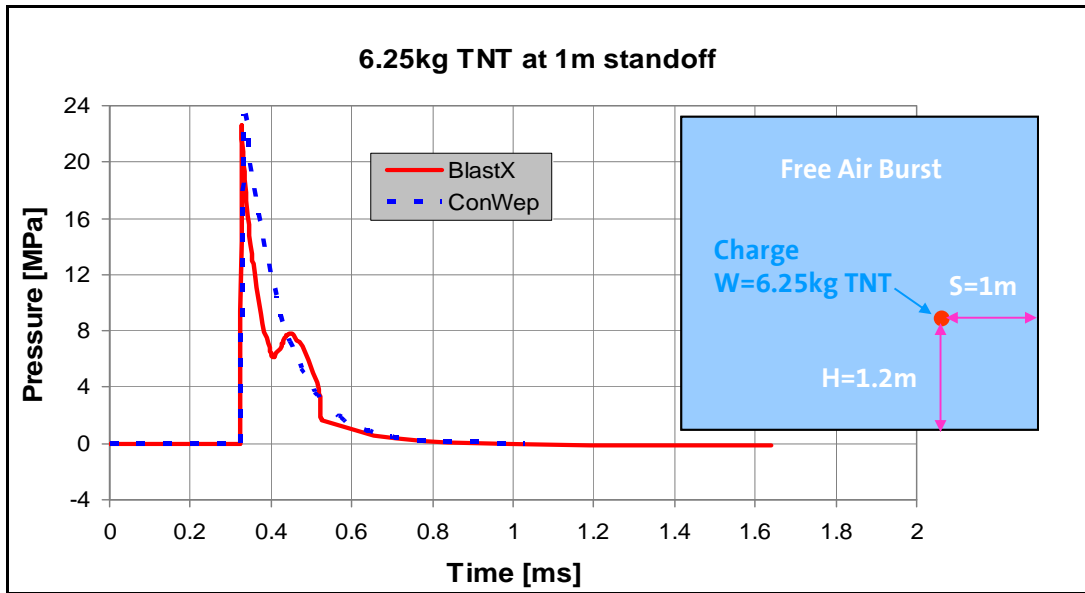


Figure 5-4 Reflected pressure time histories for 6.25 kg TNT at 1 m standoff

For free-air burst simulation, a charge of 1.536 kg TNT was detonated at $x = y = 0$, $z = 1.2 \text{m}$. Pads were fixed on the wall for monitoring contact force between particles and pads. The middle pad at $z = 1.2 \text{m}$ corresponds to the target location specified in the BlastX and ConWep calculations. For the designed model, blast wave will first arrive at vertical walls at $x = 1 \text{m}$ and $y = 1 \text{m}$. Pressure wave propagation by PAM-SHOCK calculation is shown in Figure 5-6. It can be seen that the wave front arrived at target wall around 0.32ms which agrees to the BlastX or ConWep results. Figure 5-7 shows the fringes of particle density, pressure and velocity at the time attaining their peak values.

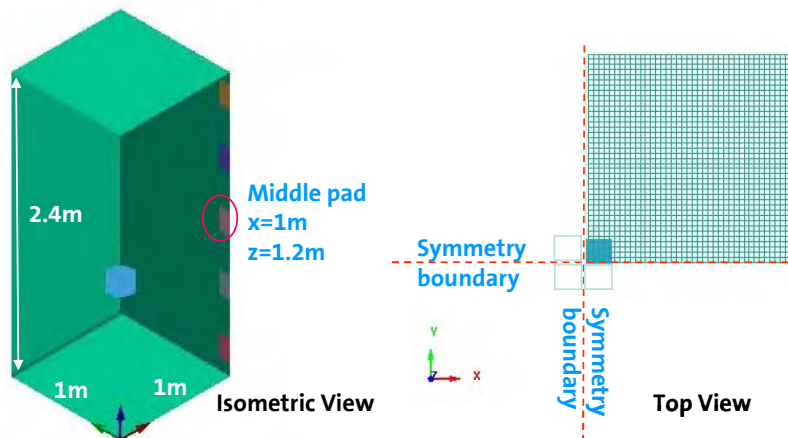


Figure 5-5 Dimension and boundary conditions of the quarter model

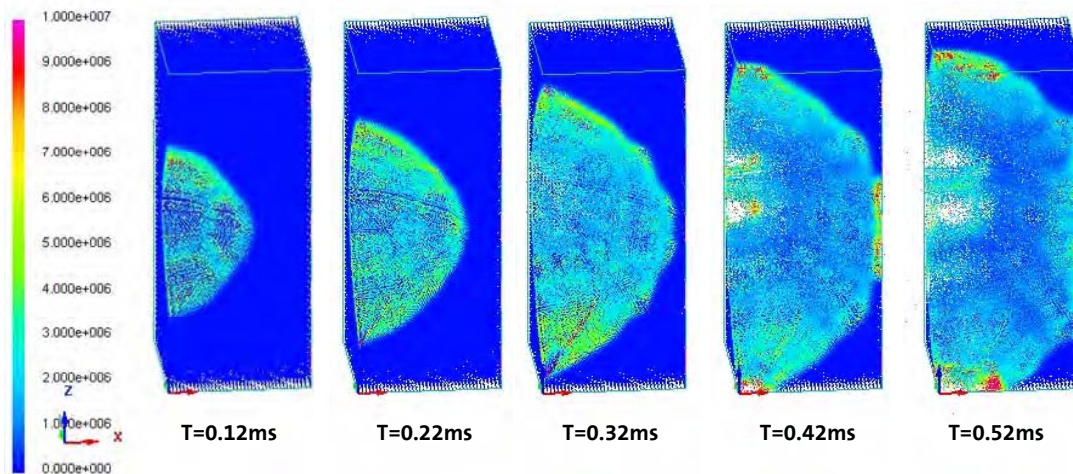


Figure 5-6 Pressure wave propagation by SPH method

Details of time history for selected SPH particles just in front of the middle pad can be found in Figure 5-8, Figure 5-9 and Figure 5-10. From the curves plotted in these figures, the SPH method predicted the peak particle density (6.76 kg/m^3) and peak particle velocity (1381 m/s) as very close to the values predicted by ConWep (Table 5-1). However, the peak reflected pressure by SPH is about 70% less than that of ConWep. Contact force between air particles and middle pad is not a smooth curve as shown in Figure 5-11. The maximum impulse calculated from contact force is about 1.42 MPa-ms.

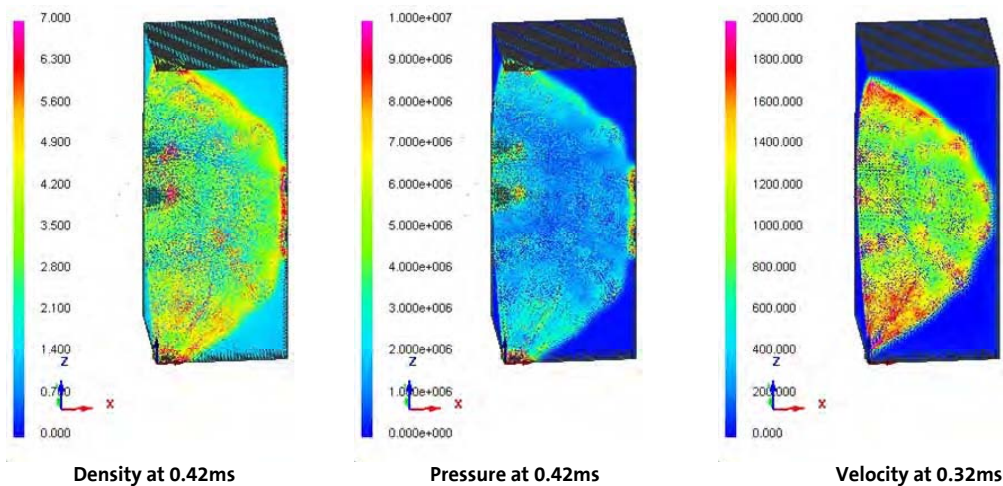


Figure 5-7 Density, pressure and velocity fringe at peak values

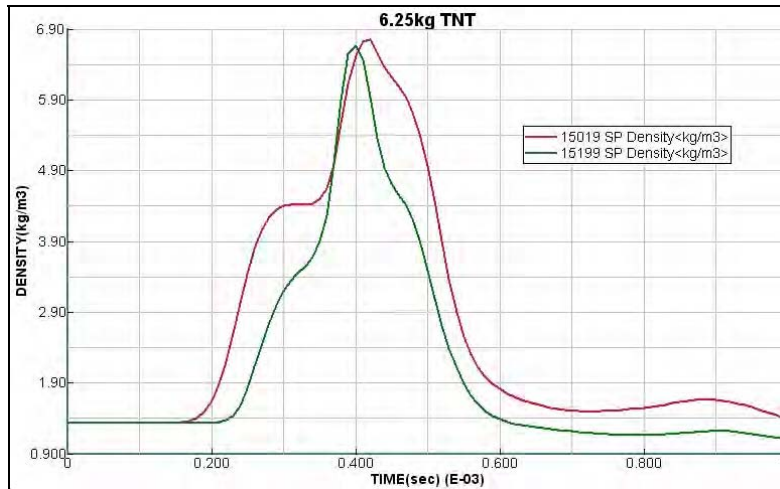


Figure 5-8 Density time histories of selected SPH particles in front of middle pad

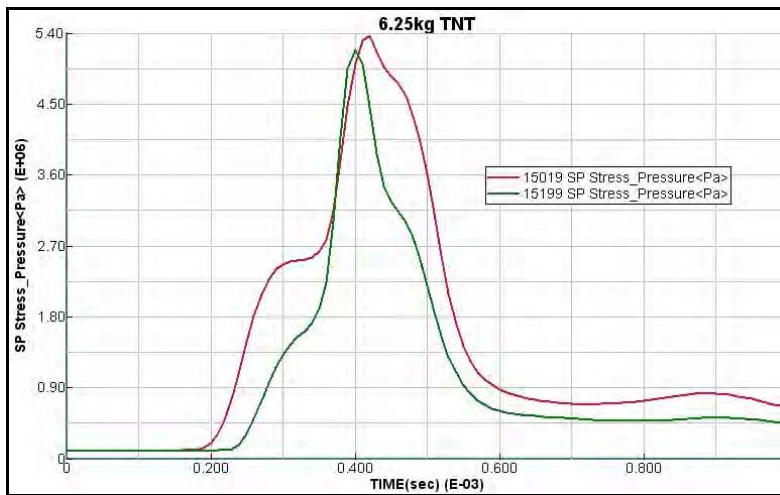


Figure 5-9 Pressure time histories of selected SPH particles in front of middle pad

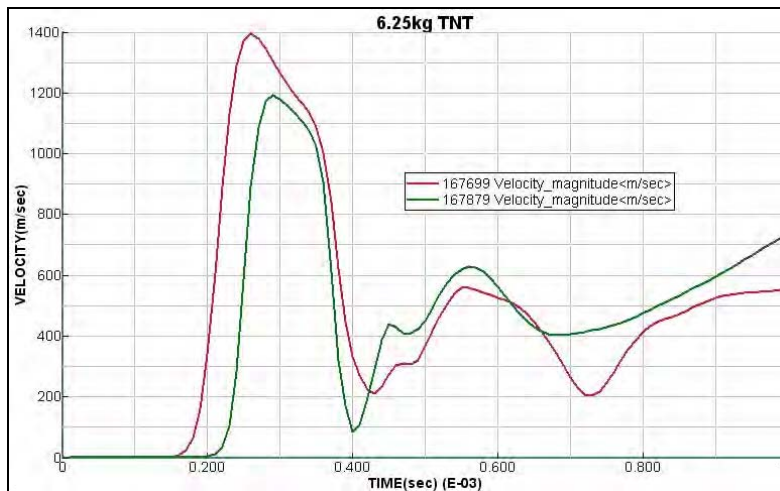


Figure 5-10 Velocity time histories of selected SPH particles in front of middle pad

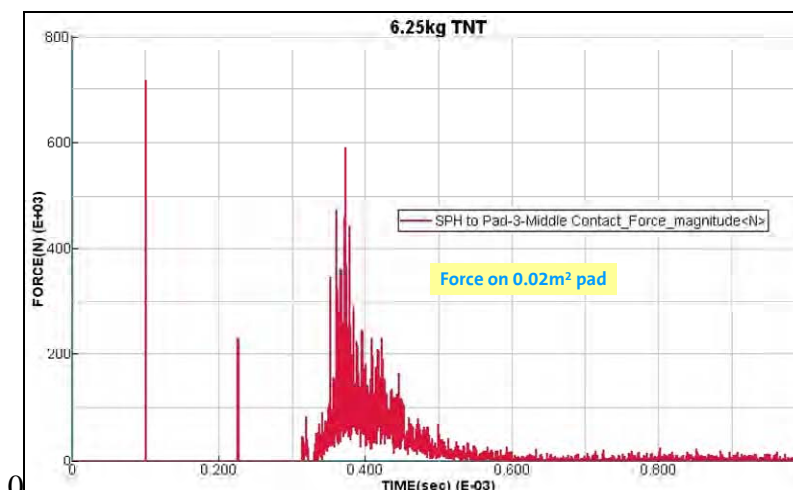


Figure 5-11 Contact force time histories between particles and middle pad

Table 5-1 Comparison of results from different methods for 6.25kg TNT

Method	Peak pressure (MPa)	Total impulse (MPa-ms)	Arrival time (ms)	Peak particle density (kg/m ³)	Peak particle velocity (m/s)
BlastX	22.7	2.42	0.325		
ConWep	23.4	2.38	0.326	6.995	1497
PAM-SHOCK	5.36	1.42	0.313	6.76	1381

5.3 Comparison of SPH (PAM-SHOCK), ALE and ConWep (LS-DYNA)

To choose the best blast loading approach currently available to this project, three different loading methods have been compared in efficiency and accuracy, SPH method in PAM-SHOCK, ALE method and ConWep function in LS-DYNA.

LS-DYNA has embedded ConWep code in its *load_blast* function. By defining the loading segments, charge weight, standoff and loading scenario, LS-DYNA can calculate blast load pressure through ConWep directly. For each loading segment, the function will consider the incident angle (between the radial direction from detonation and the target surface normal) and apply a combination of incident pressure and reflected pressure on that segment based on the incident angle.

For 20kg TNT 2 to 3ft away on the ground, the explosion may generate a blast pressure wave with a positive duration for less than one millisecond to no more than 12 ms. During such a short loading phase, the distance of a loaded object can travel no more than 20 mm. Therefore, it is reasonable to ignore the decrease in reflected pressure caused by target motion.

Since *load_blast* in LS-DYNA uses empirical code instead of modeling air particles explicitly, it use less computational time and there is no need to change the finite-element mesh when the HE charge is changed.

Due to the symmetry feature of the problem, only quarter-models have been analyzed, as shown in Figure 5-12. The symmetry plane boundary conditions were adopted at x = 0 and

$y = 0$. This can save computational cost without losing any significant information. For SPH and ALE simulations, a volume of $1.2 \times 1.2 \times 2.8 \text{ m}^3$ was discretized into 258,048 SPH air particles or ALE elements. Each air particle or element size represents a $2.5 \times 2.5 \times 2.5 \text{ cm}^3$ space. Same model space would use more than 2 million elements if a mesh size of $1.25 \times 1.25 \times 1.25 \text{ cm}^3$ was considered. For pressure-loading method using ConWep function in LS-DYNA, there is no need for air space discretization. However, loading segments should be predefined on the target surface.

The target was taken as a rigid 2mm-thick shell sphere with a diameter of 0.2m and mass of 1.995kg. The sphere was free to move under blast pressure. In the simulation, a high explosion charge equivalent to 5.4kg TNT was detonated at the center of the model. The nearest distance from sphere surface to detonation center was 0.607m.

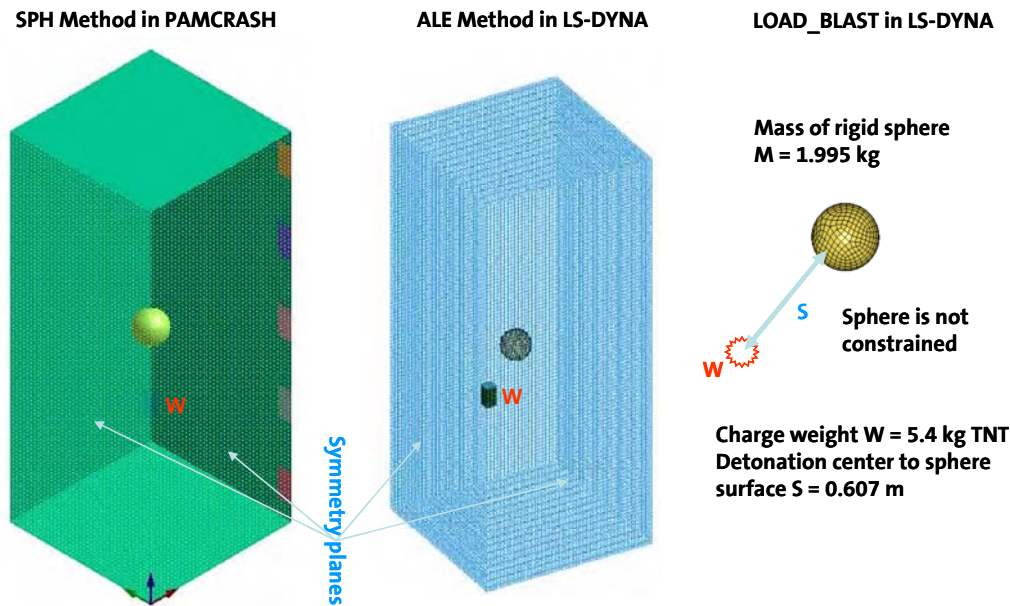


Figure 5-12 Model and boundary condition for air-sphere interaction simulation under blast pressure

Simulation results showed that reflected pressure was greatly reduced within a half millisecond. The peak reflected pressure given by ConWep was 64 MPa. By contrast, the peak reflected pressure recorded in SPH and ALE simulation were 10 MPa and 17 MPa, which are much lower (Figure 5-14). Under such strong blast impulse, the peak acceleration of rigid sphere can attain a level of 36,500 g (Figure 5-15 and Figure 5-16). However, as the positive blast pressure duration was less than a half-millisecond, the sphere can be accelerated only to a maximum velocity of 27 m/s (Figure 5-17). At such a velocity, a rigid sphere in first half-millisecond can move no more than 10mm (Figure 5-18). This implies decrease of reflected pressure due to the target motion, which can be ignored for this case. Assume the momentum loss of ConWep method to be negligible, ALE and SPH method lose 35.6% and 41.4% momentum (Table 5-2) in sequence. This can be improved by finer SPH or ALE meshes (mesh refining for both air and HE material). For a general blast injury problem, the explosion charge is about 2~10m from the target. It would require at least one million particles or elements for air-space discretization surrounding the target if using $2 \times 2 \times 2 \text{ cm}^3$ mesh size for either ALE or SPH methods. Currently, this is not practicable, owing to

limitations in computational resources. As a result, the ConWep function in LS-DYNA was used in this project for applying blast pressure on targets.

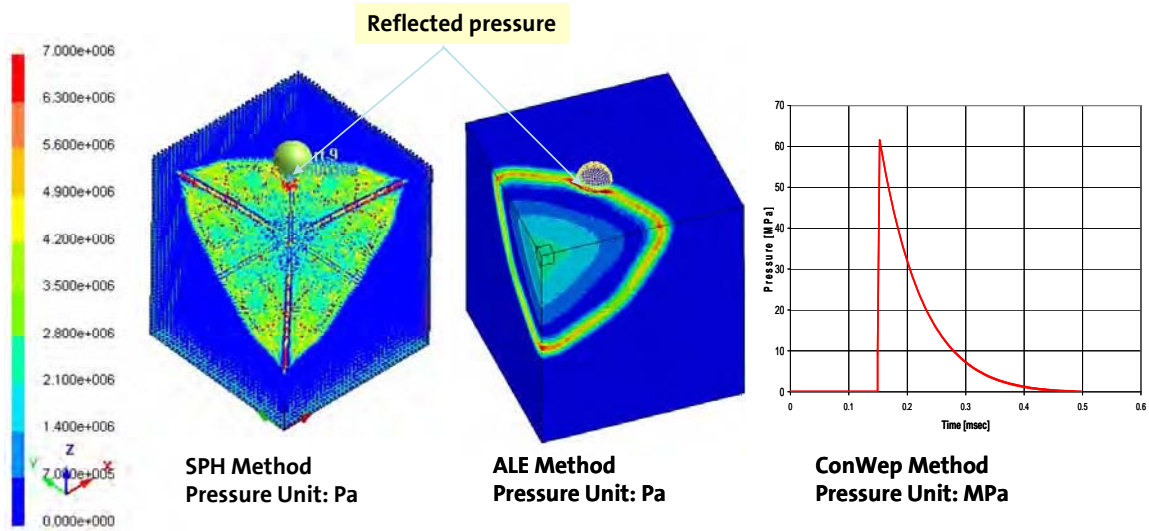


Figure 5-13 Pressure fringes at 0.22 ms after detonation

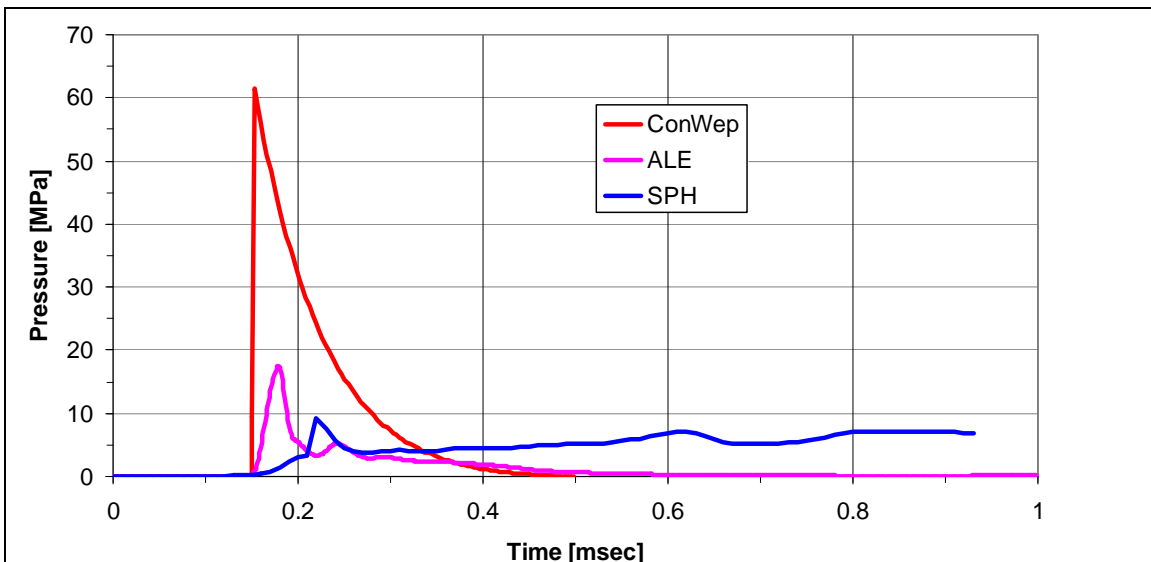


Figure 5-14 Reflected pressure time history comparison

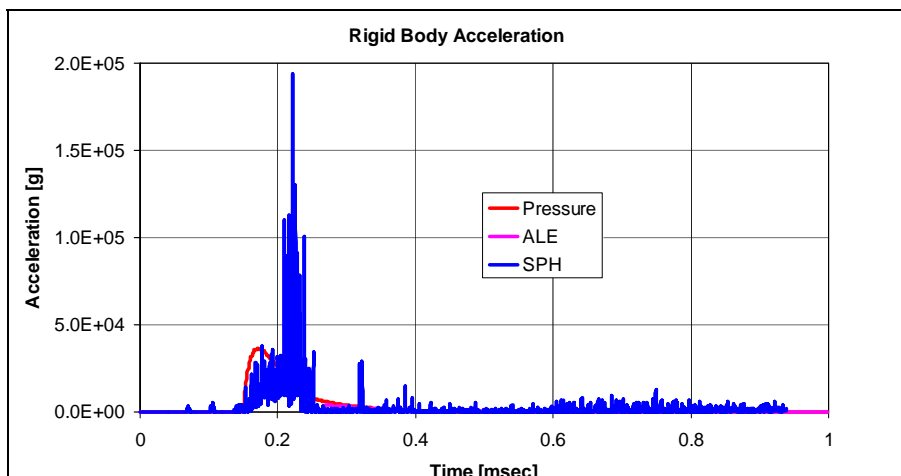


Figure 5-15 Rigid body acceleration time history of sphere by different methods

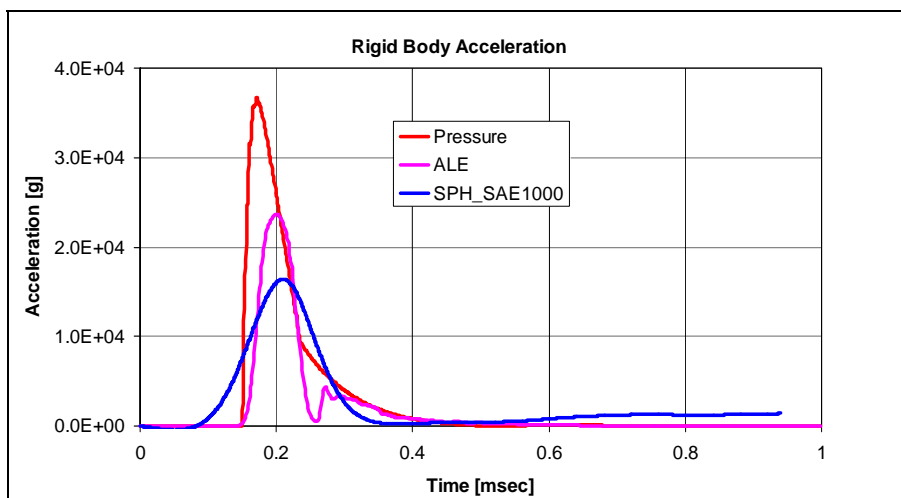


Figure 5-16 Rigid body acceleration time history comparison (SPH curve by SAE 1000)

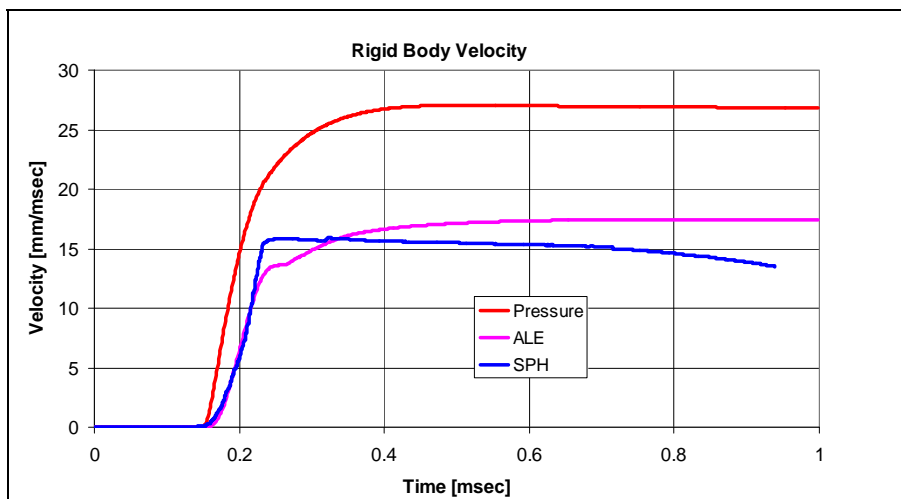


Figure 5-17 Rigid-body velocity time history comparison

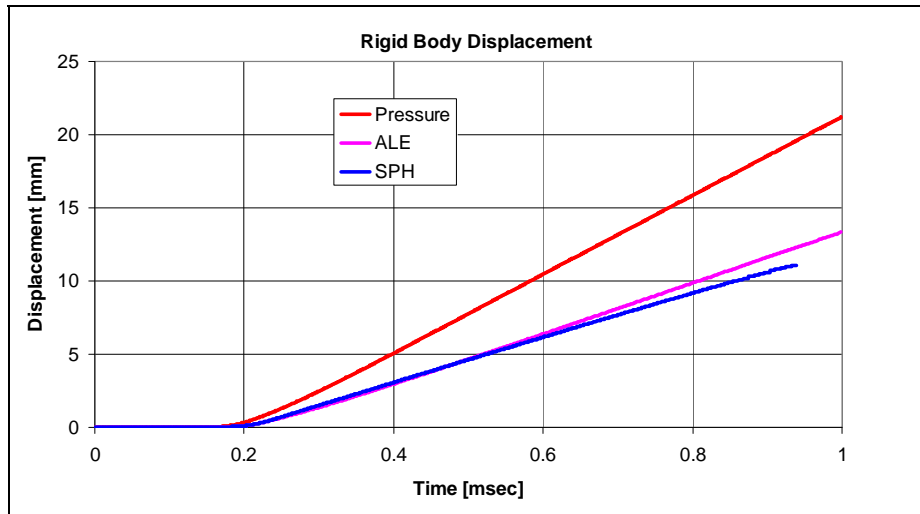


Figure 5-18 Rigid-body displacement time history comparison

Table 5-2 Comparison of blast pressure simulation results by different methods

Pressure Loading Method	Peak Reflected Pressure (MPa)	Peak Velocity by Blast (m/s)	Peak Momentum Obtained (kg•m/s)	Momentum Loss* (%)
ConWep	64	27.0	54	0
ALE	17	17.4	34.8	35.6
SPH	10	15.9	31.7	41.4

*Loading by ConWep is taken as base case (assuming 100% momentum is kept)

5.4 Blast Simulation Conclusion

SPH is a relatively new method used for three-dimensional air-blast simulations, and some effort has been spent on SPH model validation. Numerical practice shows the following facts:

- The number of SPH particles will be significant (in excess of 1 million elements) if fine mesh size is used, which will be computationally expensive.
- Mesh-dependent solution exists if using coarse mesh (centimeter-level mesh size).
 - Coarse mesh can result in larger peak pressure by the impacts from large particles (large mass) but lower average pressure (sparse particle matrix).
 - In contrast, fine mesh can produce higher average pressure because of dense particle distribution but lower peak pressure (less mass of each particle).
- Averaged reflected blast pressure by SPH method is much lower than predicted by BlastX and ConWep. Pressure time history curve (as well as contact force curve) has many spurlike peaks if coarse meshes are used. These peaks represent impacting events of multiple particles.
- SPH method can predict blast wave arrival time close to that from BlastX or ConWep.

- Few SPH particles can also have peak density, peak particle velocity close to the peak values by ConWep.

Most previous blast simulations using SPH method were performed on two-dimensional problems. Using SPH method for three-dimensional blast wave simulations is possible but requires significant computation resources. Among three pressure-loading methods that are currently available to this project, ConWep is the best choice.

6. Parametric Simulations of Primary Blast Injury

As mentioned, primary blast injury is directly caused by the effect of blast overpressure on human tissue. In general, primary injury is to air-filled organs such as lung, ear and the gastrointestinal tract (Pennardt et al., 2009). However, a primary blast can also cause obvious relative motion of brain matter in the skull. Shear, tension and compression forces related to such motion can possibly cause TBI including concussion, hemorrhage, edema, and diffuse axonal injury.

In this section, a parametric study was performed to identify the effect of blast impulse on the extent of damage to the brain, using CSDM as the injury metric, as a direct result of primary blast overpressure (no impact event). Furthermore, the study will focus on the mechanical behavior of the brain under blast loading and will not cover any other effects such as gas emboli formation or high-temperature burning.

6.1 Simulation Procedure of Primary Blast-Induced TBI

Since there is no suitable method for blast pressure loading in PAM-CRASH, all simulations in the parametric study were performed in two stages. In the first stage, calculations were executed using ConWep function in LS-DYNA with a Hybrid-III dummy model (developed by LSTC). The primary objective of this stage is to obtain the kinetic head data. The dummy was seated and blast pressure applied directly to the dummy's upper body surface (Figure 6-1). Upon completion of the LS-DYNA calculations, the head kinetic data including acceleration, velocity, and momentum were extracted and transferred to the ESI H-Head FE model in PAM-CRASH for the second stage of calculations. The second stage takes advantage of geometry and material properties of the ESI H-Head model to obtain stress and intracranial pressure, including the CSDM injury metric. The simulation procedure is summarized as follows:

Simulation Procedure

1. LS-DYNA calculation:
 - Define pressure-loading segments on dummy outer surface.
 - Define input parameters for *load_blast* function (ConWep) for a given charge weight and standoff.
 - Perform LS-DYNA simulations.
 - Analyze calculated results and output translational and rotational acceleration, and velocity time history data in all x, y and z directions.
 - Convert these time history data into PAM-CRASH curve format for next step.
2. PAM-CRASH calculation:
 - Define the outer and inner table, dipole, facial bone, and mandible parts in H-Head model as a rigid body – skull
 - Set the CG of the head as the origin of the local reference frame inside the skull. This reference frame is used for measuring motion of brain matter with respect to skull.

- Apply acceleration or velocity time history curves on the head CG.
- Run PAM-CRASH calculation.
- Plot and analyze the calculated results from PAM-CRASH calculation.

Two different loading scenarios were considered where a charge was detonated at a preset standoff (input parameter) in front of dummy and behind the dummy as shown in Figure 6-1.

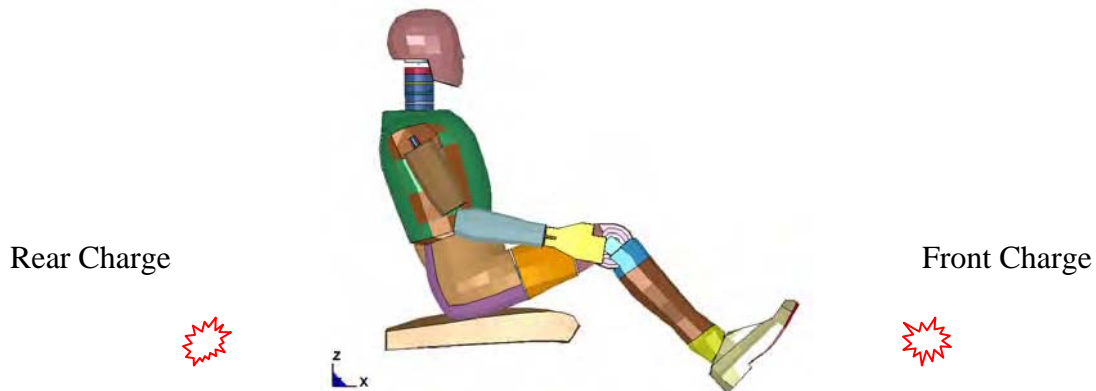


Figure 6-1 Seated dummy model under blast loading

6.2 Simulation Results

6.2.1 Front loading

Typical results for the primary blast injury can be given in the following example. A charge of 20kg TNT was detonated at 2.44m (8 ft) in front of dummy. After explosion, dummy was moved by the blast pressure (Figure 6-2); the head was mainly accelerated in the longitudinal direction with a peak value of 197g at 3ms after detonation (Figure 6-3). In the meantime, head started to rotate until maximum angle was attained; then it rotated in opposite direction due to neck constraint (Figure 6-4).

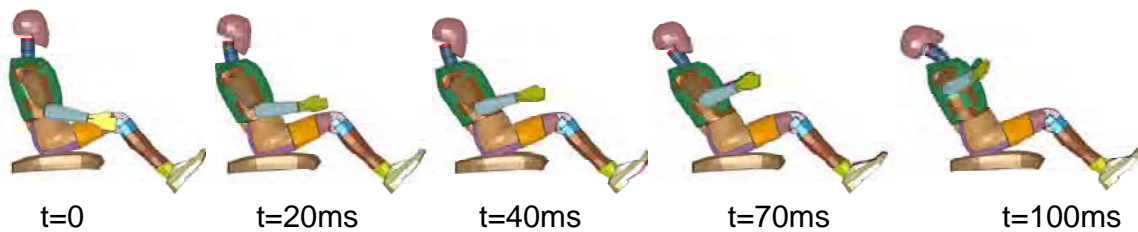


Figure 6-2 Progressive deformation of dummy under blast load from front charge

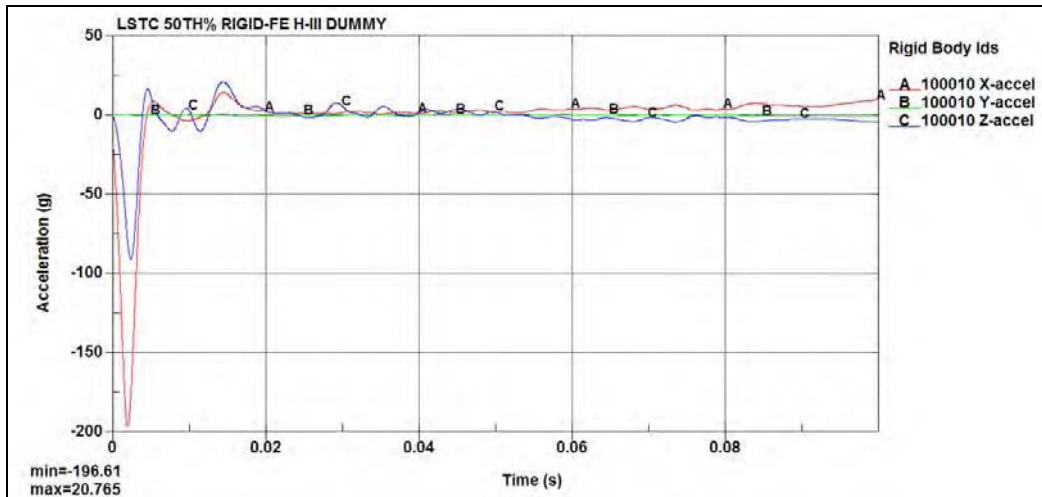


Figure 6-3 Translational acceleration time history of head

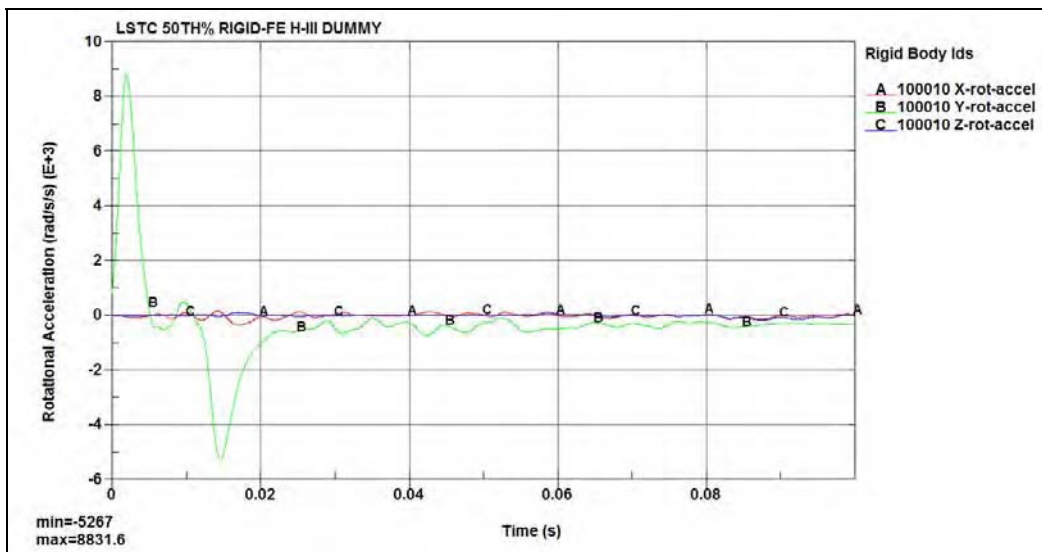


Figure 6-4 Rotational acceleration time history of head

From PAM-CRASH calculations based on the above head kinetic data, fringes of pressure variation with time in Figure 6-5 clearly show the pressure wave traveled over time within brain matter. Intracranial pressure time history plot shows that the relative movement of skull with respect to brain matter can produce very high compressive pressure in the anterior region (Figure 6-5 and Figure 6-6), the peak pressure being above 200 kPa at 3ms. However, the posterior region experienced a tension (negative pressure) first and then a compression (positive pressure), which was caused by the lag of the brain matter (Figure 6-6). This reveals the viscoelastic feature of the material property used for the brain.

The first positive peak pressure in the occipital region was caused by the head rotation around the local y-axis. It then showed pressure variation between negative and positive values when pressure waves traveled through this region.

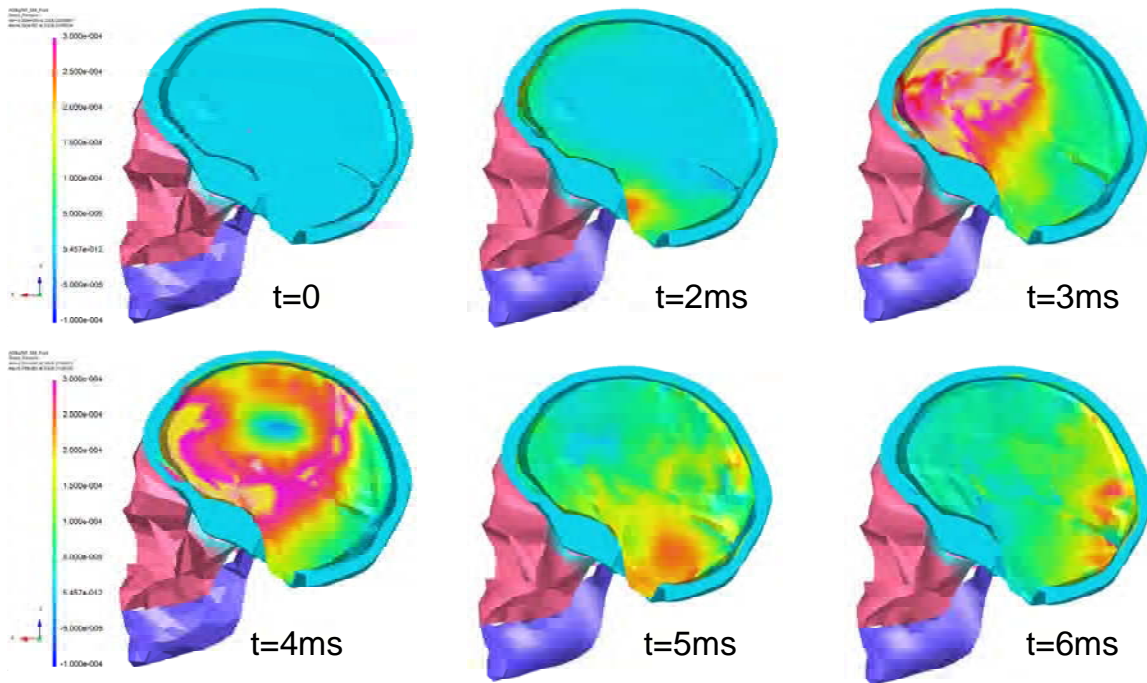


Figure 6-5 Fringes of intracranial pressure variation with time for front blast loading

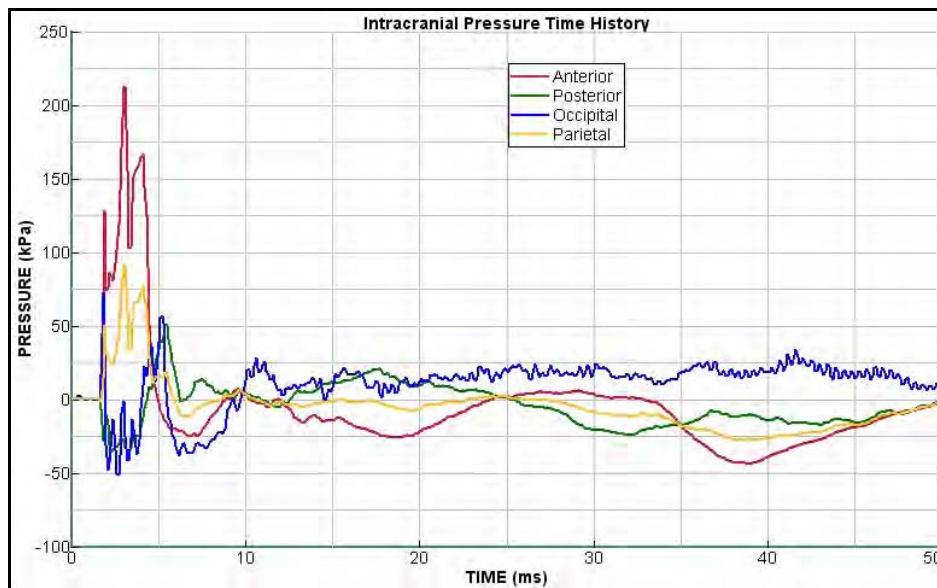


Figure 6-6 Typical intracranial pressure time history for front blast loading

Figure 6-7 displays the CSDM time history which indicates that the CSDM index was increasing to 25% within the first 10 ms as a result of the skull motion under blast pressure near peak acceleration. The second 4% increase of CSDM at 20ms resulted from the direction change of the head rotation axis after 20ms (Figure 6-9). The CSDM value (29.4%) reflects that such a front blast loading can induce moderate diffuse axonal injuries.

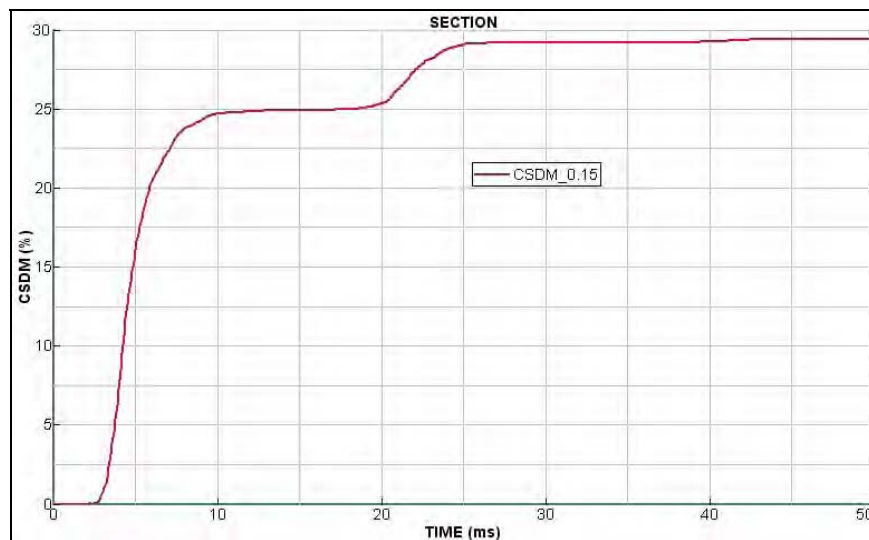


Figure 6-7 CSDM time history for front blast loading

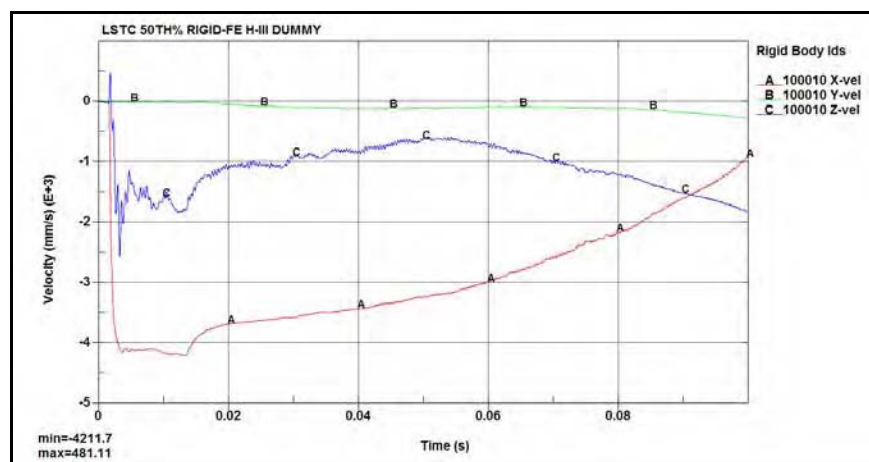


Figure 6-8 Translation velocity time history of head

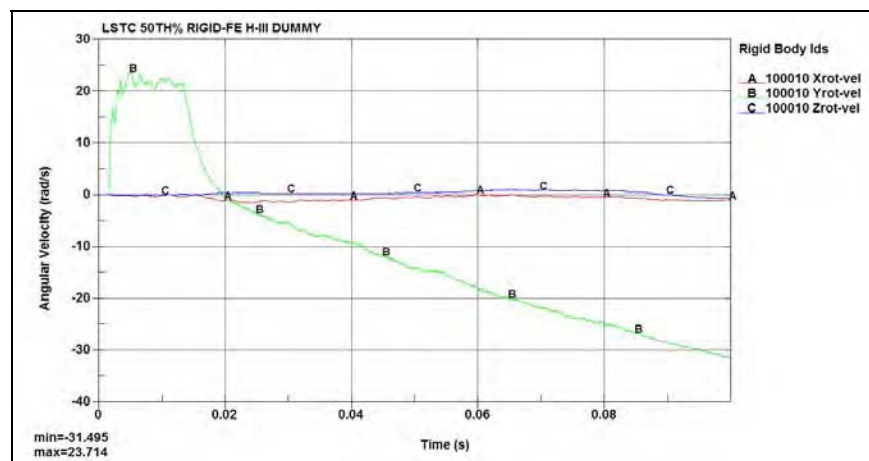


Figure 6-9 Rotational velocity time history of head

6.2.2 Rear Loading

In a rear loading case, 20kg TNT charge was detonated 2.44m (8') rearward of dummy. Figure 6-10 shows the progressive deformations. The dummy head was accelerated in both upward and forward directions with peak accelerations of 104g and 92g respectively (Figure 6-11). The head then started to rotate around the positive y-axis and followed by a whiplash (Figure 6-12).

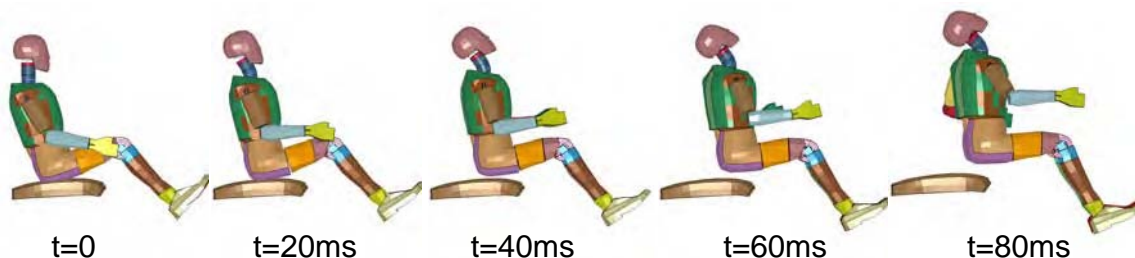


Figure 6-10 Progressive dummy deformation under blast load from rear charge

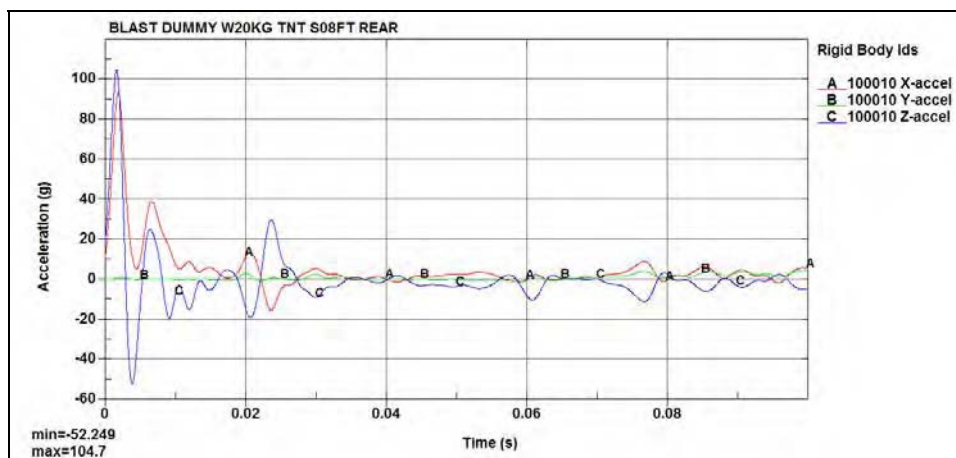


Figure 6-11 Translational acceleration time history of head

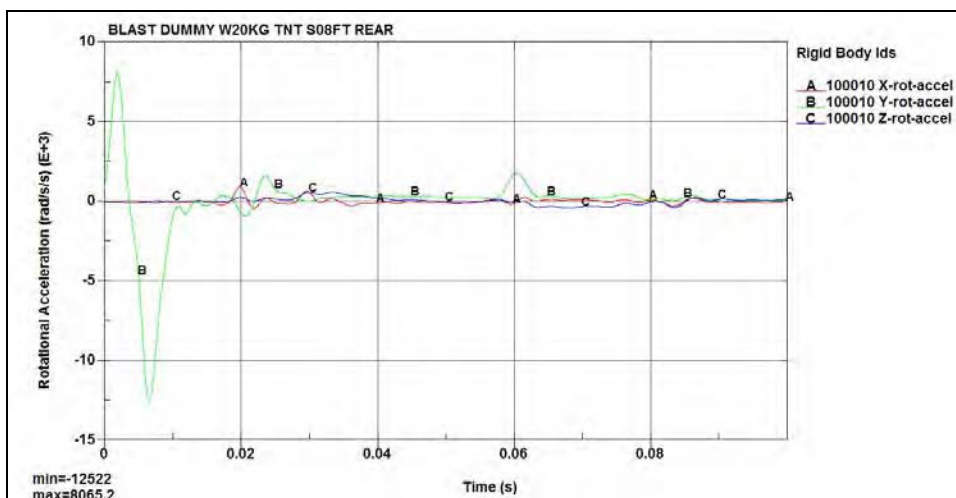


Figure 6-12 Rotational acceleration time history of head

As shown in Figure 6-13, the head kept moving forward and upward. Rotational velocity time history of the head (Figure 6-14) also shows it first rotated around the positive y-axis under blast pressure, then rotated in the opposite direction due to the pulling of neck.

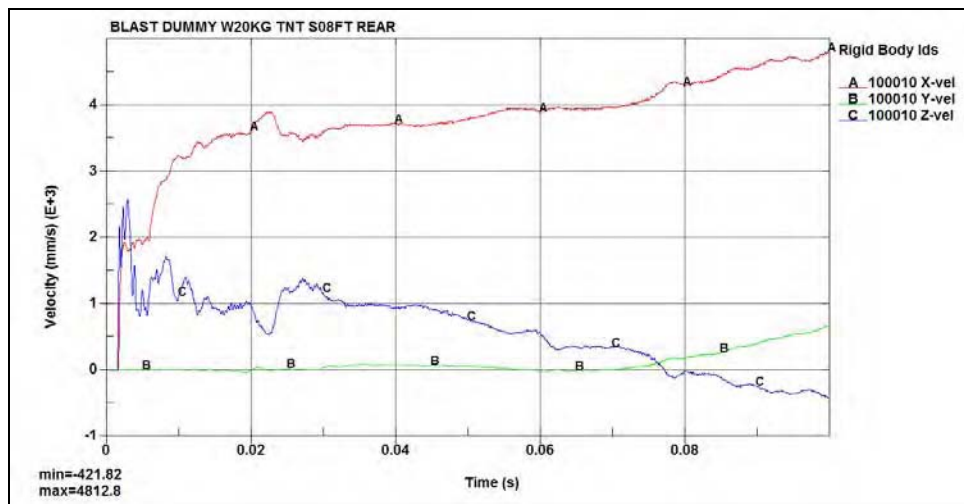
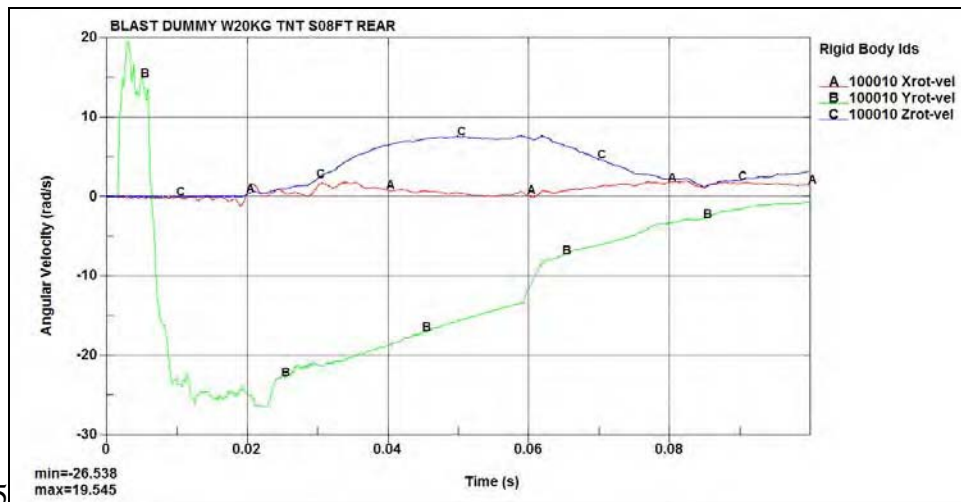


Figure 6-13 Translational velocity time history of head



5

Figure 6-14 Rotational velocity time history of head

Figure 6-15 shows pressure fringe variation with time from the PAM-CRASH calculations, in which pressure wave started at occipital and posterior regions and propagated into parietal and anterior regions. As expected, the intracranial pressure in anterior and parietal regions underwent negative pressure phase first (Figure 6-16) due to the lag of brain matter in the skull. In contrast, the occipital region as well as the posterior region experienced positive pressure first, then negative pressure. As shown in Figure 6-17, the CSDM increased to the first plateau under the direct loading of blast, the head rotation by neck pulling produced the second plateau, with a final value of 21.2%.

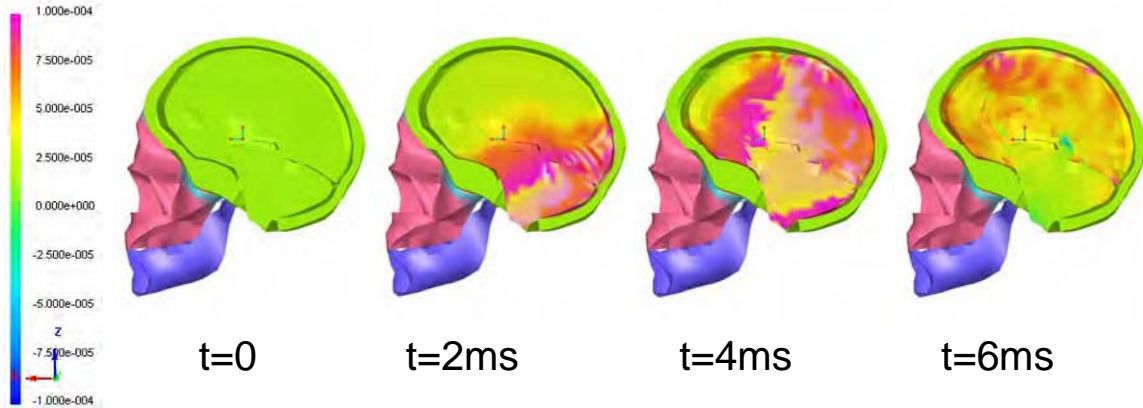


Figure 6-15 Fringes of intracranial pressure variation with time for rear blast loading

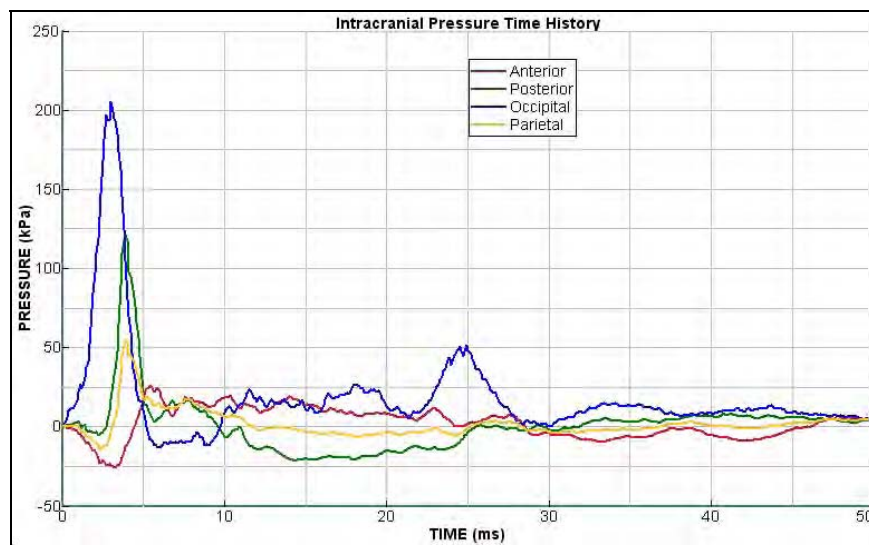


Figure 6-16 Typical intracranial pressure time history for rear blast loading

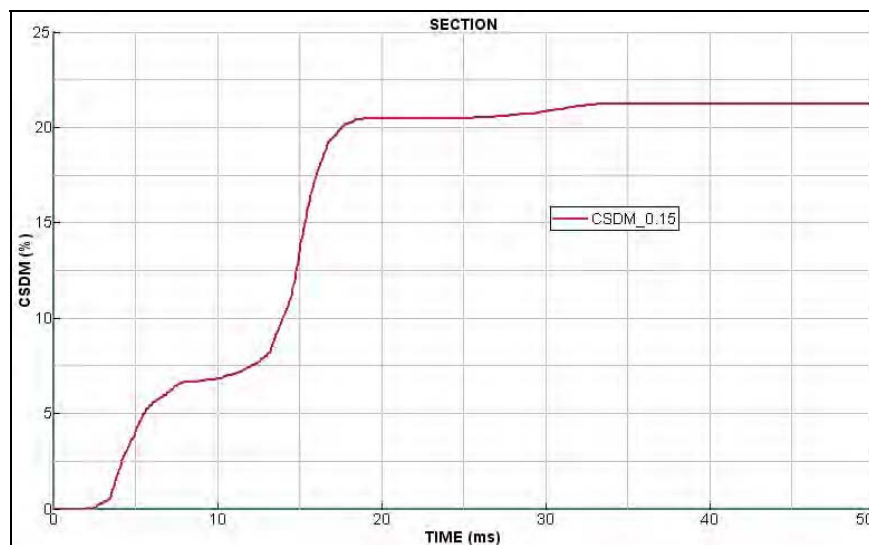


Figure 6-17 CSDM time history for rear blast loading

6.2.3 Primary Blast Injury Parametric Simulation Results

To evaluate brain injury correlation to blast loading impulses, parametric simulations were performed with the charge standoff varying along the x-axis (front-rear). A total of 25 simulations for primary blast injury calculations were performed, of which 12 cases were for front loading conditions and 13 for rear loading conditions (Table 6-1). The CSDM index for each loading case was plotted as a function of blast impulse as shown in Figure 6-18. Values of blast impulse on the dummy were calculated using the momentum obtained by the dummy and the projected area of blast pressure loading.

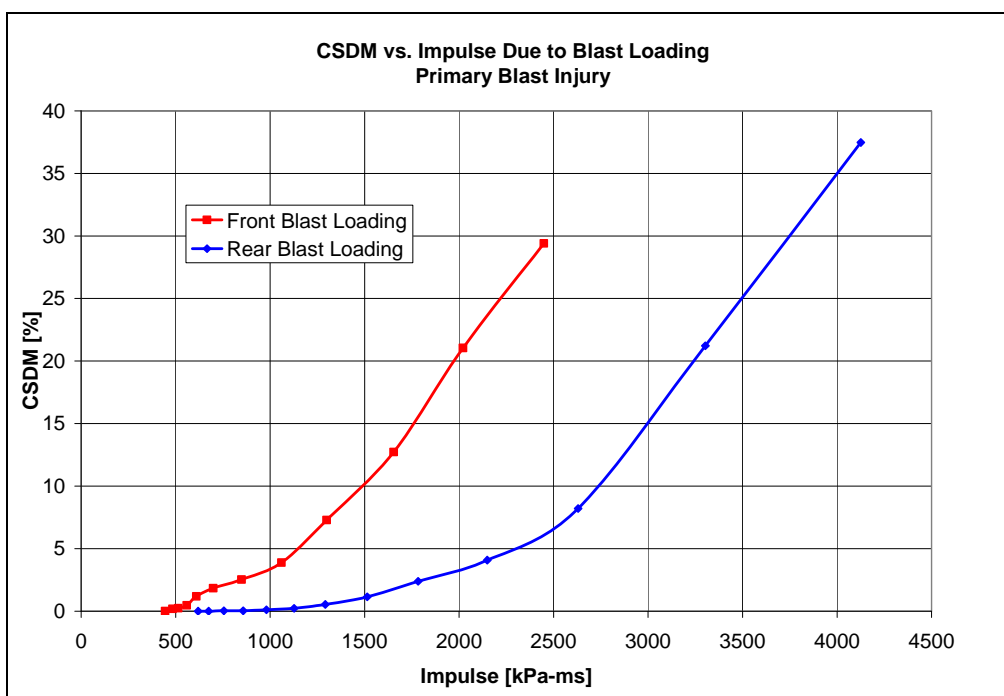


Figure 6-18 CSDM vs. impulse curve for front and rear blast loading

Figure 6-18 demonstrates that for both front and rear loading conditions, the CSDM vs impulse curves exhibit an approximately bilinear relation, with a kink near CSDM = 5.5% for each curve. For the same impulse level, there exists a difference in CSDM between two loading cases, and this difference increases with the impulse, determined by the dummy seating stance in the model. For the front charges, the resultant blast force on the dummy had a downward component which increased the seat resistance to the dummy motion. This would reduce the total momentum transferred to the dummy. As a result, the peak value of head acceleration was slightly larger than that of chest (Figure 6-19). By contrast, for the rear charge cases, the resultant force applied to the dummy had an upward component which tended to reduce the seat resistance. As a result, the peak value of chest acceleration was much larger than that of the head (Figure 6-20).

To see the systematic changes of intracranial pressure under various blast impulses, PAM-CRASH calculation results are plotted for anterior, posterior and occipital regions for both front charge cases (Figure 6-21 to Figure 6-23) and rear charge cases (Figure 6-24 to Figure 6-26).

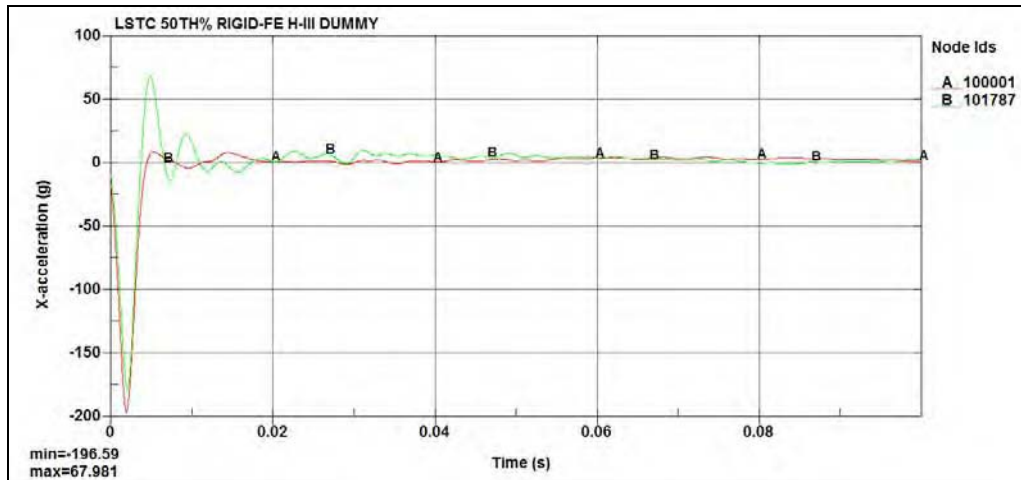


Figure 6-19 X-acceleration histories of head and chest for a front charge case

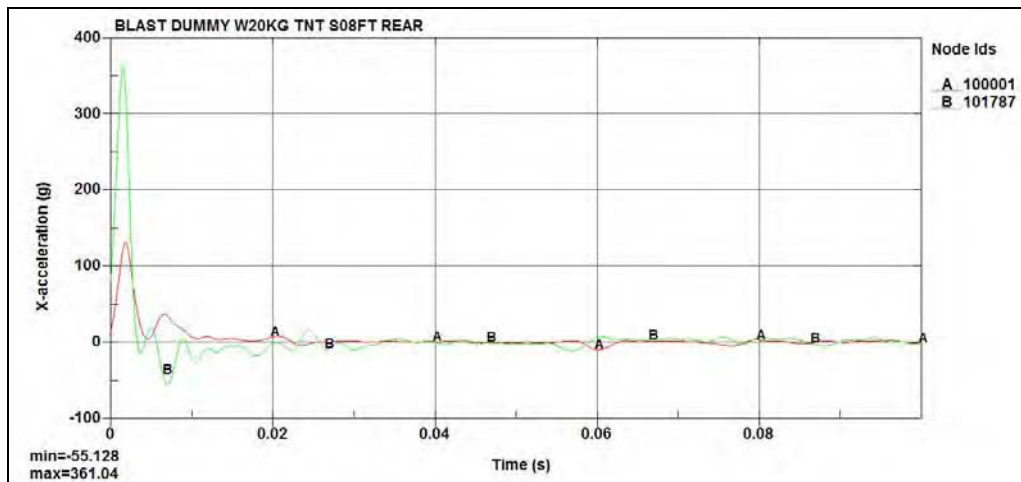


Figure 6-20 X-acceleration histories of head and chest for a rear charge case

Figure 6-21 to Figure 6-23 show a clear trend that for all front charge cases, intracranial pressure in the anterior region will have the maximum peak pressure first, then a negative pressure phase. In the posterior region, it will induce a negative pressure phase first, then a positive pressure phase. Occipital region will have an instantaneous positive pressure, then a negative pressure phase due to motion of cerebellum and brain stem with respect to the skull. Peak pressure values in all regions will reduce with increase in standoff or decrease of impulse.

For rear charge cases, anterior region will experience a negative phase first, then a positive peak (Figure 6-24). Both posterior region and occipital region will have a positive pressure phase and then a low negative pressure phase (Figure 6-25 and Figure 6-26). The maximum peak pressure occurs in the occipital region because of its small volume. Peak pressure dissipates along its traveling path. Detail information for each loading case can be found in the Table 6-1.

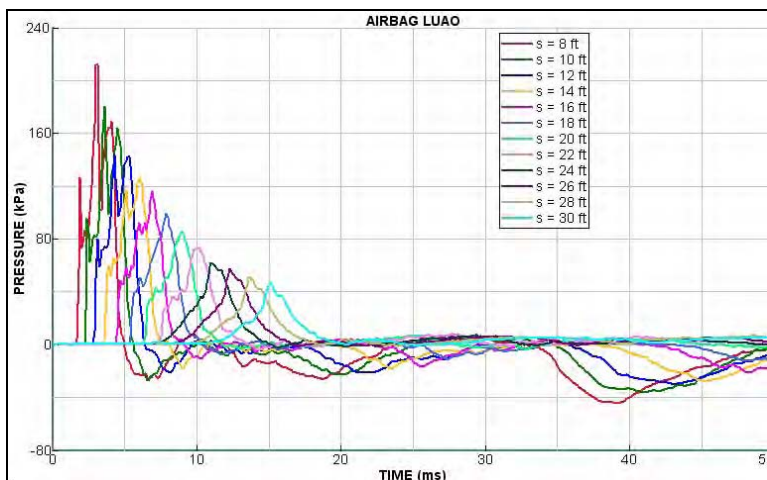


Figure 6-21 Anterior intracranial pressure histories by front blast loading

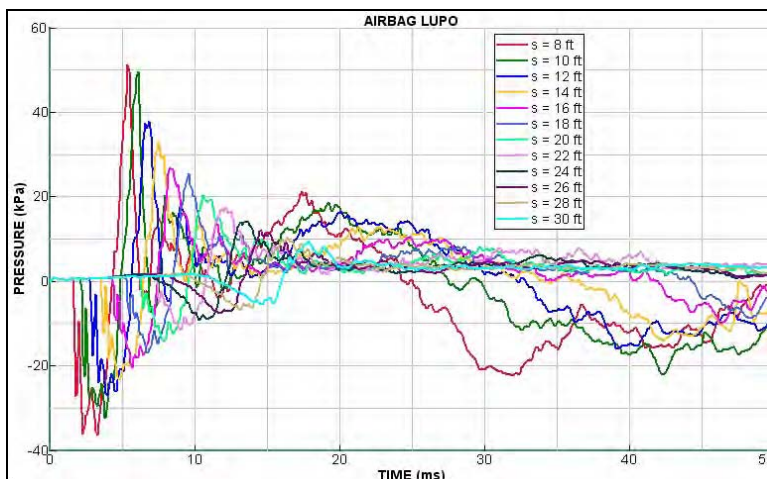


Figure 6-22 Posterior intracranial pressure histories by front blast loading

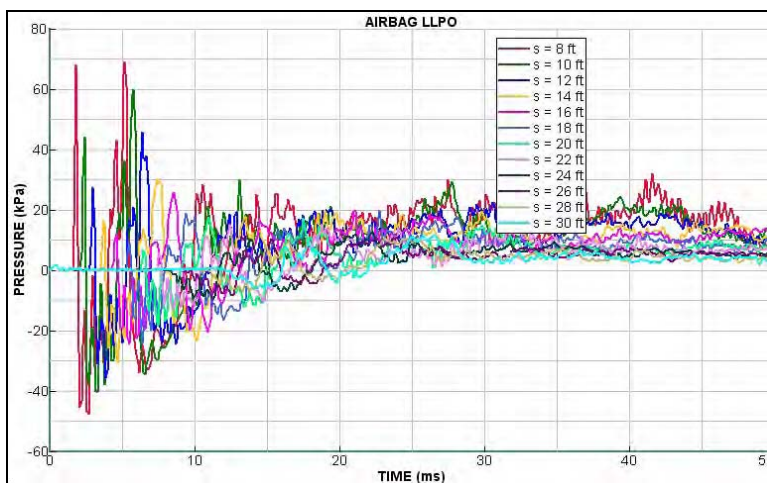


Figure 6-23 Occipital intracranial pressure histories by front blast loading

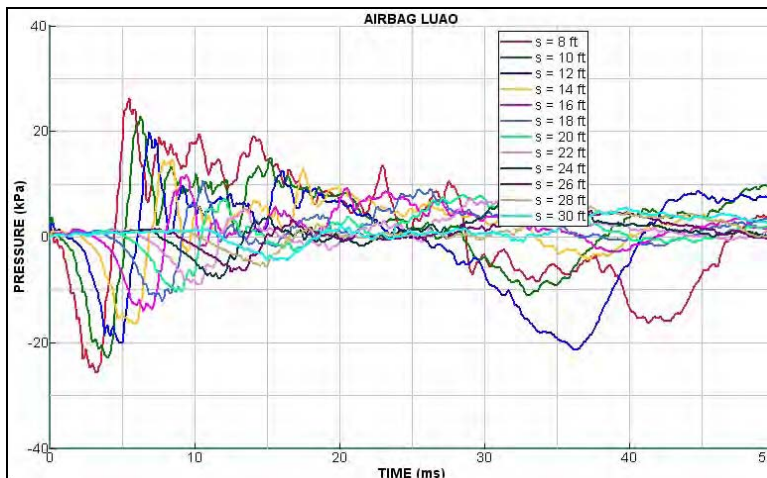


Figure 6-24 Anterior intracranial pressure histories by rear blast loading

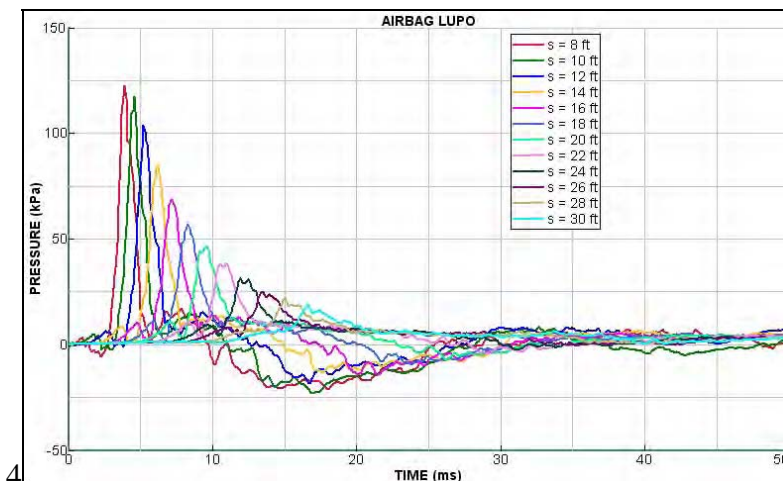


Figure 6-25 Posterior intracranial pressure histories by rear blast loading

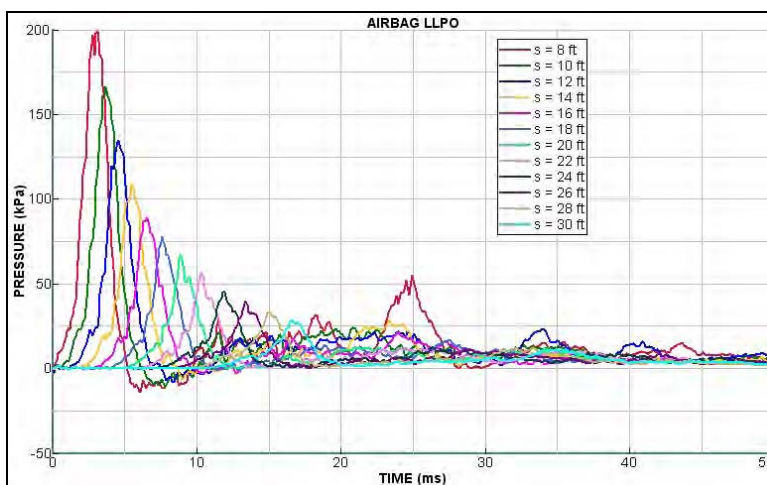


Figure 6-26 Occipital intracranial pressure histories by rear blast loading

Table 6-1 Calculated Cases for Primary Blast Injury Simulation

Standoff [ft]	Blast Loading from Front				Blast Loading from Rear			
	AccX [g]	ΔMV [kg•m/s]	Impulse [kPa]	CSDM [%]	AccX [g]	ΔMV [kg•m/s]	Impulse [kPa]	CSDM [%]
6	-	-	-	-	139.1	1174.1	4125.439	37.477
8	196.60	696.90	2448.70	29.41	104.70	940.12	3303.30	21.22
10	175.90	575.05	2020.56	21.05	83.70	748.35	2629.48	8.20
12	151.90	470.59	1653.51	12.73	72.60	611.63	2149.09	4.08
14	129.60	369.74	1299.16	7.29	61.70	507.56	1783.42	2.39
16	110.60	301.73	1060.19	3.89	52.20	430.84	1513.84	1.15
18	94.60	241.68	849.19	2.53	44.10	367.66	1291.85	0.54
20	81.30	198.98	699.16	1.84	37.60	320.59	1126.46	0.23
22	70.10	173.58	609.91	1.18	32.10	278.94	980.11	0.12
24	60.50	159.06	558.89	0.47	27.30	244.14	857.84	0.03
26	52.90	146.43	514.51	0.24	23.50	214.95	755.27	0.03
28	46.80	137.68	483.77	0.18	20.50	192.07	674.88	0.00
30	41.49	126.54	444.62	0.00	18.13	176.27	619.36	0.00

1. AccX: Peak acceleration in loading direction ($\pm X$)
2. ΔMV : Total momentum obtained by dummy during positive pressure duration
3. Impulse: Values are converted from dummy's momentum
4. CSDM: Values are taken at calculation termination time

6.3 Remarks

1. Primary blast loading can potentially cause mild diffuse axonal injury.
2. For same level of blast-charge weight and standoff, brain injury can be worse if head motion is restricted by the neck. On the other hand, brain injury can be reduced if the head is pulled by the neck to follow the motion of upper body.
3. The CSDM vs impulse curves are bilinear relations, with a kink near CSDM = 5.5% for each curve.
4. For the front charge cases, simulation results indicate the impulse level of 1300 kPa-ms and 2000 kPa-ms are the thresholds for mild DAI (CSDM >5.5%) and moderate DAI (CSDM >22.5%).
5. For the rear charge cases, simulation results indicate the impulse level of 2400 kPa-ms and 3300 kPa-ms are the thresholds for mild and moderate DAI.

7. Parametric Simulations of Secondary Blast Injury

A secondary blast injury is caused by flying objects striking individuals. In other words, a secondary-blast-induced TBI simulation involves individuals getting impacts from fragments or flying debris. Extremely high-speed-munitions-fragment impact and penetration phenomena were not analyzed here, since they usually cause directly vital brain damage. This section will focus on TBI caused by blunt-shaped fragments flying at medium velocity.

A parametric study was performed to identify the effect of fragment impulse on the extent of damage to the brain, using CSDM as the injury metric.

7.1 Simulation Procedure of Secondary Blast-Induced TBI

To analyze the process of fragments impacting the human head, H-Head modeling alone is not enough. The model must be attached to a human body model in order to avoid over-predicted head rotation after fragment impact. Besides the H-Head FE model, currently the PAM-CRASH human body model was not available for this project. Therefore, the simulations were performed in two stages, as in the previous section. In the first stage, the calculations were carried out using LS-DYNA with the aid of Hybrid-III dummy model to obtain the kinetic data of head CG. The dummy was kept seated (as provided by LS-DYNA) but without support. Fragment was pre-assigned with a preset speed to impact on the head surface (Figure 8-1). After LS-DYNA calculations, the head kinetic data including acceleration, velocity, and momentum were extracted. These data were then used in the second stage, the PAM-CRASH calculations. The second stage takes advantages of geometry and material properties of H-Head model. Deformation and intracranial pressure of brain can then be obtained from the second-stage calculations. As a summary, the simulation procedure is given as follows

1. LS-DYNA calculations:
 - Define contact surface between flying fragment and H-III dummy head.
 - Position the fragment and assign the initial velocity.
 - Perform LS-DYNA simulation.
 - Analyze calculated results and output the translational and rotational acceleration and velocity time history data in all x, y and z-directions.
 - Convert the time history data into PAM-CRASH curve format for the next step.
2. PAM-CRASH calculations:
 - Define the outer and inner table, dipole, facial bone, and mandible parts in H-Head model as a rigid body, the skull.
 - Set the CG of head as the origin of the local reference frame inside the skull. This reference frame is used for relative motion measuring.
 - Apply acceleration or velocity time history curves on the head CG.
 - Perform PAM-CRASH simulation.
 - Plot and analyze the calculated results from PAM-CRASH calculation

Two different loading scenarios were considered here, the flying fragment impacts on the front of the dummy head and at the rear of dummy head (Figure 7-1). For all cases, the fragment was defined as a 20mm-thick circular steel plate of 50mm diameter. Front impact event has a downward impact angle of 37.7 degrees. For rear impact, the fragment impacts the head horizontally. To isolate the brain damage purely contributed by fragment impact, no blast pressure was applied on the dummy or H-head models in all simulations.

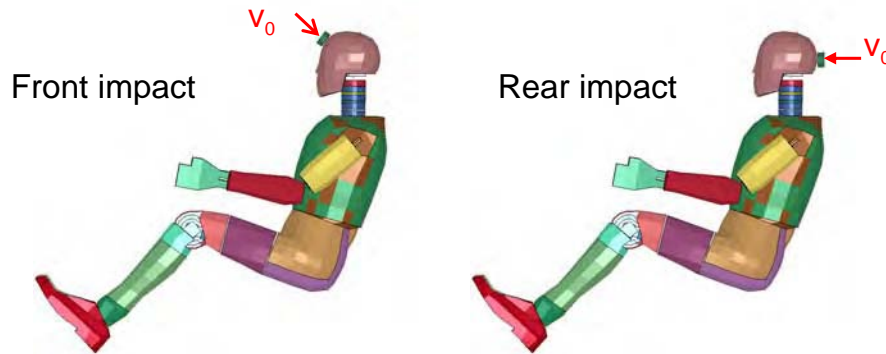


Figure 7-1 FE models for front impact (left) and rear impact (right) by fragment

7.2 Simulation Results

7.2.1 Front Impact

Typical results from a front impact event are as follows. In this case, the circular plate fragment impacted on anterior area of head at 20 m/s. After impact, the dummy was moved by momentum (Figure 7-2); the head quickly attained its peak value of 120g (Figure 7-3). The head then started to rotate with neck bending, which was followed by upper-body rotation when neck bending stopped (Figure 7-4). The backward and rotating motions of the head continued at least 100ms, as reflected in the translational and rotational velocity time histories plots (Figure 7-5 and Figure 7-6).

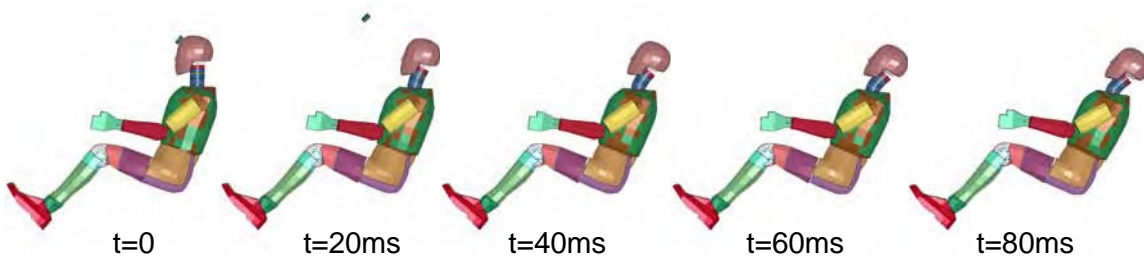


Figure 7-2 Progressive deformation of dummy by a front blow from a fragment at 20 m/s

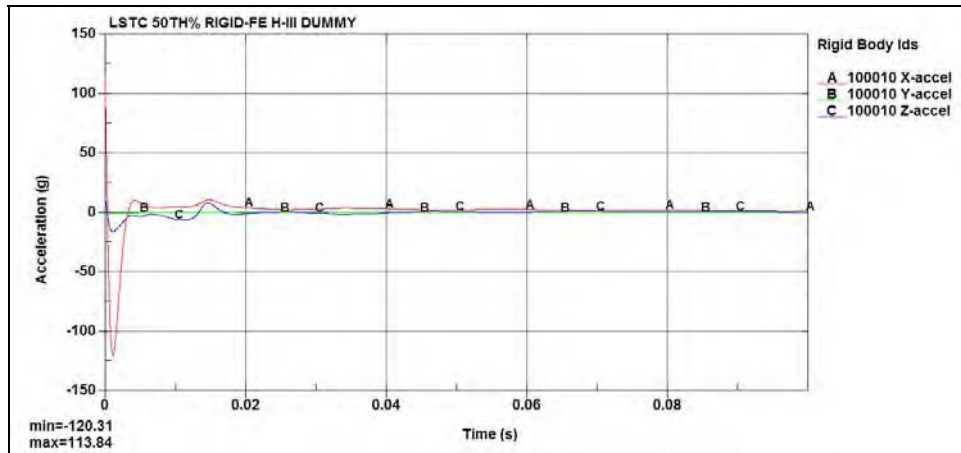


Figure 7-3 Translational acceleration time history of head

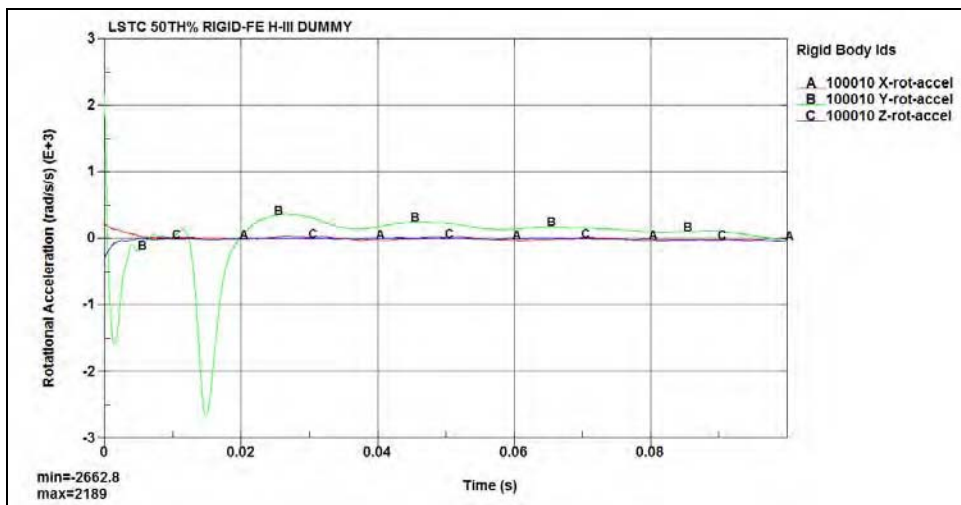


Figure 7-4 Rotational acceleration time history of head

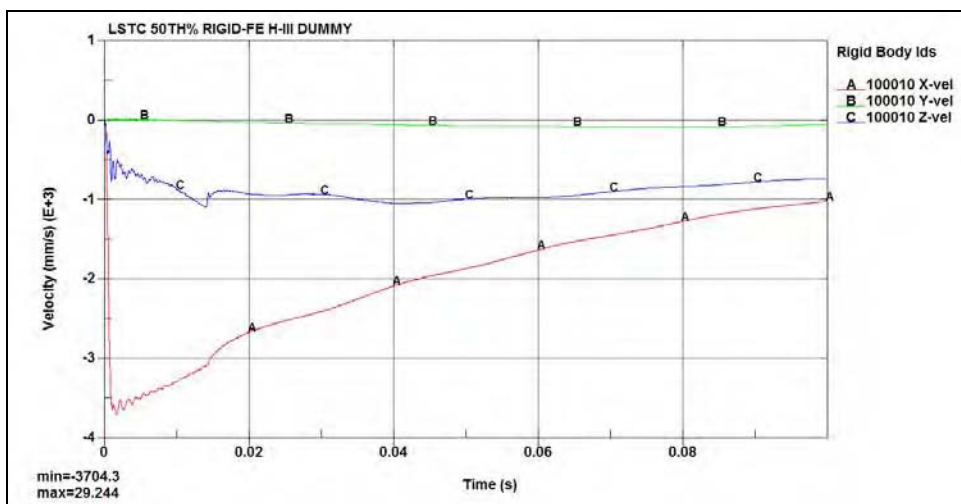


Figure 7-5 Translational velocity time history of head

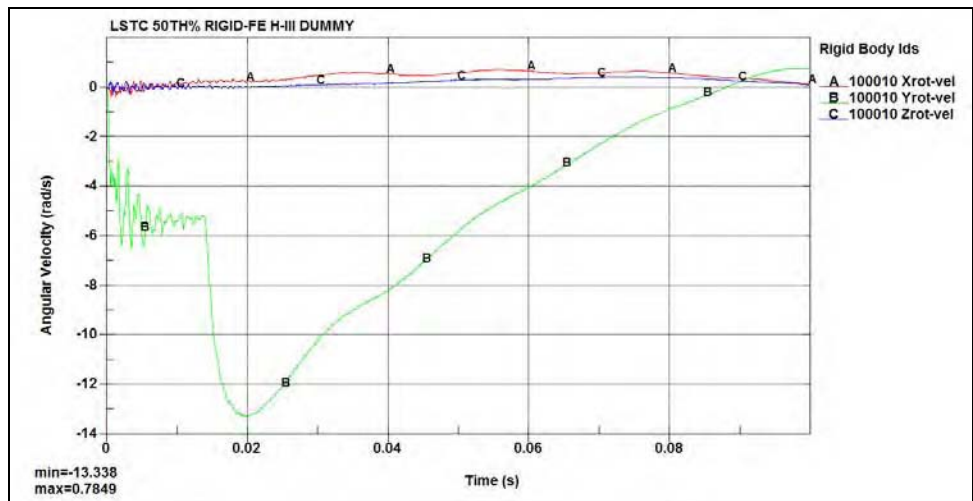


Figure 7-6 Rotational velocity time history of head

Corresponding results from PAM-CRASH calculation show the front impact generated a compressive pressure wave in the anterior and parietal regions, which dissipated quickly with time (Figure 7-7). Intracranial pressure time histories were recorded in Figure 7-8.

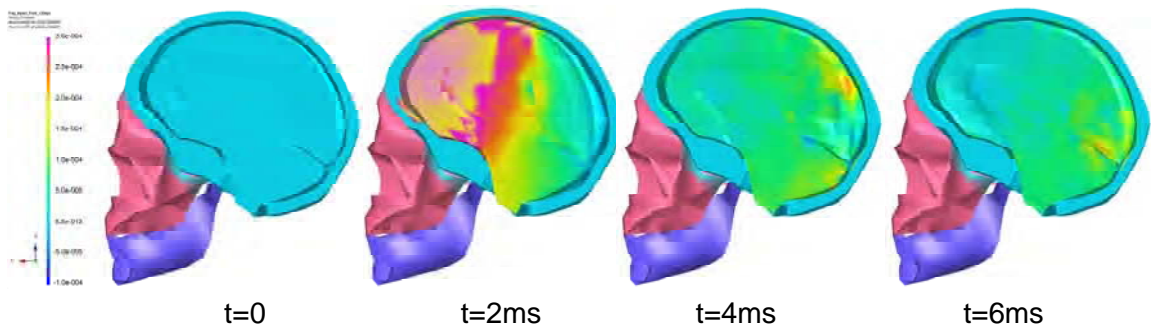


Figure 7-7 Fringes of intracranial pressure variation with time for a front impact

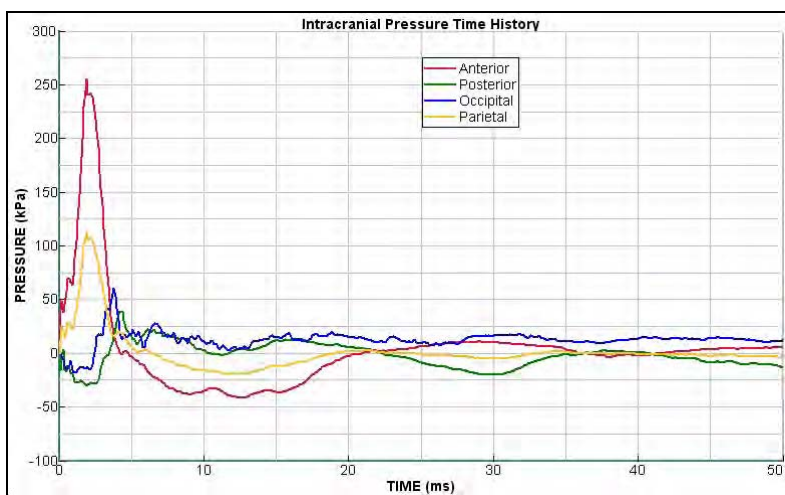


Figure 7-8 Typical intracranial pressure time history for a front impact event

The compressive pressure in the anterior region had a peak value of 250 kPa, and the peak value in the parietal region decreased to 110 kPa. In both regions, it was followed by a negative pressure phase. In contrast, the posterior and occipital regions experienced a tension (negative pressure) first and then a compression (positive pressure), which was caused by the lagged motion of brain matter, as expected. As shown in Figure 7-9, the CSDM index increased to 6.6% within the first 8ms of the front impact event.

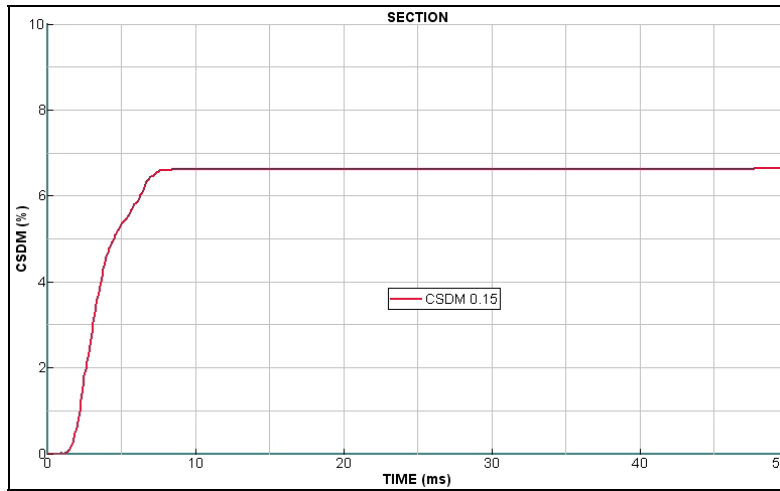


Figure 7-9 CSDM time history for a front impact event

7.2.2 Rear Impact

For a typical rear impact event simulation, the initial velocity of fragment was set as 20 m/s in the horizontal direction. Figure 7-10 shows the fringes of progressive deformations of dummy by such a blow. The peak translational acceleration of the head was 147g in positive x-direction (Figure 7-11). With the impact, the head was subjected to a positive rotational acceleration about the y-axis, and the rotation would cause further neck bending (Figure 7-12). The forward and rotating motion of the head were kept at least 100ms, which can be seen in the translational and rotational velocity time history plots (Figure 7-13 and Figure 7-14).

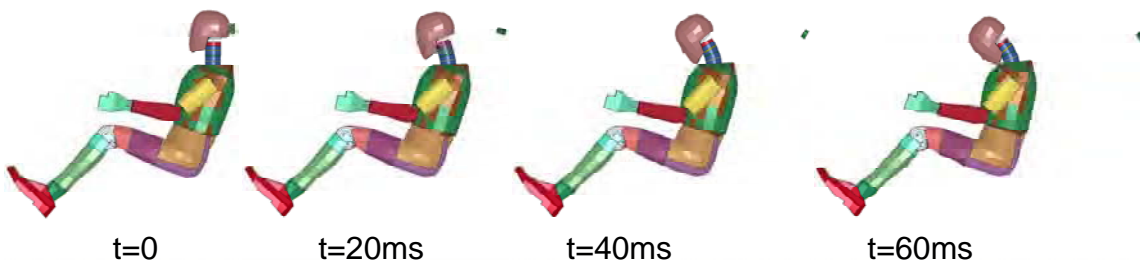


Figure 7-10 Progressive deformation of dummy by a rear blow from a fragment at 20 m/s

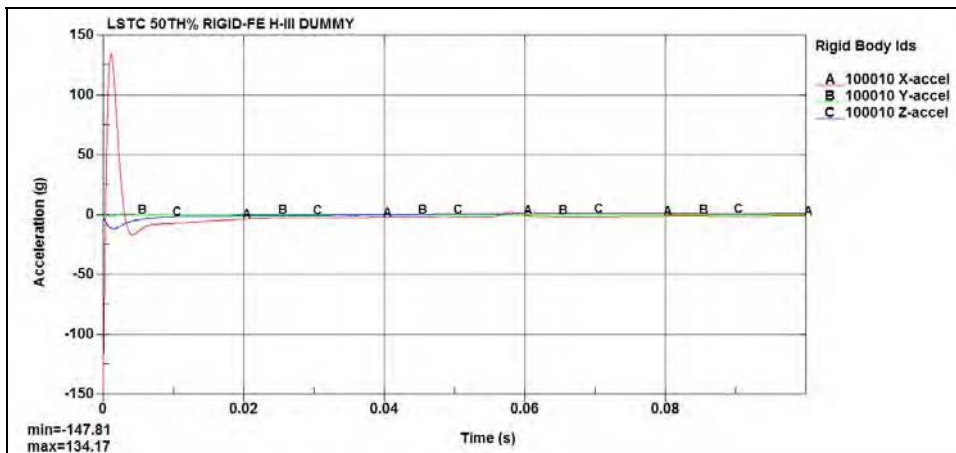


Figure 7-11 Translational acceleration-time history of head

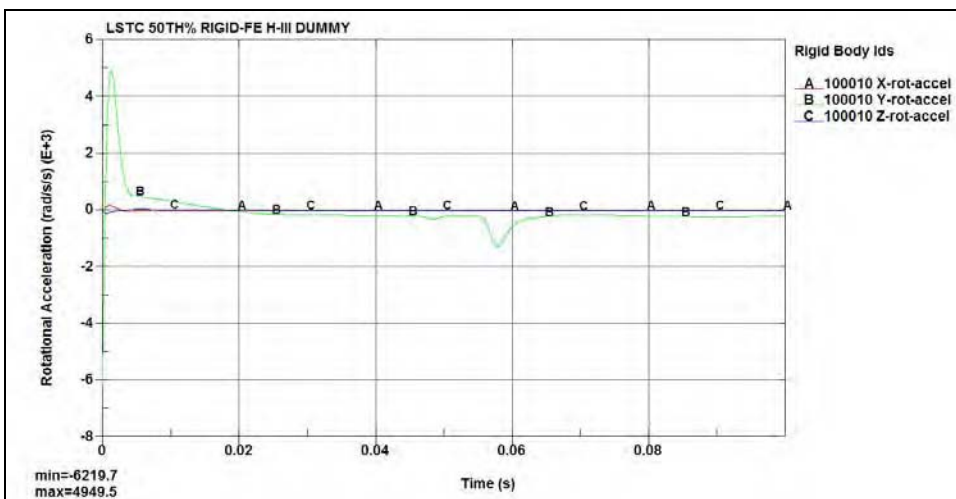


Figure 7-12 Rotational acceleration-time history of head

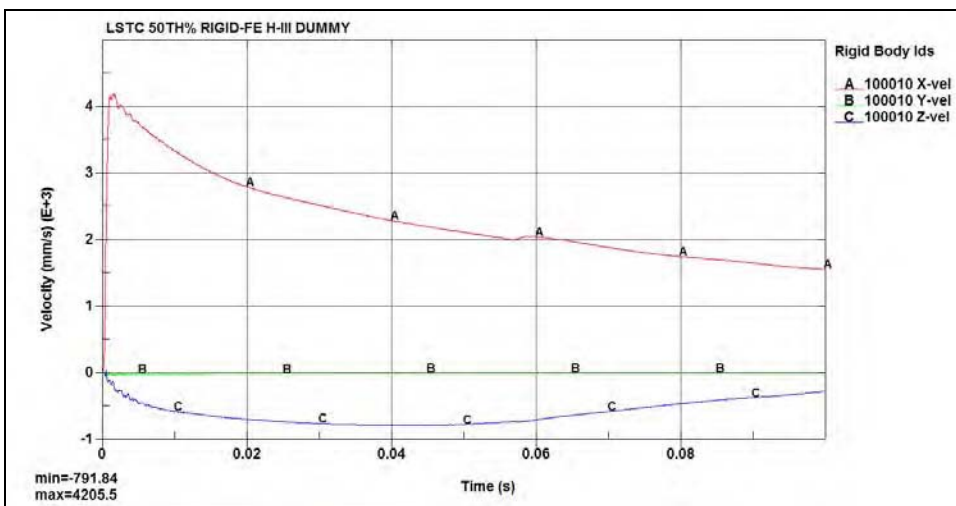


Figure 7-13 Translational velocity-time history of head

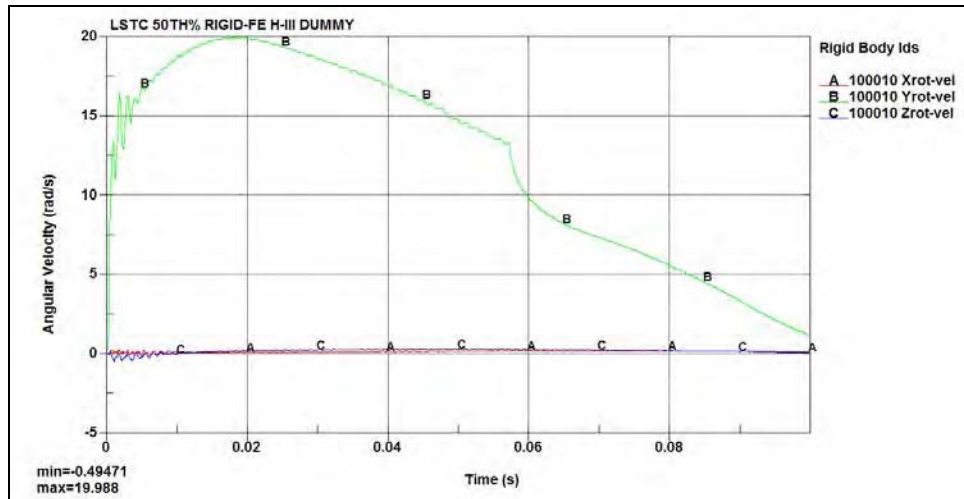


Figure 7-14 Rotational velocity-time history of head

Results of PAM-CRASH calculation show the rear fragment impact generated a compressive pressure wave in the posterior and occipital regions and that it propagated to parietal and anterior regions (Figure 7-15). Corresponding intracranial pressure time histories for each region are plotted in Figure 7-16.

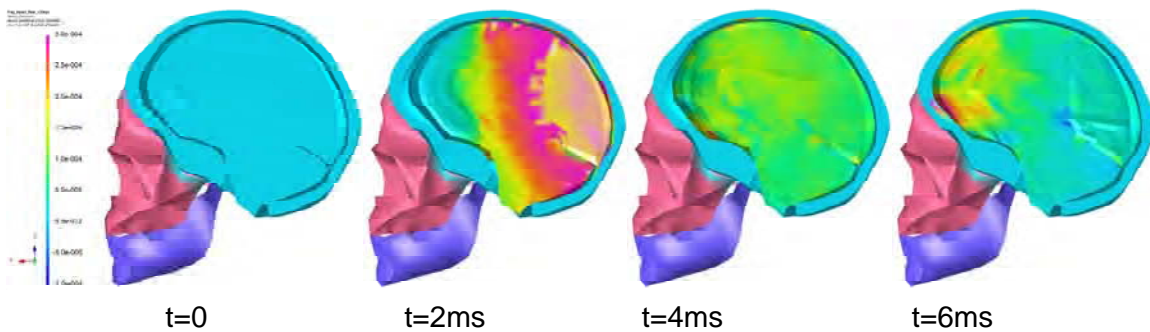


Figure 7-15 Fringes of intracranial pressure variation with time for a rear impact

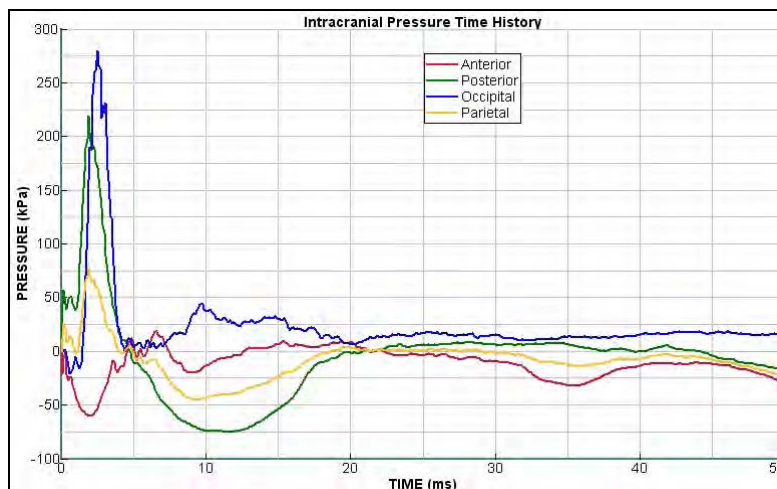


Figure 7-16 Typical intracranial pressure time history for a rear impact event

As expected, the intracranial pressure in the anterior region underwent negative pressure first. By contrast, the posterior region experienced compression first, then tension, because of the relative motion between brain matter and skull. Maximum peak pressure was found about 275 kPa in the occipital region. CSDM climbed to the peak value of 16.4% in the first 10ms (Figure 7-17). This is the time when brain matter had undergone all the positive and negative peak pressures.

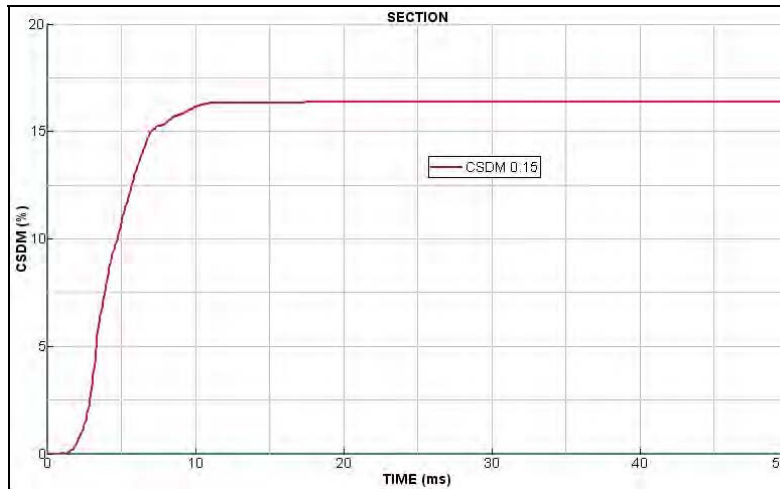


Figure 7-17 CSDM time history for a typical rear impact event

7.2.3 Secondary Blast Injury Parametric Simulation Results

To evaluate brain injury correlation to fragment impact with different momentums / impulses a total of 22 simulation cases with the impact speed varying from 8 m/s to 30 m/s were performed with 12 cases for front impact and 10 for rear.

Figure 7-18 to Figure 7-20 demonstrate a clear trend of intracranial pressure for front fragment impact events. The pressure history of the anterior region shows it undergoes a positive phase immediately after the impact, then enters a negative pressure phase because of the lag of brain matter. The peak pressure ranges from 100 kPa to 350 kPa for initial impact speeds from 8 m/s to 30 m/s. For the negative pressure phase, the peak pressures are less than 100 kPa. Posterior and occipital regions have the opposite trend, a negative pressure phase followed by a positive one.

For the rear fragment impact events, the anterior region will experience a negative pressure phase, then a positive phase (Figure 7-21). The posterior region will enter a positive phase immediately after impact; it will then pass peak pressure and enter a negative phase (Figure 7-22). Peak pressure in occipital region ranges from 120 kPa to 360 kPa for impact speeds from 8 m/s to 30 m/s. For the same event, peak pressure in the occipital region was higher than in the posterior region. This was caused by the small volume of the cerebellum and brain stem. Pressure wave traveling into the cerebellum and stem domain would converge and reflect backward quickly.

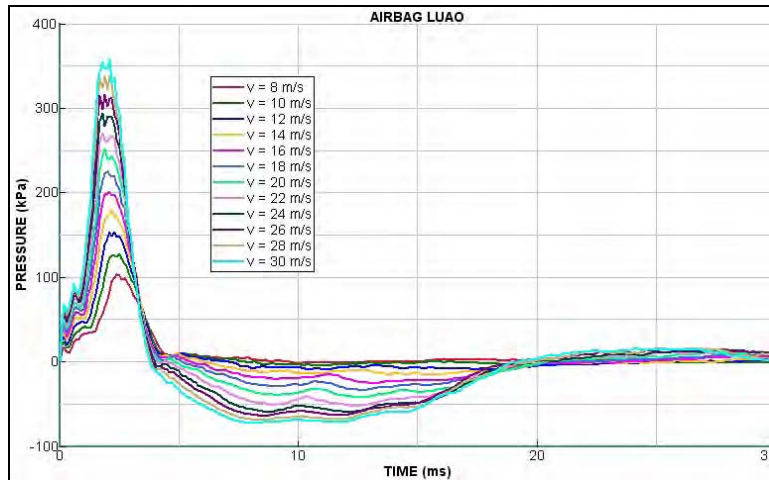


Figure 7-18 Anterior intracranial pressure histories for front impact at various speeds

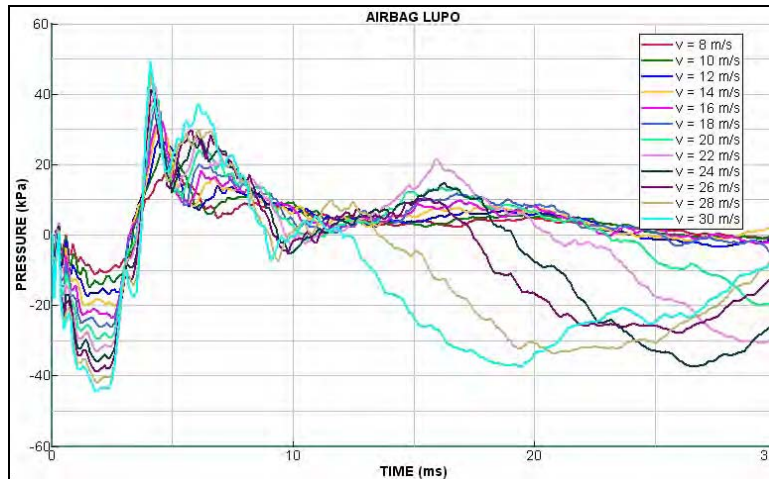


Figure 7-19 Posterior intracranial pressure histories for front impact at various speeds

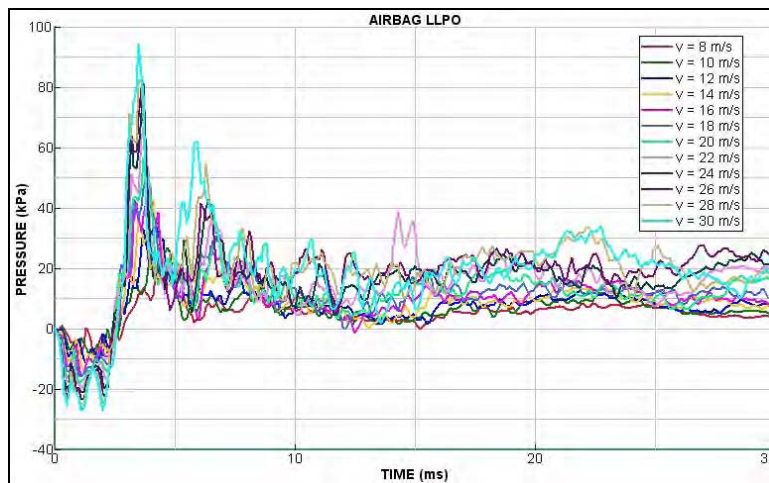


Figure 7-20 Occipital intracranial pressure histories for front impact at various speeds

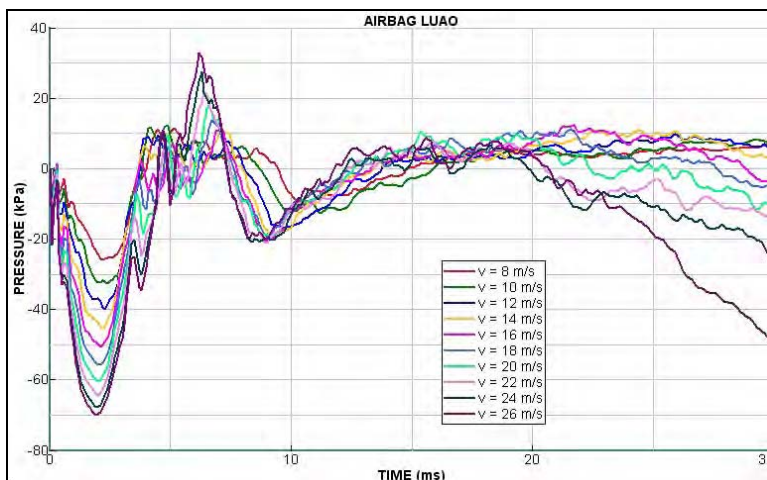


Figure 7-21 Anterior intracranial pressure histories for rear impact at various speeds

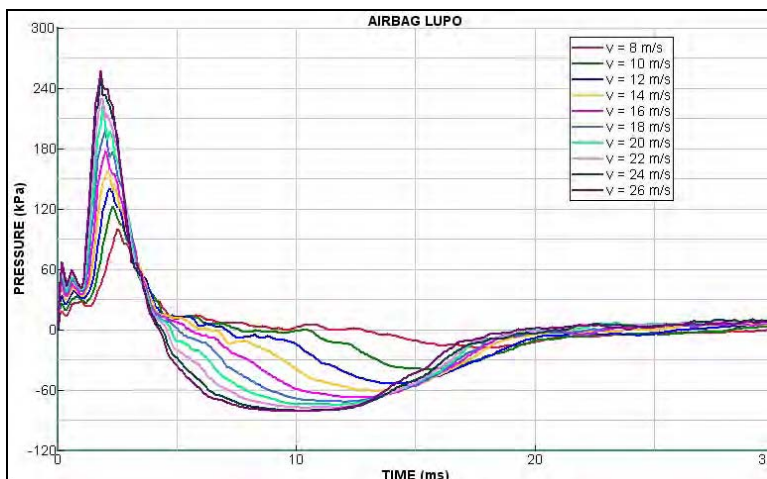


Figure 7-22 Posterior intracranial pressure histories for rear impact at various speeds

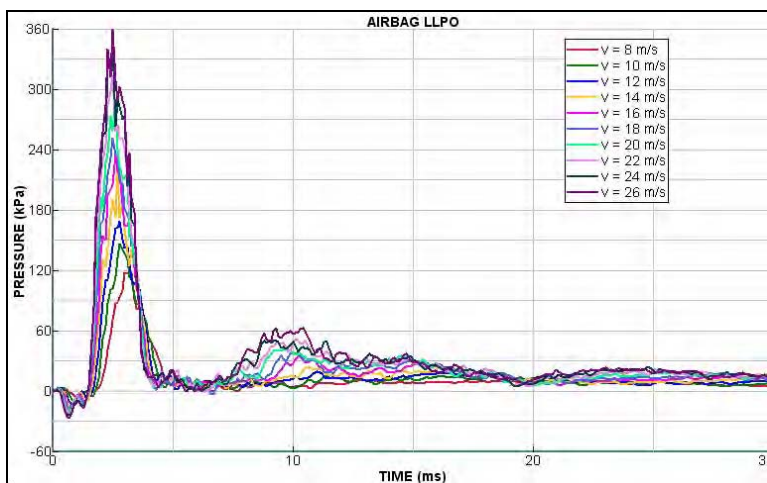


Figure 7-23 Occipital intracranial pressure histories for rear impact at various speeds

CSDM for each impact case was plotted as a function of impact impulse in Figure 7-24. These impulse values were derived from the amount of momentum transferred from fragment to dummy. The summary for all cases is given in Table 7-1. It was found that the upper-body rotation would dominate when the impact speed was too high; this was revealed by the growing rate of the peak head acceleration in the x-axis direction slowed down after the impact speed was over 22 m/s (Table 7-1).

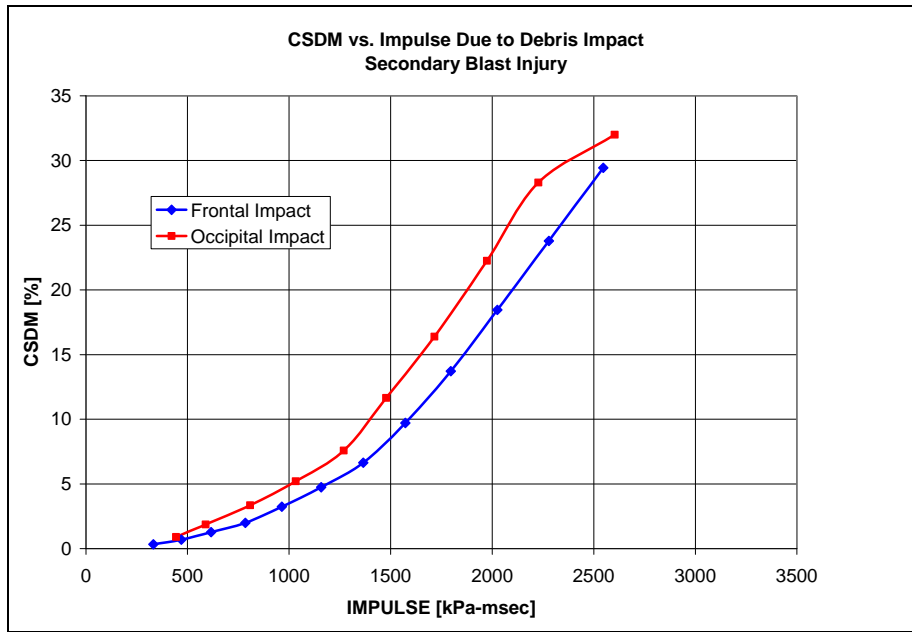


Figure 7-24 CSDM vs impulse curve for front and rear fragment impact

Table 7-1 Calculated Cases for Secondary Blast Injury Simulation

Speed [m/s]	Front Fragment Impact				Rear Fragment Impact			
	AccX [g]	ΔMV [kg•m/s]	Impulse [kPa]	CSDM [%]	AccX [g]	ΔMV [kg•m/s]	Impulse [kPa]	CSDM [%]
8	73.31	0.65	332.42	0.33	87.30	0.87	443.65	0.90
10	86.68	0.92	470.08	0.69	103.69	1.16	589.00	1.87
12	97.98	1.21	616.25	1.28	114.37	1.59	808.05	3.36
14	105.06	1.54	785.03	1.99	122.04	2.03	1032.95	5.20
16	112.21	1.89	964.25	3.25	123.17	2.49	1269.72	7.58
18	116.42	2.27	1157.58	4.75	129.63	2.90	1477.97	11.65
20	120.31	2.68	1365.16	6.64	134.17	3.37	1715.71	16.38
22	123.71	3.09	1572.50	9.72	135.96	3.88	1973.92	22.25
24	123.87	3.53	1796.23	13.72	138.73	4.37	2227.35	28.30

26	127.81	3.98	2026.02	18.46	134.86	5.11	2603.36	31.99
28	130.34	4.47	2278.94	23.78	134.02	5.72	2914.74	–
30	131.02	5.00	2546.78	29.43	132.33	6.16	3135.93	–

1. *AccX: Peak acceleration in primary impact direction ($\pm X$);*
2. *ΔMV : Momentum transferred from fragment to dummy during impact*
3. *Impulse: Values are converted from momentum*
4. *CSDM: Values are taken at calculation termination time.*
5. *Mass of fragment for all cases: 0.303kg.*

7.3 Remarks

1. Secondary blast brain injury can cause either mild or moderate diffuse axonal injury.
2. For the same level of impulse, posterior impact can cause more brain tissue damage than anterior impact.
3. Based on simulation results, the impulse at the level of 1000 kPa-ms and 2000 kPa-ms are the thresholds for mild DAI (CSDM >5.5%) and moderate DAI (CSDM >22.5%).
4. The CSDM vs impulse curves are roughly bilinear relations, with a kink near CSDM = 5.5% for each curve. The bilinear relations may imply that the increase of brain damage vs increase of impulse enters a higher level after the impact impulse passes the threshold for mild DAI.

8. Parametric Simulation of Tertiary Blast Injury

A tertiary blast injury occurs when people are forcefully put in motion by the blast and strike other objects. In this section, a parametric study was performed to identify the effect of blast impulse on the extent of damage to the brain, using CSDM as the injury metric, as a direct result of a person being put into motion by the blast wave and subsequently impacting surrounding objects by kinetic inertia. Furthermore, focus will only be on head impacts.

8.1 Simulation Procedure of Tertiary Blast-Induced TBI

Similarly, simulations were performed in two stages. In the first, the calculations were carried out using LS-DYNA and a Hybrid-III dummy model with the primary objective of obtaining the kinetic data of head CG. The dummy was kept seated (as provided by LS-DYNA) but without a seat support. Blast charge was located in front of or behind the dummy at some distance. A rigid plate was fixed in space before or after the head for impact events. Head kinetic data such as acceleration, velocity, and momentum were extracted for input into the second stage involving the PAM-CRASH calculations. The second stage takes advantages of the geometry and material properties of the H-Head model. Deformation and intracranial pressure of brain can then be obtained by the end of the second stage calculation. The simulation procedure is summarized as follows:

1. LS-DYNA calculation:
 - Define loading segments on dummy for blast loading.
 - Define contact surface between H-III dummy head and impact object.
 - Define parameters for *load_blast* function for blast explosion.
 - Perform LS-DYNA simulation.
 - Analyze calculated results and output translational and rotational acceleration, velocity-time history data in all x, y and z directions.
 - Convert time-history data into PAM-CRASH curve format for the next step.
2. PAM-CRASH calculation:
 - Define the outer and inner table, dipole, facial bone, and mandible parts in H-Head model as a rigid body – the skull.
 - Set the CG of head as the origin of the local reference frame inside the skull. This reference frame is used for measuring relative motion of brain matter to skull.
 - Apply acceleration or velocity time-history curves on the head CG.
 - Perform PAM-CRASH simulation.
 - Plot and analyze the calculated results from PAM-CRASH calculation.

Two loading scenarios were considered (Figure 8-1). The first involves a blast charge located a distance in front of the dummy so that the head would impact a rear rigid plate. The second involves a blast located a distance from the back of the dummy so that the head

would impact a rigid plate in front of the dummy. For both scenarios, a gap between head and rigid plate was assigned in order to ensure that the dummy completely experienced the momentum from the blast impulse before impact.

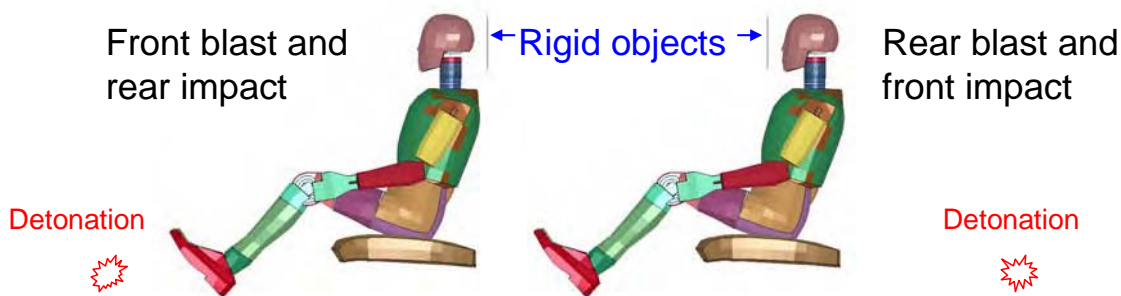


Figure 8-1 FE model set up for tertiary-blast-injury simulation

8.2 Simulation Results

8.2.1 Front Blast Loading with Rear Impact Event

In this case, a charge of 20 kg TNT was detonated 4.27m in front of the dummy. After detonation, the dummy was moved by the blast pressure (Figure 8-2); the head acceleration attained its peak value of 129.6g about 5 ms after detonation (Figure 8-3). The head then started to rotate under pressure. Head and upper body moved backward and impacted the rigid plate at 23ms (Figure 8-5 and Figure 8-6). The impact accelerated the head in the opposite direction with a peak value of 189g; it also caused a second head rotation (Figure 8-4 and Figure 8-7).

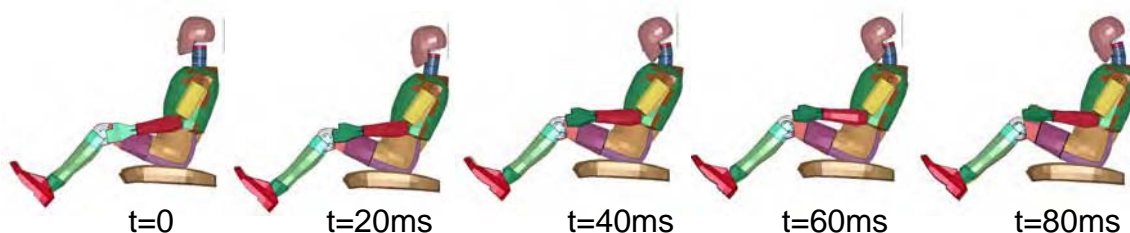


Figure 8-2 Progressive deformation of dummy by a front blast loading with rear impact

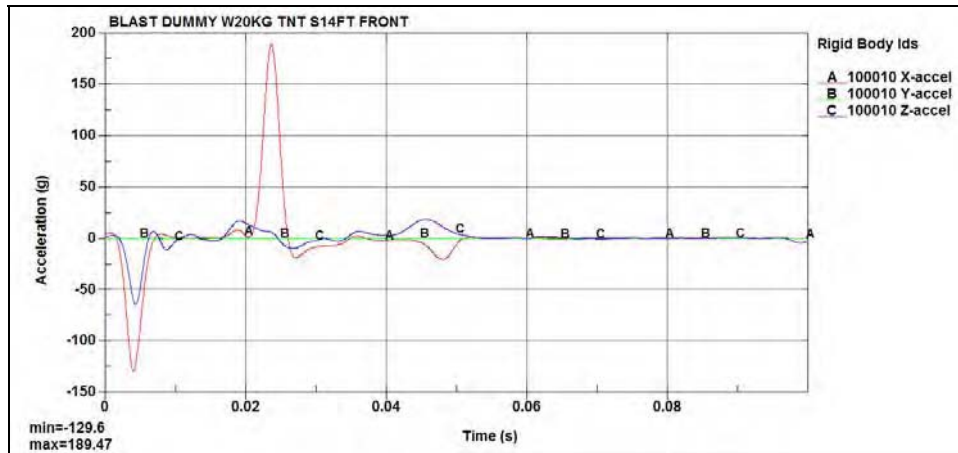


Figure 8-3 Translational acceleration time history of head

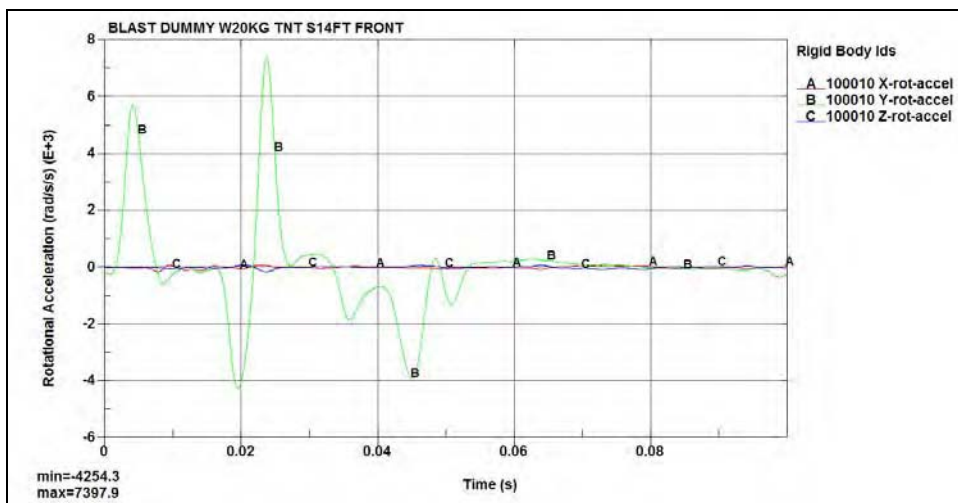


Figure 8-4 Rotational acceleration time history of head

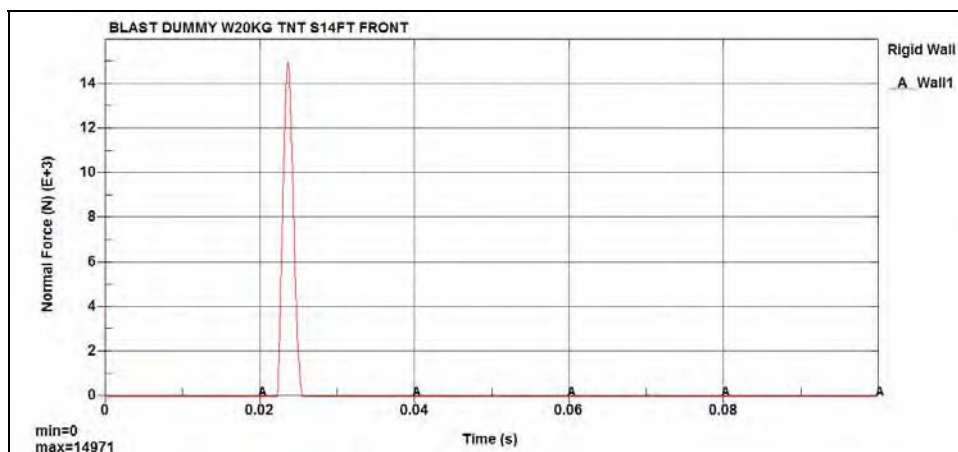


Figure 8-5 Rigid wall impact force time history

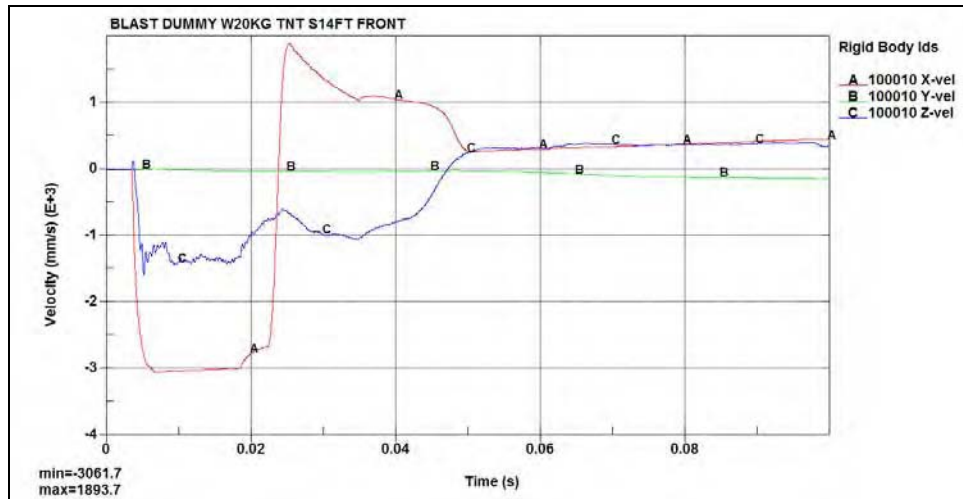


Figure 8-6 Translational velocity time history of head

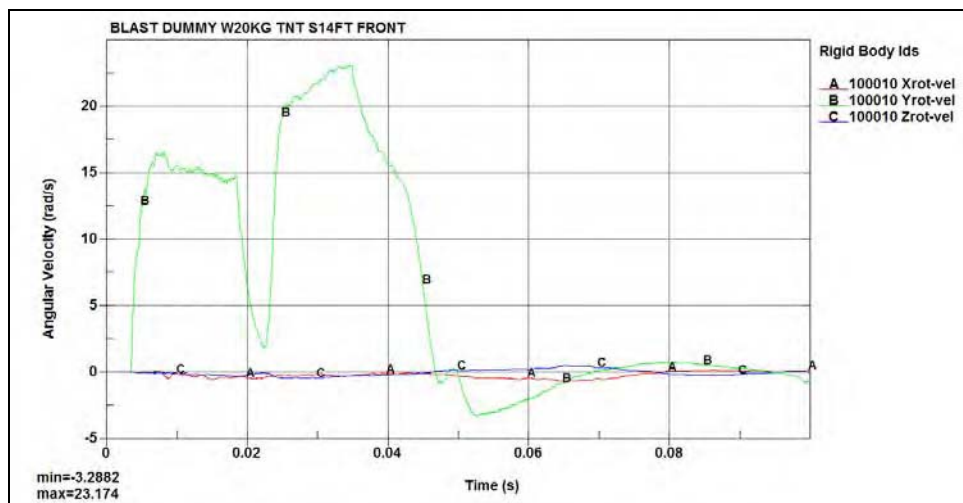


Figure 8-7 Rotational velocity time history of head

Figure 8-8 shows the fringes of intracranial pressure variation with time. As can be seen from the first 8ms, the blast wave arrived at 4ms and propagated from the anterior region to the posterior region (t=6 and t=8 ms). The occipital impact occurred at 23ms and generated a second compressive wave which propagated from occipital into anterior region (t = 24, and t=26 ms).

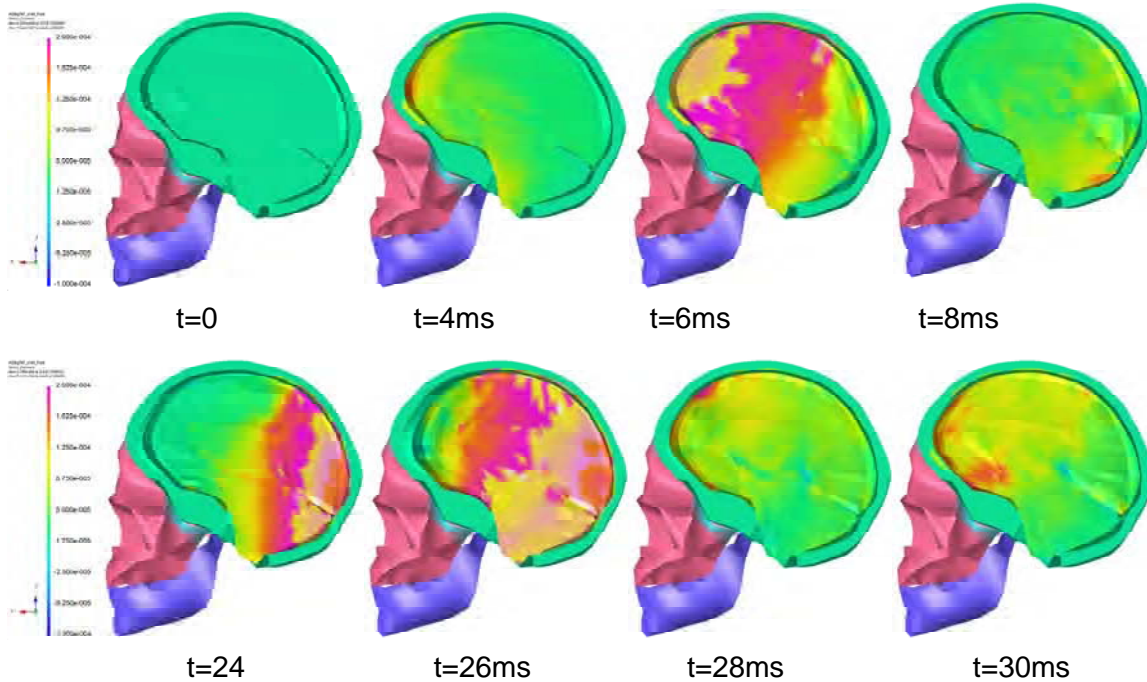


Figure 8-8 Fringes of intracranial pressure for a front blast loading and rear impact

Anterior intracranial pressure-time history (Figure 8-9) recorded a peak pressure value of 120 kPa caused by the front blast loading. In occipital region, the peak intracranial pressure was 240 kPa when impact occurred. The maximum negative intracranial pressure was approximately 80 kPa in the posterior region. Figure 8-10 shows that CSDM increased to less than 4% during the blast loading process and quickly rose above 24% as brain tissue was damaged during the rear impact event.

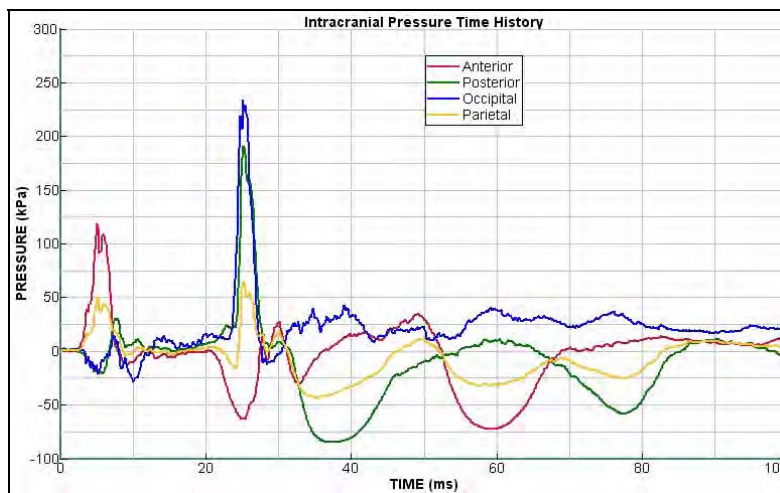


Figure 8-9 Intracranial pressure time history for a front blast with rear impact

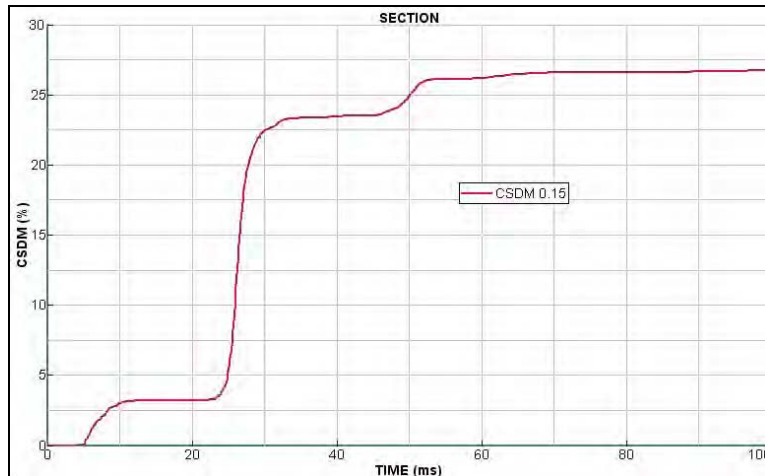


Figure 8-10 CSDM-time history for front blast loading and rear impact

8.2.2 Rear Blast Loading with Front Impact Event

In this case, a charge of 20 kg TNT was located 4.27m behind dummy. Figure 8-11 displays the progressive deformation of the dummy. The head acceleration attained its first peak of 61.7g about 5ms (Figure 8-12). The head then started to rotate under blast pressure on the front face. Head and upper body moved forward and impacted the rigid plate at 30ms (Figure 8-12 and Figure 8-14). the impact accelerated the head in the opposite direction with a peak value of 122g (Figure 8-12) and the continuing motion of the upper body caused the second head impact on the rigid plate. Figure 8-15 and Figure 8-16 plot the translational and rotational velocity time history, which also shows the double-impact events.

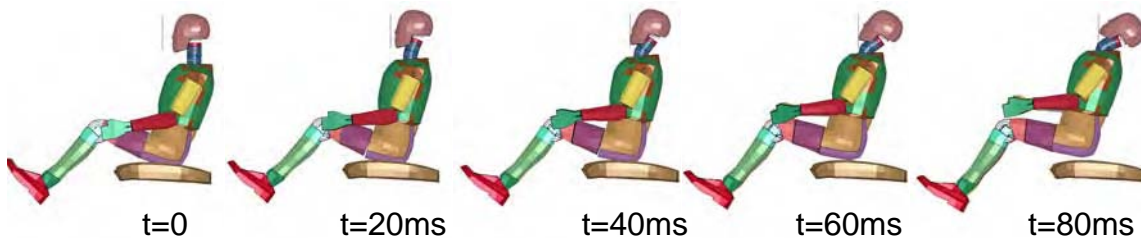


Figure 8-11 Progressive deformation of dummy by a rear blast loading with front impact

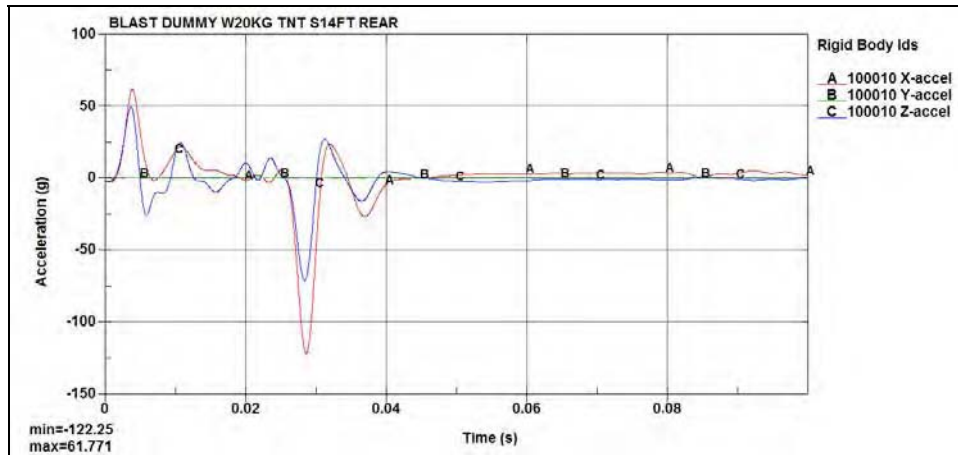


Figure 8-12 Translational acceleration time history of head

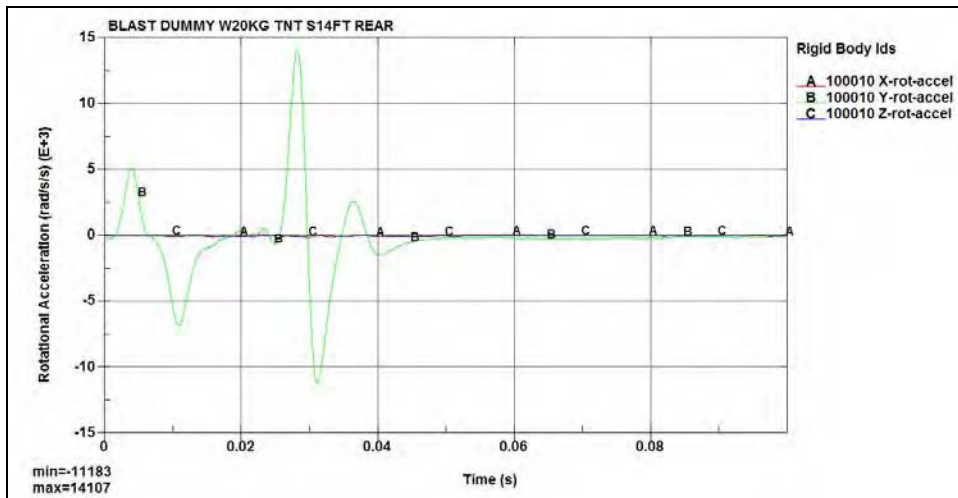


Figure 8-13 Rotational acceleration time history of head

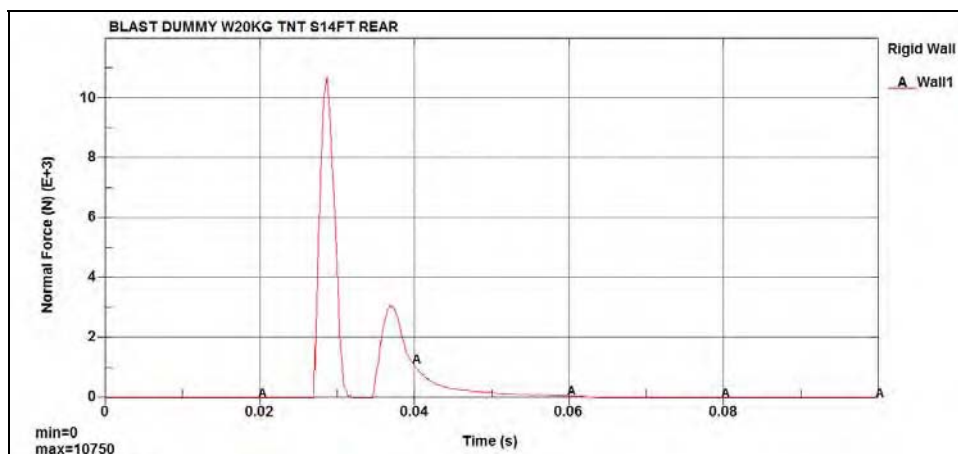


Figure 8-14 Head-rigid object impact force time history

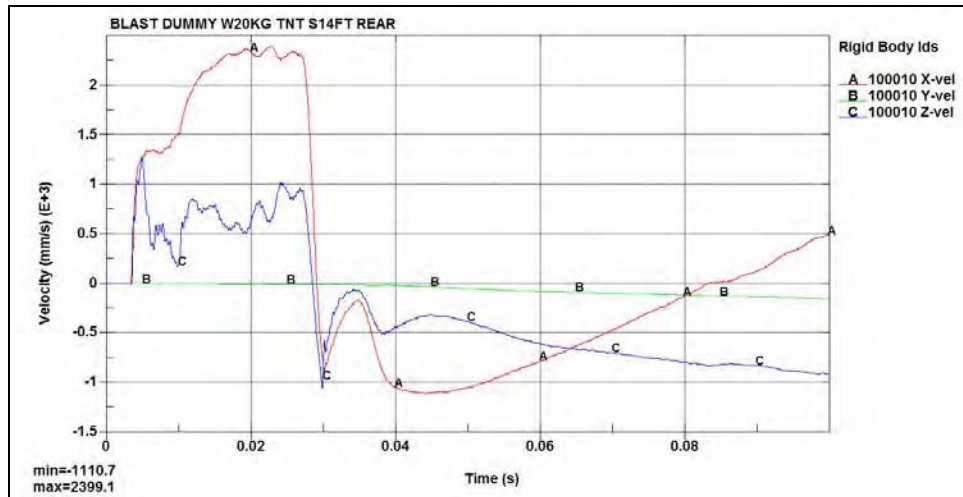


Figure 8-15 Translational velocity time history of head

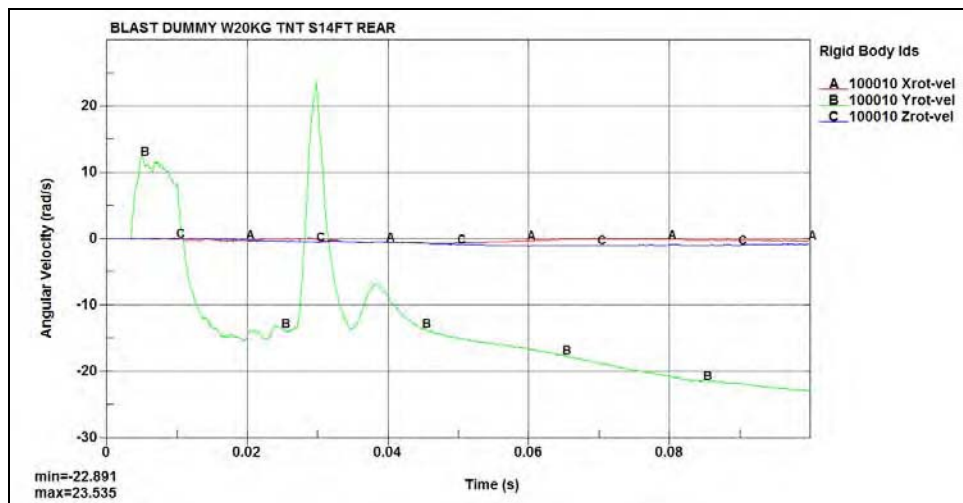


Figure 8-16 Rotational velocity time history of head

Figure 8-17 shows the fringes of intracranial pressure variation with time. As can be seen from the first 8ms, the blast wave front arrived at 4ms and it propagated from the posterior region to the parietal and anterior regions (t=6, 8ms). The first frontal impact occurred at 30ms and generated high compression in the anterior region. Pressure there rose again at 38ms by the second frontal impact. Time history of intracranial pressure displays the changes in each region (Figure 8-18).

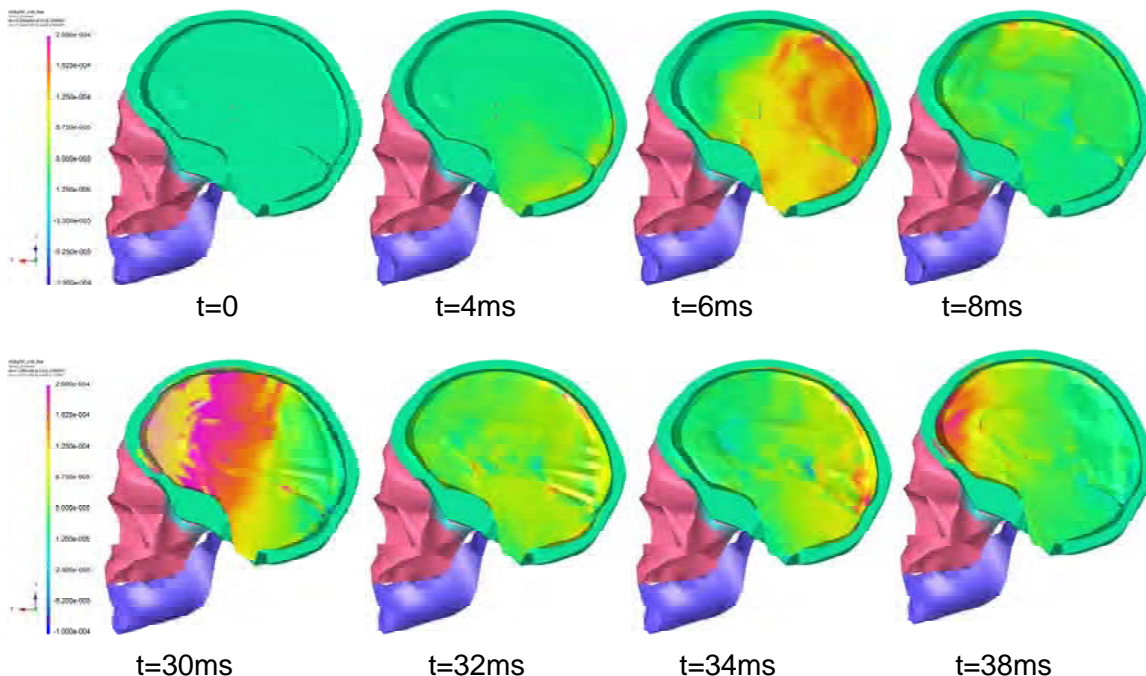


Figure 8-17 Fringes of intracranial pressure for a rear blast loading with front impact

The recorded peak pressure in anterior region was 55 kPa, which was caused by the first impact. In the occipital region, the peak intracranial pressure was 110 kPa by blast loading. The maximum negative intracranial pressure was approximately 73 kPa in anterior region. Figure 8-19 shows that CSDM increased rapidly to 26% during the front impact process.

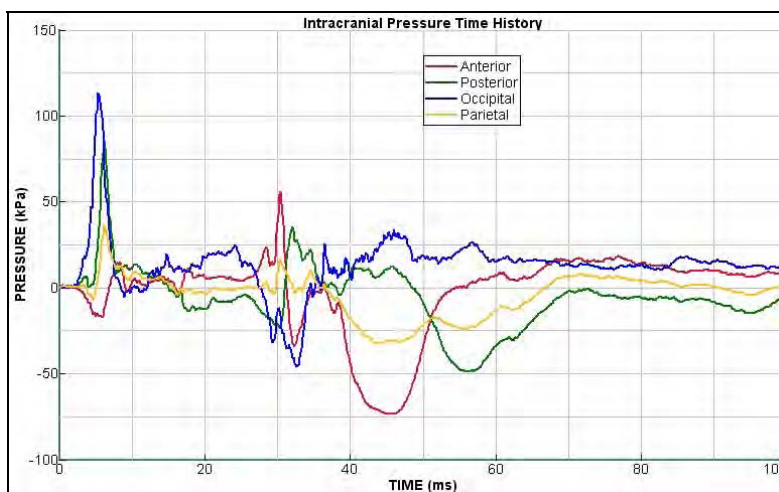


Figure 8-18 Intracranial pressure time history for a rear blast with front impact

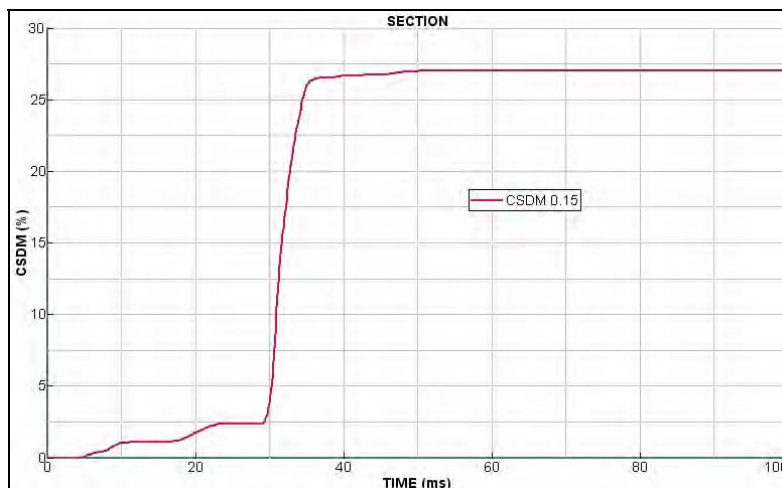


Figure 8-19 CSDM time history for a rear blast loading with front impact

8.2.3 Tertiary Blast Injury Parametric Simulation Results

To see correlations of brain injury with the combination of blast loading and impact, 22 calculation cases have been performed, half for front blast loading with rear impact and half for rear blast loading with front impact. For all cases, the charge was 20kg TNT and the standoff varied from 3m to 9 m.

Figure 8-20 to Figure 8-22 demonstrate a clear trend of intracranial pressure for front blast loading with rear impact events. The pressure history of the anterior region undergoes a positive phase when the blast pressure arrives, then enters a negative phase because of the lag of brain matter. A second positive pressure phase appears immediately after impact, followed by a second negative pressure phase (Figure 8-20). Posterior and occipital regions have the opposite trend – the dominant feature is the positive peak pressures that are produced by rear impact events, with these peak pressures ranging from 90 kPa to 240 kPa in the posterior region (Figure 8-21) and from 150 kPa to 275 kPa in the occipital region (Figure 8-22) for standoffs from 3m to 9m. For the negative pressure phase in all regions, the maximum peak is <100 kPa.

For rear blast loading with front impact events, the anterior region will experience first a negative then a positive pressure phase before impact (Figure 8-23). The front impact will produce a second positive phase then a second negative phase. These second pressure peaks dominate in the pressure plots, the positive peak pressures ranging from 50 kPa to 100 kPa and the maximum negative value less than 80 kPa. The posterior and occipital regions enter a positive pressure phase immediately under blast pressure and follow with the first negative pressure phase. The obvious effect of front impact in posterior region is the second negative pressure phase. The maximum negative peak pressure value in the posterior region produced by the front impact is <50 kPa (Figure 8-22).

As expected, the pressure history plots for the period before the head impact repeat the cases with blast loading only (Section 6).

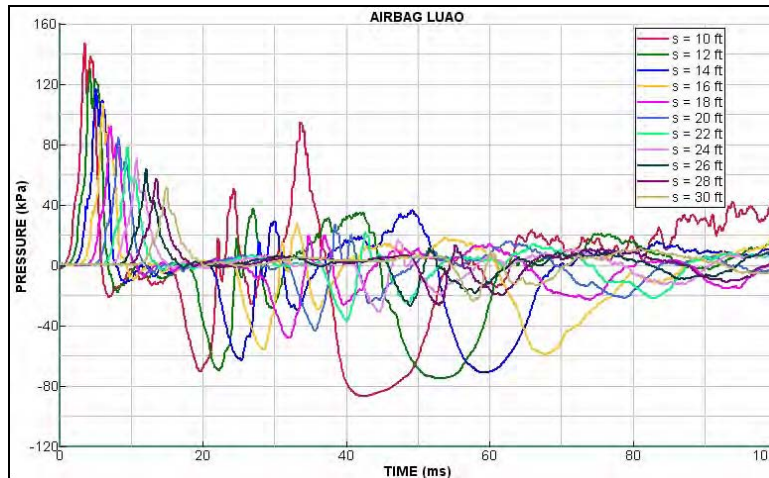


Figure 8-20 Anterior intracranial pressure histories for front blast loading and rear impact

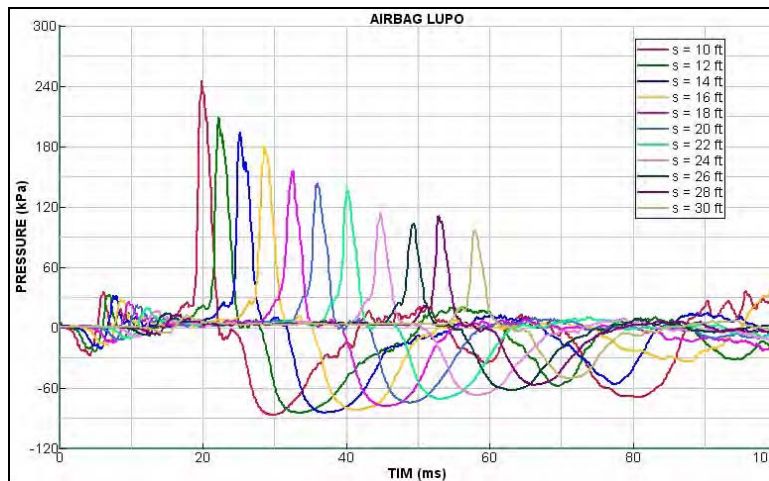


Figure 8-21 Posterior intracranial pressure histories for front blast loading and rear impact

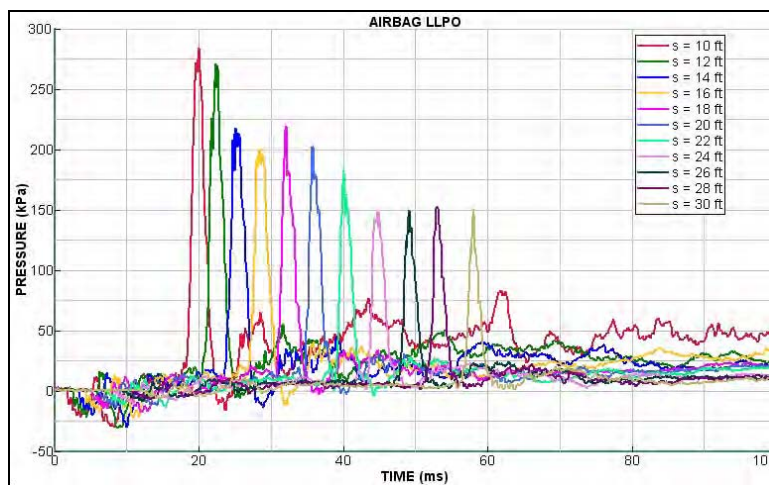


Figure 8-22 Occipital intracranial pressure histories for front blast loading and rear impact

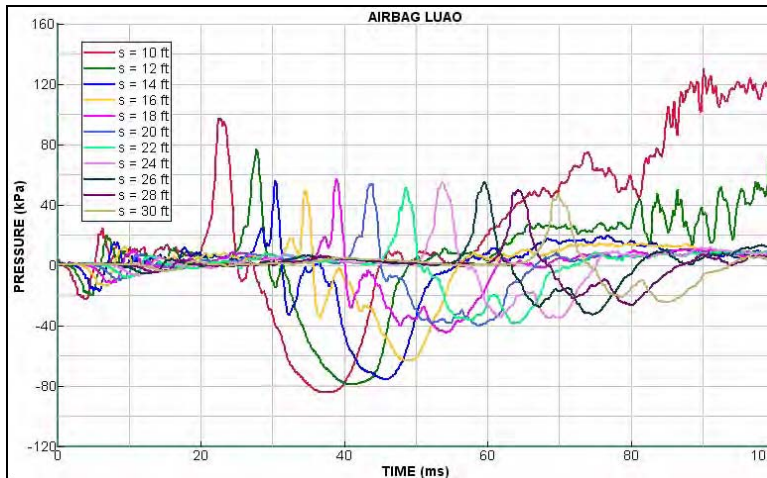


Figure 8-23 Anterior intracranial pressure histories for rear blast loading and front impact

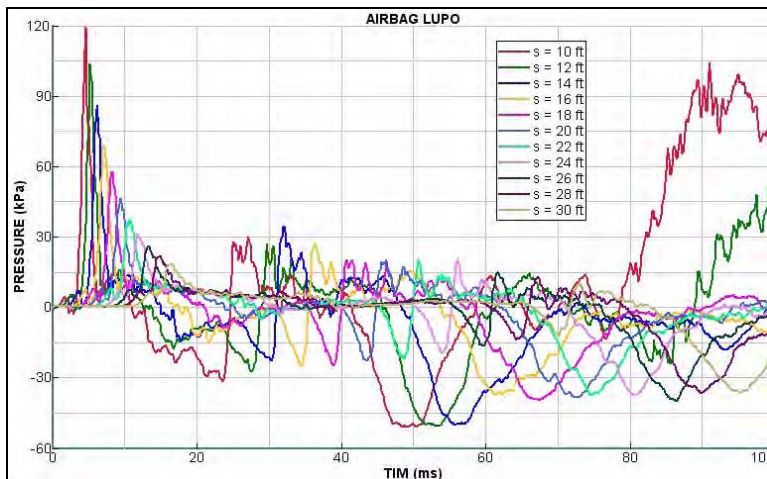


Figure 8-24 Posterior intracranial pressure histories for rear blast loading and front impact

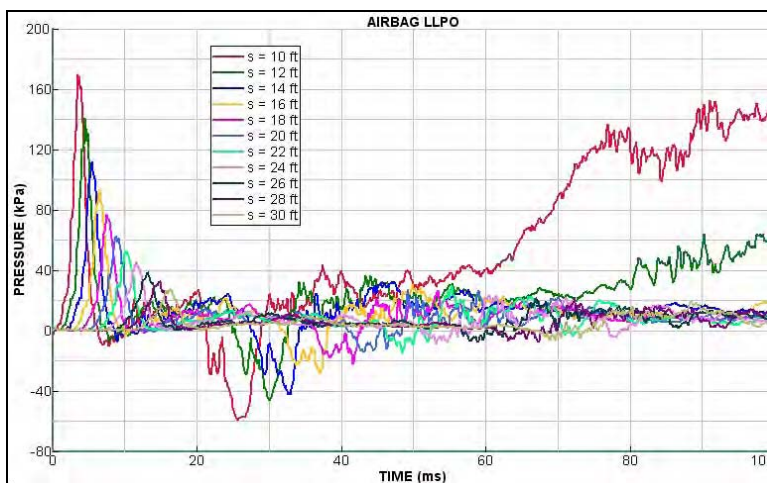


Figure 8-25 Occipital intracranial pressure histories for rear blast loading and front impact

Based on observations of these pressure history plots in the above figures (Figure 8-20 to Figure 8-25), the second pressure impulse produced by front or rear rigid impact is probably the major contributor to the tertiary blast injury. Results for all calculated cases are summarized in Figure 8-26, in which CSDM for each impact case was plotted as a function of impact impulse. These values were derived from the amount of momentum obtained by the dummy from blast loading. Details for each loading case are listed in Table 8-1. For the cases under front blast loading with rear head impact, CSDM vs impulse curve is a linear function; for the cases under rear blast loading with front head impact, it's nonlinear. This was caused by the dummy nose, which was acting as a cushion during front head impact. Such cushion effect will be reduced when the impact speed is too high.

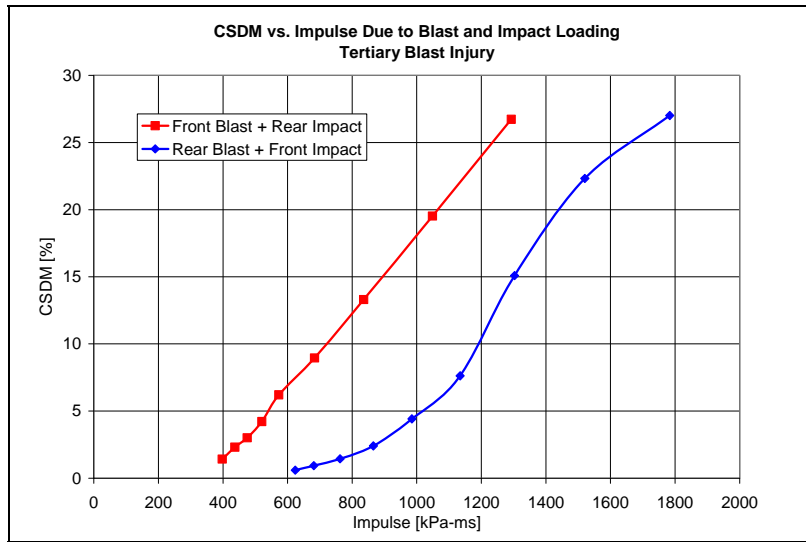


Figure 8-26 CSDM vs blast impulse for tertiary-blast brain injury

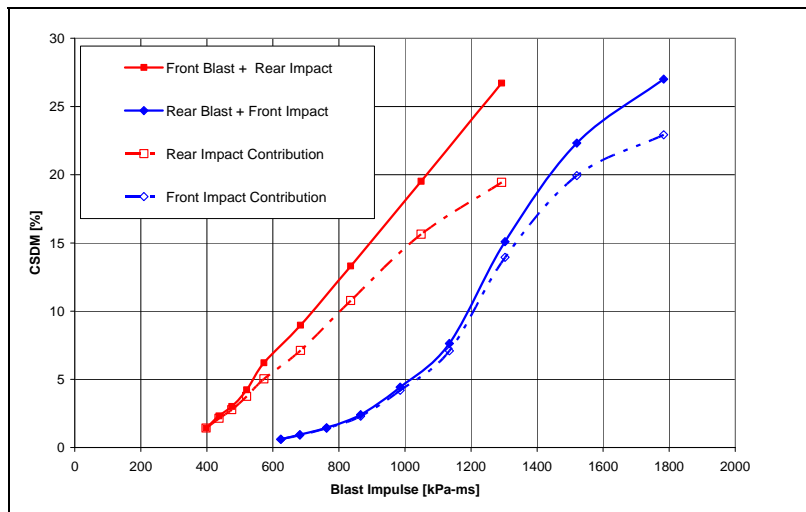


Figure 8-27 Impact contributions to CSDM for tertiary-blast brain injury

By subtracting the brain damage resulting from the blast loading phase, the contribution from head impact can be extracted, as shown in Figure 8-27. The conclusion is that the major cause of brain damage in tertiary blast injury is head impact.

Table 8-1 Calculated Cases for Tertiary Blast Injury Simulation

Standoff [ft]	Front Blast + Rear Impact				Rear Blast + Front Impact			
	AccX [g]	ΔMV [kg•m/s]	Impulse [kPa]	CSDM [%]	AccX [g]	ΔMV [kg•m/s]	Impulse [kPa]	CSDM [%]
10	247.71	572.82	2012.72	66.53	155.39	747.44	2626.28	69.73
12	216.45	469.01	1647.96	35.73	130.04	612.99	2153.87	46.98
14	189.47	367.92	1292.76	26.72	122.25	507.46	1783.06	27.01
16	166.90	298.52	1048.91	19.52	112.96	432.7	1520.38	22.32
18	143.99	237.87	835.80	13.30	102.19	370.82	1302.95	15.09
20	130.87	194.58	683.70	8.96	93.56	322.81	1134.26	7.62
22	117.41	163.05	572.91	6.21	82.27	280.39	985.21	4.42
24	100.72	148.11	520.41	4.22	72.07	246.36	865.64	2.41
26	88.18	135.29	475.37	3.01	62.87	217.01	762.51	1.45
28	91.06	124.36	436.96	2.32	56.58	193.99	681.62	0.94
30	82.23	113.26	397.96	1.43	47.75	177.6	624.03	0.6

1. AccX: Second peak acceleration in x-direction generated by impact.
2. ΔMV : Total momentum obtained by dummy by blast pressure duration.
3. Impulse: Values are converted from dummy's momentum.
4. CSDM: Values are taken at calculation termination time.
5. Charge for all cases: 20kg TNT.

8.3 Remarks

1. For the same level of blast impulse, front loading with rear impact can cause more damage than rear blast loading with front impact.
2. For front blast loading with rear impact, an impulse level of 600 kPa-ms and 1100 kPa-ms are the threshold values of mild and moderate DAI.
3. For rear blast loading with front impact, an impulse level of 1000 kPa-ms and 1500 kPa-ms are the threshold values of mild and moderate DAI.
4. Head / rigid object impact is the main contributor to brain damage during tertiary blast injury.

9. Key Research Accomplishments and Conclusions

- Validations of ESI H-Head model v2007 against Hardy et al. NDT acceleration and deceleration tests confirm that the differences between simulation and tests are within acceptable ranges.
- Validation shows reasonable correlation between H-Head model results and Nahum impact test. Both the proposed pressure loading and the acceleration loading methods can ensure that impact momentum is transferred correctly, and thus there is better matching than in previous studies.
- Through the H-Head model validation process, it was found that applying head acceleration on head CG is essentially equivalent to applying impact force or pressure loading on the outer surface of H-Head model. In both methods the head has similar kinetic response. Because the skull is relatively stiff, the contribution made by the skull deformation under impact or pressure can be neglected. Head rigid body motion is the major contributor to brain injury.
- Among several pressure loading methods currently available, ConWep is the best choice. SPH method for three-dimensional blast wave simulations is computationally expensive and not practical at this time. Numerical investigation shows a very large number of SPH particles are required for a three-dimensional blast simulation to avoid mesh-dependent solutions. For centimeter-level mesh size, the average reflected pressure calculated by SPH method is much lower than that predicted by BlastX or ConWep.
- Primary blast loading can potentially cause diffuse axonal injury. For same level of impulse, brain injury can be worse if head motion is restricted by the neck. On the other hand, brain injury can be reduced if the head passively follows upper-body motion under pressure.
 - For the front charge cases, simulation results indicate the impulse level of 1300 kPa-ms and 2000 kPa-ms are the thresholds for mild DAI (CSDM >5.5%) and moderate DAI (CSDM >22.5%).
 - For the rear charge cases, simulation results indicate the impulse level of 2400 kPa-ms and 3300 kPa-ms are the thresholds for mild DAI and moderate DAI, in sequence. Such results included the effects of dummy seating stance.
- For secondary TBI caused by fragment impact events, posterior impact can cause more tissue damage than anterior impact for same level of impact impulse. Based on simulation results, the impulse at the level of 1000 kPa-ms and 2000 kPa-ms are the thresholds for mild DAI and moderate DAI.
- For both primary and secondary blast-induced TBI, the CSDM vs impulse curves are roughly bilinear with a kink near CSDM = 5.5%. Such a fact shows that the increase of brain damage vs increase of impulse enters a higher level after the impact impulse passes the threshold value for mild DAI.
- Head impact on rigid objects is the major contributor to brain damage during tertiary blast injury. For same level of impulse, front blast loading with rear impact can

cause more damage than rear blast loading with front impact. This is consistent with observations for primary- and secondary-blast-induced TBI.

- For front blast loading with rear impact, an impulse level of 600 kPa-ms and 1100 kPa-ms are the threshold values of mild and moderate DAI.
- For rear blast loading with front impact, an impulse level of 1000 kPa-ms and 1500 kPa-ms are the threshold values of mild and moderate DAI, in sequence.

10. References

- Abel, J.M., Gennarelli, T.A., Segawa, H. (1978). Incidence and Severity of Cerebral Concussion in the Rhesus Monkey Following Sagittal Plane Angular Acceleration. In: *Proc. 22nd Stapp Car Crash Conference*, 35–53. Paper No. 780886.
- Bandak, F.A., Eppinger, R.H. (1994). A Three-Dimensional Finite Element Analysis of the Human Brain under Combined Translational and Rotational Acceleration. In: *Proc. 38th Stapp Car Crash Conference*, 145–163. Paper No. 942215.
- Bandak, F.A., Tannous, R.E., Zhang, A.X., Dimasi, F., Masiello, P., Eppinger, R.H. (2001). SIMon: A simulated injury monitor, application to head injury assessment. In: 17th International Technical Conference on the Enhanced Safety of Vehicles, Amsterdam, Holland.
- Bandak, F.A., Tannous, R.E., Zhang, A.X., Toridis, T.G., Eppinger, R.H. (1996). Use of Finite Element Analysis and Dummy Test Measurements for the Assessment of Crash Injury Traumatic Brain Injury. In: *Advisory Group for Aerospace Research and Development, Mescalero, New Mexico*, 10–10.13.
- Chapon, A., Verriest, J.P., Dedoyan, J., Trauchessec, R., Artru, R. (1983). Research On Brain Vulnerability from Real Accidents, Iso Document No. Iso/Tc22sc12/Gt6/N139.
- Chazal, J., Tanguy, A., Bourges, M. (1985). Biomechanical Properties of Spinal Ligaments and a Historical Study of the Supraspinal Ligament in Traction. *J. Biomech.* **18** (3), 167–176.
- Choi, H.-Y., Lee, I.-H. (1999b). Advanced Finite Element Modeling of the Human Body for Occupant Safety Simulation. In: *Europam 1999*, ESI Software S.A., 99, Rue Des Solets, BP 80112, 94513 Rungis Cedex, France.
- Claessens, M. (1997). *Finite Element Modeling of the Human Head under Impact Conditions*. PhD Thesis. Eindhoven University. ISBN 90-386-0369-X.
- Claessens, M., Sauren, F., Wismans, J. (1997). Modeling the Human Head under Impact Conditions: A Parametric Study. In: *Proc. 41st Stapp Car Crash Conference*, 315–328. Paper No. 973338.
- Cooper, P.R. (1982a). Post-Traumatic Intracranial Mass Lesions. In: Cooper, P.R. (Ed.), *Head Injury* (Williams and Wilkins, Baltimore/London), 185–232.
- Cooper, P.R. (1982b). Skull Fracture and Traumatic Cerebrospinal Fluid Fistulas. In: Cooper, P.R. (Ed.), *Head Injury* (Williams and Wilkins, Baltimore/London), 65–82.

- Dimasi, F., Marcus, J., Eppinger, R. (1991). 3-D Anatomic Brain Model for Relating Cortical Strains to Automobile Crash Loading. In: *13th ESV International Technical Conference on Experimental Safety Vehicles*. Paper No. 91-S8-O-11.
- Donnelly, B.R., Medige, J. (1997). Shear Properties of Human Brain Tissue. *J. Biomech. Engrg.* **119**, 423–432.
- Ewing, C., Thomas, D., Lustick, L., Muzzy, W.Iii, Willems, G., Majewski, P. (1976). the Effect of Duration, Rate of Onset, and Peak Sled Acceleration On the Dynamic Response of the Human Head and Neck. In: *Proc. 20th Stapp Car Crash Conference*, 3–41. Paper No. 760800.
- ESI Group, 2008, Virtual Performance Solutions – Explicit solver reference manual.
- Guha, S., Bhalsod, D. and Krebs, J., 2008, LSTC Hybrid III Dummies – Positioning & post-processing, Livermore Software Technology Corporation.
- Gennarelli, T.A. (1980). Analysis of Head Injury Severity by Ais-80. In: *24th Annual Conference of the American Association of Automotive Medicine (AAAM, Morton Grove, Il)*, 147–155.
- Gennarelli, T.A., Thibault, L.E., Adams, J.H., Graham, D.I., Thompson, C.J., Marcincin, R.P. (1982). Diffuse Axonal Injury and Traumatic Coma in the Primate. *Ann. Neuron.* **12**, 564–574.
- Gurdjian, E.S., Lissner, H.R. (1944). Mechanism of Head Injury As Studied by the Cathode Ray Oscilloscope, Preliminary Report. *J. Neurosurgery* **1**, 393–399.
- Gurdjian, E.S., Roberts, V.L., Thomas, L.M. (1966). Tolerance Curves of Acceleration and Intracranial Pressure and Protective Index in Experimental Head Injury. *J. Trauma* **6**, 600–604.
- Gurdjian, E.S., Webster, J.E., Lissner, H.R. (1955). Observations of the Mechanism of Brain Concussion, Contusion, and Laceration. *Surgery Gynecol. Obstet.* **101**, 680–690.
- Hardy, W.N., Foster, C.D., Mason, M.J., Yang, K.H., King, A., and Tashman, S., 2001, Investigation of Head Injury Mechanisms Using Neutral Density Technology and High-Speed Biplanar X-Ray, 337-368, *Stapp Car Crash Journal* vol. 45.
- Holbourn, A.H.S. (1943). Mechanics of Head Injury. *Lancet* **2**, 438–441.
- Kang, H.S., Willinger, R., Diaw, B.M., Chinn, B. (1997). Validation of A 3d Anatomic Human Head Model and Replication of Head Impact in Motorcycle Accident by finite Element Modeling. In: *Proc. 41st Stapp Car Crash Conference*, 329–338. Paper No. 973339.

- Langlois, JA; Rutland-Brown, W; Thomas, KE. Traumatic brain injury in the United States: Emergency department visits, hospitalizations, and deaths. Atlanta, GA: Centers for Disease Control and Prevention, National Center for Injury Prevention and Control, 2004.
- Lee, M.C., Melvin, J.W., Ueno, K. (1987). Finite Element Analysis of Traumatic Subdural Hematoma. In: *Proc. 31st Stapp Car Crash Conference*, 67–77. Paper No. 872201.
- Lee, M.C., Haut, R.C. (1989). Insensitivity of Tensile Failure Properties of Human Bridging Veins to Strain Rate: Implications in Biomechanics of Subdural Hematoma. *J. Biomech.* 22, 537–542.
- Lissner, H.R., Lebow, M., Evans, F.G. (1960). Experimental Studies On the Relation Between Acceleration and Intracranial Pressure Changes in Man. *Surgery Gynecol. Obstet.* 111, 329–338.
- LSTC, 2007, LS-DYNA Keyword User’s Manual.
- Meaney, D.F., Smith, D., Ross, D. T., and Gennarelli, T. A., 1993, Diffuse Axonal Injury in the Miniature pig, Biomechanical Development and Injury Threshold, ASME Crashworthiness and Occupant Protection in Transportation Systems, 169-175, 25.
- Margulies, S.S., Thibault, L.E., Gennarelli, T. A. (1990). Physical Model Simulations of Brain Injury in the Primate. *J. Biomech.* 23, 823–836.
- Miller, K., Chinzei, K. (1997). Constitutive Modeling of Brain Tissue: Experiment and Theory. *J. Bio*
- Nahum, A.M., Smith, R., Ward, C.C. (1977). Intracranial Pressure Dynamics During Head Impact. In: *Proc. 21st Stapp Car Crash Conference*, 339–366. Paper No. 770922.
- Nahum, A.M., and Smith, R.W., 1976, An Experimental Model for Closed Head Impact Injury, *Proceedings of 20th Stapp Car Crash Conference (SAE 760825)*.
- Newman, J.A. (1993). Biomechanics of Head Trauma: Head Protection. In: Nahum, A.M., Melvin, J.W. (Eds.), *Accidental Injury – Biomechanics and Prevention* (Springer, Berlin), 292–310 (Chapter 13).
- Ommaya, A.K., Hirsch, A.E., Flamm, E.S., Mahone, R.H. (1966). Cerebral Concussion in the Monkey: An Experimental Model. *Science* 153, 211–212.
- Ommaya, A.K., Hirsch, A.E. (1971). Tolerances for Cerebral Concussion from Head Impact and Whiplash in Primates. *J. Biomech.* 4, 13–31.

- Ommaya, A.K., Gennarelli, T.A. (1974). Cerebral Concussion and Traumatic Unconsciousness: Correlation of Experimental and Clinical Observations On Blunt Head Injuries. *Brain* 97, 633–654.
- Ommaya, A.K., Hirsch, A.E. (1971). Tolerances for Cerebral Concussion from Head Impact and Whiplash in Primates. *J. Biomech.* 4, 13–31.
- Ono, K., Kikuchi, A., Nakamura, M., Kobayashi, H., Nakamura, N. (1980). Human Head Tolerance to Sagittal Impact Reliable Estimation Deduced from Experimental Head Injury Using Subhuman Primates and Human Cadaver Skulls. In: *Proc. 24th Stapp Car Crash Conference*, 101–160. Paper No. 801303.
- Ono, K., et al. (1999). Relationship Between Localized Spine Deformation and Cervical Vertebral Motions for Low Speed Rear Impacts Using Human Volunteers. In: *Ircobi Conference, Spain*, 149–164.
- Pennardt, A. and Lavonas E. J. (2009), Blast Injuries. [eMedicine.com Web site]. June 23 30, 2009. Available at: <http://emedicine.medscape.com/article/822587-overview>.
- Penn, R.D., Clasen, R. A. (1982). Traumatic Brain Swelling and Edema. In: Cooper, P.R. (Ed.), *Head Injury* (Williams and Wilkins, Baltimore), 233–256.
- Putz, R., Pabst, R. (2000). *Sobotta – Atlas Der Anatomie Des Menschen*, Twenty-first Ed. (Urban&Fischer, München, Jena).
- Ruan, J.S., Khalil, T.B., King, A.I. (1991). Human Head Dynamic Response to Side Impact by Finite Element Modeling. *J. Biomech. Engrg.* 113, 267–283. PhD Dissertation, Wayne State University.
- Ruan, J.S., Prasad, P. (1994). Head Injury Assessment in Frontal Impacts by Mathematical Modeling. In: *Proc. 38th Stapp Car Crash Conference*, 111–121. Paper No. 942212.
- Salazar, AM; Zitnay, GA; Warden, DL; Schwab, KA. DVHIP Study Group. Defense and Veterans Head Injury Program: Background and Overview. *J Head Trauma Rehabil*, Vol. 15(5), 1081-1091, 2000.
- Sances Jr, A., et al. (1982). Head and Spine Injuries. In: *Agard Conference on Injury Mechanisms, Prevention and Cost, Köln, Germany*, 13-1–13-33.
- Scott, W.E. (1981). Epidemiology of Head and Neck Trauma in Victims of Motor Vehicle Accidents. Head and Neck Criteria. In: Ommaya, A.K. (Ed.), *A Consensus Workshop* (Us Department of Transportation, National Highway Traffic Safety Administration, Washington, Dc), 3–6.
- Spitzer, V.M., Whitlock, D.G. (1998). *Atlas of the Visible Human Male* (Jones & Bartlett

- Publishers), 67.
- Taber, KH; Warden, DL; Hurley, RA. Blast-related traumatic brain injury: What is known? *J Neuropsychiatry Clin Neurosci*, Vol. 18, 141-145, 2006.
- Tarriere, C. (1981). Investigation of Brain Injuries Using the Ct Scanner. In: Ommaya, A. K. (Ed.), *Head and Neck Injury Criteria: A Consensus Work-Shop* (Us Department of Transportation, National Highway Traffic Safety Administration, Washington, DC), 39–49.
- Takhounts, E. G., Eppinger, R. H., Campbell, J. Q., Tannous, R. E., Power, E. D., and Shock, L. S., (2003) On the Development of the SIMon Finite Element Head Model, *Stapp Car Crash Journal*, 107-133, vol. 47.
- Thurman, D. The epidemiology and economics of head trauma. In: Miller, L; Hayes, R, Eds. *Head Trauma Therapeutics: Basic, Preclinical and Clinical Aspects*. New York (NY): Wiley and Sons, 2001.
- Torg, J. S. (Ed.) (1982). *Athletic Injuries to the Head, Neck and Face* (Lea & Febiger, Philadelphia, Pa).
- Torg, J. S., Pavlov, H. (1991). Axial Load “Teardrop” Fracture. In: *Athletic Injuries to the Head, Neck and Face*, second ed. (Lea & Febiger, Philadelphia, PA).
- Trameçon, A., Allain, J.C, Haug, E., Montmayeur, N., and Beaugonin, M., 2003, Design of Soldier’s Protection Equipment: Recent Trends in Biomechanical Models and Comfort. *Proceeding of 74th Shock and Vibration Symposium* (U-065).
- Turquier, F., Kang, H.S., Trosseille, X., Willinger, R., Lavaste, F., Tarriere, C., Dömönt, A. (1996). Validation Study of a 3D Finite Element Head Model against Experimental Data. In: *Proc. 40th Stapp Car Crash Conference*, 283–293. Paper No. 962431.
- Ueno, K., Melvin, J.W., Lundquist, E., Lee, M. C. (1989). Two-Dimensional Finite Element Analysis of Human Brain Impact Responses: Application of a Scaling Law. In: *Crashworthiness and Occupant Protection in Transportation Systems*. In: AMD 106 (The American Society of Mechanical Engineers, New York), 123–124.
- Voo, L., Kumaresan, S., Pintar, F.A., Yoganandan, N., Sances Jr, A. (1996). Finite Element Models of the Human Head. *Medical Biological Engrg. Comput.* 34, 375–381.
- Walke, A.E., Kollros, J. J., Case, T.J. (1944). The Physiological Basis of Concussion. *J. Neurosurg.* 1, 103–116.

- Willinger, R., Kang, H.S., Diaw, B. (1999). Three-Dimensional Human Finite-Element Model Validation against Two Experimental Impacts. *Ann. Biomedical Engrg.* **27**, 403–410.
- Wismans, J.S.H.M., et al. (1994). *Injury Biomechanics* (Eindhoven University of Technology), 49.
- Zeidler, F., Stürtz, G., Burg, H., Rau, H. (1981). Injury Mechanisms in Head-On Collisions Involving Glance-Off. In: *Proc. 25th Stapp Car Crash Conference*, 825–860. Paper No. 811025.
- Zhou, C., Khalil, T. B., King, A.I. (1996). Viscoelastic Response of the Human Brain to Sagittal and Lateral Rotational Acceleration by Finite Element Analysis. In: *International Ircobi Conference on the Biomechanics of Impact, Dublin, Ireland*.
- Zhang, L., Yang, K., Dwarampudi, R., Omori, K., Li, T., Chang, K., Hardy, W., Khalil, T., and King, A., 2001. Recent advances in brain injury research: A new human head model development and validation. *Stapp Car Crash Journal*, *45*, 369-393.